

Fluid-walled microfluidics for cell migration studies

Cyril Deroy

Brasenose College
University of Oxford

Thesis submitted for the degree of:
Doctor of Philosophy (DPhil)

Michaelmas 2021

Academic Supervisor:
Prof. Edmond Walsh
Department of Engineering Science, University of Oxford

Table of Contents

Abstract *6*

Acknowledgments *7*

Chapter 1: Introduction *9*

Objectives **11**

References **14**

Chapter 2: Literature Review *16*

A brief history of microfluidics **16**

Movement towards Lab-on-a-Chip systems **16**

Microfluidic organ models for drug testing and disease modelling **17**

Challenges facing microfluidic adoption in the biomedical community **18**

Open microfluidics and the advent of fluid-walled microfluidics **19**

The importance of flow in cell culture **21**

Chemotaxis: the study of directed cell migration **21**

References **23**

Chapter 3: Predicting flows through microfluidic circuits with fluid walls *30*

Abstract **30**

Introduction **31**

Results **33**

Circuit fabrication and operation 33

The challenge: predicting flows when fluid walls morph 33

Measuring conduit height 35

FBS creates a no-slip boundary at media:FC40 interfaces 35

Semi-analytical model to describe fluid-walled conduits 37

The semi-analytical solution predicts experimentally-measured heights 38

Predicting wall shear stress 41

Chokes reduce height variations down conduits 41

Predicting flows in complex networks 44

Discussion **46**

Materials and Methods **48**

Fluid-walled microfluidic circuit fabrication 48

Perfusing fluid-walled conduits 48

Measuring conduit height 49

References **51**

Supplementary Information **54**

List of symbols 54

Semi-analytical solution for fluid-walled conduits 54

Importance of conduit exit-height 61

Numerical solution 62

Pendant-drop tensiometry 65

Reynolds number in fluid-walled conduits 66
Conduit capillary length 68
Semi-analytical solution for perfect slip at the media:FC40 interface 69
Conduit failure 70
Collapsing numerical and semi-analytical solutions 72
Error analysis for conduit-height predictions 74
Varying flow regimes 77
Splitting conduits 78
Height correction for apparent depth in microscope measurements 80
Maintaining constant shear along fluid-walled conduits 86
Semi-analytical solution for shear stress 87
Effect of a choke on the gradient of wall shear stress 88
Error from $\boldsymbol{h/a}$ simplification on shear stress gradient in choked conduits 92
Culturing cells in fluid-walled conduits 94
Supplementary Movie 95

Chapter 4: Reconfiguring microfluidic circuits to isolate and retrieve cells of interest 98

Abstract 98

Introduction 99

Results 101
Workflow 101
Printing fluid-walled microfluidic circuits 101
Managing positional information 103
Exposing cells to chemical gradients, imaging, and isolating migrating cells 103
Recovering macrophages chemotaxing towards C5a 106
Establishing the gradient 106
Identifying the chemotaxing population 106
Isolating the chemotaxing sub-population 107
Extracting the chemotaxing sub-population 107
Recovering *P. aeruginosa* cells migrating towards antibiotics 109
Imaging bacteria within antibiotic gradients 110
Reconfiguring circuits on a microscope to isolate migrating cells 111
Extracting chemotaxing cells and assessing their viability 112

Discussion 115

Materials and Methods 117
Strains, media and culture conditions 117
Imaging 117
Circuit design and fabrication 118
BMDM circuit 118
P. aeruginosa circuit 119
Exposing BMDMs to a gradient of C5a 119
Exposing *P. aeruginosa* to a ciprofloxacin gradient 121
Determining maximum gradient widths 122
3D-printed adaptors for easy manipulation of circuits on and off the microscope 123
Calibrating a circuit before reconfiguration on a microscope 124
Isolating and extracting chemotaxing BMDMs both on and off the microscope 125
Automated retrieval of isolated BMDMs 125
Assessing BMDM viability post-extraction 126
Isolating and extracting migrating *P. aeruginosa* cells 126
Extracting planktonic P. aeruginosa from the isolation chamber 127

Assaying viability of surface-attached P. aeruginosa 128
Image analysis 128
References 130
Supplementary Figures 133
Supplementary Videos 142
Supplementary STEP files of the 3D-printed parts 142
Chapter 5: Fluid-walled microfluidic assay for macrophage chemotaxis 144
Abstract 144
Introduction 145
Results 147
Workflow and operation 147
Printing circuits 147
Loading and generating stable gradients in passive circuits 147
Steady-state and gradient stability 148
Moving dishes containing passive circuits does not impair gradient formation 149
Setting up gradients in active circuits 150
Passive circuits for BMDM chemotaxis 152
Exposing BMDMs to gradients of C5a 152
Distinguishing between chemotaxis and chemokinesis 153
Cells at the front behave differently from those behind 155
Patterning cells in conduits reveals different population dynamics 155
Determining chemotactic responses to concentration and gradient strength 156
Comparing multiple cell types and high-throughput chemotaxis studies in well plates 158
Label-free comparison of different cell populations in single circuits 158
Increasing throughput using well plates 158
Active circuits for chemotaxis assays in steady and shifting gradients 161
Generating defined steady gradients in flowing circuits 161
BMDMs respond to low concentrations of C5a in flow-generated gradients 162
BMDM taxis in instantaneously-shifted and continuously-shifted gradients 163
Discussion 167
Materials and Methods 172
Strains, media, culture conditions and reagents 172
Imaging 172
Printing circuits 173
Loading and patterning cells 173
Jetting circuits 173
Circuit design 174
Generating stable concentration gradients 175
Passive circuit 175
Active circuit 175
Determining the diffusion coefficient of C5a 176
Image analysis 176
xCELLigence chemotaxis assay 176
References 178
Supplementary Information 183
Determining concentration gradients in passive circuits 183
Dose-response of BMDMs to C5a 186

Determining chemotaxis onset in passive circuits 187
Determining concentration gradients in active circuits 188
Assessing the effect of circuit geometry on cell velocity 192

Movies 194

Chapter 6: Discussion 198

Conclusion 198

Future work 201
Dynamic systems controlled by gradients in Laplace pressure 201
Measuring diffusion coefficients in flowing conduits 202
Understanding the suicidal response of bacteria to antibiotics 204
Population dynamics in macrophages 205

Abstract

Microfluidic systems have evolved significantly over the past decade to offer biologists *in vitro* environments that mimic organ function, enable disease modelling, and perform high-throughput drug screens. Despite these important advances, microfluidic uptake in biomedical research remains limited, with the main reasons cited being biocompatibility concerns, technical complexity, and low flexibility of systems. Recently, an alternative approach to traditional microfluidics was developed, which uses only the materials common to biologists. The technique, termed fluid-walled microfluidics, shapes cell culture media on Petri dishes in a variety of methods and has been extensively studied in static environments, using chambers resembling sessile drops to perform various cell-based assays. However, studies involving flow have remained limited to proof-of-concept applications. As flow regulates many biological behaviours, it is essential to incorporate flow in fluid-walled microfluidic assays to make these accessible to the wider biomedical community.

This thesis explores the underlying properties of fluid-walled systems to establish and experimentally validate a simple mathematical model of circuits experiencing flow, and applies it to study complex cell migration behaviours. A method for real-time isolation and retrieval of specific sub-populations of cells in flowing environments is then introduced, using 3D-printed adaptors to convert microscopes into micromanipulators that reconfigure circuits, and applied to study both mammalian and bacterial cell migration in response to various concentration gradients (chemotaxis). Finally, a general approach for chemotaxis studies is presented, using both passive and active circuits (with/without flow) to give users flexibility and control over defined experimental conditions. Altogether, this thesis serves as a blueprint for the fabrication and manipulation of open and flowing microfluidic circuits using only Petri dishes, cell culture media, FC40, a 3-axis traverse and syringe pumps. The methods outlined empower biologists to study complex cellular behaviours in environments that more closely mimic *in vivo* conditions, with the aim of making microfluidic technology accessible to the less experienced user.

Acknowledgments

These past four years have been more than just a degree: a journey, an adventure, and a ride that I have enjoyed more than I could have ever imagined. This was made possible by the people that accompanied me over the years, and who have made this work a reality.

I would first like to thank my supervisor, Prof. Edmond Walsh, for making this DPhil possible and for providing invaluable guidance along the way. Through your inspiring dedication to research and mastery of scientific thinking, you changed the way I approach problems and taught me to ask the right questions.

To Prof. Peter Cook, my adoptive supervisor, your breadth and depth of knowledge is an inspiration to all, and your attention to detail taught me to skilfully present my work to the broader scientific community. Your door was always open (including weekends), and our stimulating conversations, whether about science, football, or politics, created an enjoyable and fulfilling working environment.

To Cristian, my lab mate, housemate, and travel partner, most of my experiences throughout this DPhil were shared with you, from my first international conference to the start of the pandemic, our mutual appreciation for comedy made every single moment truly enjoyable. To Nick, my work partner and gym buddy, your inspiring motivation and constant positivity pushed me to become the best version of myself. To Federico, my last remaining lab partner, I couldn't have asked for a better friend and colleague to accompany me in the final stages of this DPhil. To all of the lab lads, thank you for making this workspace feel like home.

To Jamie, my first collaborator, you made spending so many sleepless nights in the lab fun and bearable, together with some help from Hall & Oates. To Agata, my second

collaborator and welfare partner in arms, you made the Greave's group feel like a second home, and made coffee breaks a delightful ritual with all your delicious homemade cakes.

To my Oxford friends that have shaped and enriched my experiences outside of the lab, Cameron, Robin, Alex, Alexis, Andrew, and Gilad, Oxford would not have been such a fulfilling experience without all of you. To my London and Paris friends, Julien, Olivier, Melis, Dylan Bourgeois, Dylan Berthier, Chris, Couros, Charlie, Alizée, Jarrod, Eliot, Driss, and Philipp, thank you all for being a strong and reliable support network.

To my parents, Joëlle and Laurent, who have been my strongest supporters and always encouraged me to pursue my ambitions, this work is a result of your dedication and commitment to providing the best upbringing possible. To Marine and Olivia, the greatest and most caring sisters a brother could ask for. To my grandparents, Claire, Jean, Claude, and Hervé, your combined depth of knowledge and wealth of experience inspired me to pursue a career in science and have helped shape me into the researcher I am today. To Sarah, Laurent, and Serge, who provided me with unconditional support along the way, your kindness and generosity knows no bounds.

To Helene, my partner, words cannot begin to express my gratitude for the help, love, and support you provided throughout this journey. You were always the first to inspire and encourage me during the tumultuous stages of this thesis, finding the right words to reassure and motivate me to overcome unexpected obstacles, providing invaluable guidance and support through your kindness and generosity. I never stop being amazed by your wisdom and astute mind, and cannot thank you enough for the advice and support you offered along the way. Your contribution to my work and experiences at Oxford cannot be overstated, and as a small token of appreciation, I dedicate this thesis to you.

Chapter 1: Introduction

The application of microfluidics to biomedical research revolutionised our understanding of biological processes by offering new ways to mimic and reproduce cellular environments *in vitro*. On the cover, microfluidic systems appear to solve many of the problems faced by biologists regularly: they typically require microlitre amounts of reagents that are often very expensive, and so greatly reduce costs and minimise waste, they enable precise control of flow to create physiologically relevant environments for cells (in contrast to traditional static cell culture), are often inexpensive to produce, and can be reused [1], [2]. Despite this, adoption of microfluidic devices in biomedical labs remains limited, while most microfluidic-based research is published in engineering or specialised journals [3]. Reasons cited for this lack of uptake include poor sample accessibility as cells are typically confined within solid walls, the need for specialised equipment to operate devices and their technical complexity, air-bubble trapping in microfluidic channels that block or disturb flow patterns and dislodge cells, and finally the questionable biocompatibility of polydimethylsiloxane (PDMS) used in most microfluidic device fabrication [4]–[6]. The title of a review from Berthier *et al.* in 2012 [5] still rings true today: “Engineers are from PDMS-land, Biologists are from Polystyrenia”.

Considering both current advantages and drawbacks of microfluidic technology, it becomes possible to conceptualise the ideal microfluidic system. Such a device would be open in nature to allow easy access to samples and cells, allow rapid prototyping and fabrication times, integrate easily into existing workflows, flexibly and reliably incorporate and control flow, be reconfigurable to isolate cells of interest, and crucially be entirely biocompatible and cell-friendly. Open microfluidic systems have been developed to enable sample accessibility, removing at least one of the device’s solid walls which becomes a fluid interface. Notable

techniques include scanning probe microscopy to perform localised chemistry on biological interfaces [7], yet most existing open devices are fabricated and operate similarly to traditional systems. Recently, a new branch of open microfluidics developed by Walsh *et al.* [8], termed fluid-walled microfluidics, attempts to address the requirements of an ideal system. The technique shapes cell-culture media on the surface of standard Petri dishes, taking advantage of interfacial forces at the microscale that pin media firmly to the dish surface to create networks of conduits and sessile droplets in any 2D configuration. These networks are made by infusing media through a dispensing needle held just above the surface of the dish, and moving the needle to form the desired pattern, much like drawing with pen on paper. The system is then overlaid with a bioinert and biocompatible fluorocarbon (FC40) that prevents circuit evaporation and increases overall stability. This technique offers significant advantages over existing solutions. It is entirely open in nature so cells can be accessed anywhere within the circuit by simply inserting a pipet through the fluid walls which seal and self-heal around the pipet upon insertion and removal [9]. Walls are optically transparent as FC40 has a very similar refractive index to water, so cells can be imaged anywhere within circuits, unlike traditional solid-walled systems that have poor refractive properties near the walls [10]. Additionally, circuits usually take less than a minute to print, and can be reconfigured to isolate specific regions of interest [11],[12].

However, most of the fluid-walled microfluidic applications to date have revolved around static systems that do not require flow, while few proof-of-concept applications with flow demonstrated simple chemotaxis of bacteria [8] and continuous perfusion of cells [12]. As most cells within the body experience some form of flow [13], it is paramount to incorporate fluid flow to create microfluidic systems with physiological relevance. Fluid-walled systems have the particularity of being just that: systems with fluid and elastic

interfaces. As such, these walls morph in response to changes in pressure, generated in the presence of flow. This makes modelling and predicting fluid velocities and shear stresses to tune circuit parameters to biologists' specific requirements more difficult than in traditional solid-walled systems with fixed geometries. This thesis therefore searches to mathematically model such fluid-walled circuits so that flow characteristics may be predicted and controlled, to expand this technology to biomedical applications necessitating flow, and specifically apply it to chemotaxis, the study of directed cell migration.

Objectives

The overall aim of this thesis is to develop fluid-walled microfluidic circuits to study cell migration and address the following objectives:

1. Develop a mathematical model to predict and characterise fluid velocities and shear stresses in fluid-walled circuits when applying a pump-controlled flow rate, and implement a method to manipulate the magnitude and variation of these parameters by tuning circuit geometries.
2. Implement a technique to reconfigure microfluidic circuits to isolate specific cells of interest and in real-time using live microscopy.
3. Use the developed theoretical framework to design and operate passive and active circuits to study cell migration in response to concentration gradients of chemoattractants, and develop algorithms to track cells. Provide a theoretical basis for establishing concentration gradients within fluid-walled microfluidic circuits.

The thesis is structured in 6 chapters that directly address the presented objectives and finishes with a concluding chapter to summarise and discuss the work outlined and propose future developments.

Chapter 2 presents a brief literature review of microfluidic technology and its applications in cell biology. It outlines current advantages and limitations, and expands on the importance of flow to study cellular physiology and behaviour, specifically in the context of directed cell migration.

Chapter 3 introduces a semi-analytical model to accurately predict the varying height of fluid-walled conduits under flow. This then allows prediction of fluid velocities and shear stresses within single conduits and more complex vascular trees. These results are compared with experimental measurements to demonstrate the accuracy of the model, which simplifies to a simple power law. A method to control and create near-uniform shear stress distributions in conduits is implemented, which allows users to create circuits that fit their individual requirements.

Chapter 4 outlines a method to selectively isolate and retrieve cells of interest within flowing microfluidic devices. Using 3D-printed adaptors, conventional microscopes are converted into reconfiguring tools that can manipulate and re-shape fluid-walled circuits in real-time and with a precision of several microns. Cells can then be extracted for downstream analysis. The technique is applied here to investigate cell migration of mammalian and bacterial cells in response to concentration gradients and demonstrates that bacteria exhibit suicidal behaviours in response to highly concentrated antibiotics.

Chapter 5 presents passive and active fluid-walled circuits to study cell migration in response to concentration gradients established by diffusion. This chapter outlines a higher-throughput method to print 12 identical circuits onto conventional 35 mm Petri dishes, which can be further extended to fit 72 circuits in 6 well-plates. Cells are then tracked in real-time, taking advantage of the optical properties of fluid-walled systems, and their response to gradients of varying strength and concentration is analysed. The devices described seek to

address the existing limitations of chemotaxis studies, and provide new ways for biologists to interrogate genotypic and phenotypic differences of diverse cell populations.

Chapter 6 is the final in this thesis and discusses the results presented, summarises the advantages and limitations of the techniques introduced, and proposes future developments.

The work carried throughout this thesis resulted in the publication of the below 4 papers (2 co-lead author, 2 co-author):

1. C. Soitu, C. Deroy, A. A. Castrejón-Pita, P. R. Cook, and E. J. Walsh, "Using Fluid Walls for Single-Cell Cloning Provides Assurance in Monoclonality", *SLAS Technol.*, 2019, doi: 10.1177/2472630319891135.
2. C. Soitu, A. Feuerborn, C. Deroy, A. A. Castrejón-Pita, P. R. Cook, and E. J. Walsh, "Raising fluid walls around living cells", *Sci. Adv.*, vol. 5, no. 6, 2019, doi: 10.1126/sciadv.aav8002.
3. C. Soitu, N. Stovall-Kurtz, C. Deroy, A. A. Castrejón-Pita, P. R. Cook, and E. J. Walsh, "Jet-Printing Microfluidic Devices on Demand", *Adv. Sci.*, 2020, doi: 10.1002/advs.202001854.
4. C. Deroy, F. Nebuloni, P. R. Cook, and E. J. Walsh, "Microfluidics on Standard Petri Dishes for Bioscientists", *Small Methods*, 2021, doi: 10.1002/smtd.202100724, (In Press).

Additionally, the paper introduced in Chapter 3 is currently under review for publication (Microsystems and Nanoengineering), while the papers presented in Chapters 4 and 5 are being prepared for submission. Finally, a more detailed analysis of the work on bacterial chemotaxis discussed in chapter 4 is also being prepared for publication in a separate manuscript.

References

[1] C. Hansen and S. R. Quake, "Microfluidics in structural biology: smaller, faster… better," *Curr. Opin. Struct. Biol.*, vol. 13, no. 5, pp. 538–544, 2003, doi: https://doi.org/10.1016/j.sbi.2003.09.010.

[2] P. Yager *et al.*, "Microfluidic diagnostic technologies for global public health," *Nature*, vol. 442, no. 7101, pp. 412–418, 2006, doi: 10.1038/nature05064.

[3] E. K. Sackmann, A. L. Fulton, and D. J. Beebe, "The present and future role of microfluidics in biomedical research," *Nature*, vol. 507, no. 7491, pp. 181–189, 2014, doi: 10.1038/nature13118.

[4] Y. Wang *et al.*, "Systematic prevention of bubble formation and accumulation for long-term culture of pancreatic islet cells in microfluidic device," *Biomed. Microdevices*, vol. 14, no. 2, pp. 419–426, Apr. 2012, doi: 10.1007/s10544-011-9618-3.

[5] E. Berthier, E. W. Young, and D. Beebe, "Engineers are from PDMS-land, Biologists are from Polystyrenia," *Lab Chip*, vol. 12, no. 7, pp. 1224–1237, 2012, doi: 10.1039/c2lc20982a.

[6] S. Halldorsson, E. Lucumi, R. Gómez-Sjöberg, and R. M. T. Fleming, "Advantages and challenges of microfluidic cell culture in polydimethylsiloxane devices," *Biosens. Bioelectron.*, vol. 63, pp. 218–231, 2015, doi: https://doi.org/10.1016/j.bios.2014.07.029.

[7] G. V Kaigala, R. D. Lovchik, and E. Delamarche, "Microfluidics in the 'Open Space' for Performing Localized Chemistry on Biological Interfaces," *Angew. Chemie Int. Ed.*, vol. 51, no. 45, pp. 11224–11240, Nov. 2012, doi: 10.1002/anie.201201798.

[8] E. J. Walsh *et al.*, "Microfluidics with fluid walls," *Nat. Commun.*, vol. 8, no. 1, p. 816, 2017, doi: 10.1038/s41467-017-00846-4.

[9] C. Soitu *et al.*, "Microfluidic chambers using fluid walls for cell biology," *Proc. Natl. Acad. Sci.*, 2018, doi: 10.1073/pnas.1805449115.

[10] C. Soitu, C. Deroy, A. A. Castrejón-Pita, P. R. Cook, and E. J. Walsh, "Using Fluid Walls for Single-Cell Cloning Provides Assurance in Monoclonality," *SLAS Technol.*, 2019, doi:

10.1177/2472630319891135.

[11] C. Soitu, A. Feuerborn, C. Deroy, A. A. Castrejón-Pita, P. R. Cook, and E. J. Walsh, “Raising fluid walls around living cells,” *Sci. Adv.*, vol. 5, no. 6, 2019, doi: 10.1126/sciadv.aav8002.

[12] C. Soitu, N. Stovall-Kurtz, C. Deroy, A. A. Castrejón-Pita, P. R. Cook, and E. J. Walsh, “Jet-Printing Microfluidic Devices on Demand,” *Adv. Sci.*, 2020, doi: 10.1002/advs.202001854.

[13] D. Huber, A. Oskooei, X. Casadevall i Solvas, A. deMello, and G. V Kaigala, “Hydrodynamics in Cell Studies,” *Chem. Rev.*, vol. 118, no. 4, pp. 2042–2079, Feb. 2018, doi: 10.1021/acs.chemrev.7b00317.

Chapter 2: Literature Review

A brief history of microfluidics

Microfluidic technology was first introduced during the second half of the 20th century, presenting itself as a platform for the manipulation of fluids at the microscale. With the invention of inkjet printing in the 1950's alongside the transistor, microtechnology made its first appearance into the world, allowing the development of Micro Electromechanical Systems (MEMS) by the 1980's. These devices were first used for applications such as pressure sensors or printheads, and then led on to the development of micro-valves and micro-pumps, made using the glass and silicon-based manufacturing techniques used at the time. A decade later, MEMS technologies started to focus on biological and chemical applications, and with the support of the Defence Advanced Research Projects Agency (DARPA), tools for genomic research, and biological and chemical warfare agent detection systems were implemented [1]. This led to the development of a new field, namely Biomedical-MEMS (Bio-MEMS). Rather than utilising glass and silicon as the underlying fabrication material, microfluidic devices veered towards polymers, and specifically polydimethylsiloxane (PDMS), due to their attractive properties: these are optically transparent, soft elastomers, permeable to gases, which makes them ideal for microscopy imaging, casting onto photolithographed moulds, and cell culturing [2], [3].

Movement towards Lab-on-a-Chip systems

The application of microfluidics then began to focus on a new type of technology, namely Lab-on-a-Chip (LoC), also known as Micro Total Analysis Systems (micro-TAS or µTAS). LoC (and micro-TAS) devices allow users to perform analyses usually carried out in a lab on a

miniaturized scale. These commonly take the shape of computer chip-sized devices – hence their name – and can perform operations such as PCR and DNA sequencing [4], [5], disease detection and diagnosis [6], drug delivery [7], and can be used for the creation of new biomedical reagents and the development of novel cellular and biochemical assays [8]. Tiny samples can then be analysed directly on the platform, without requiring specialised and expensive laboratory equipment, although there is often the need for additional supporting infrastructure beyond that typically available in biology labs (e.g., syringe pumps and micro sensors) [2], [5], [9]. Furthermore, the behaviour of fluids at the microscale provides a change in the physics for the manipulation of samples, which can make processes such as mixing reagents and creating chemical reactions much more controlled, and turbulence induced mixing more difficult [10]–[12]. Waste is also greatly reduced, lowering the overall cost of running experiments, as very small amounts of reagents are required [13]; a key consideration in biology/chemical experiments where reagents are often expensive and hazardous.

Microfluidic organ models for drug testing and disease modelling

More recently, in the last decade, a new branch of LoC devices made its first appearance, namely Organs-on-a-Chip (OoC). Spanning from a nationally funded initiative in the US led by DARPA and the National Institutes of Health (NIH), the aim of this new research field was to develop micro-devices harnessing LoC technology, to create biomimetic platforms with the capacity to mimic human organ functions. With the end goal being the creation of an interconnected Human-on-a-Chip, various OoC devices began to emerge, with, most famously, the Heart-on-a-Chip and Lung-on-a-Chip [14], [15]. It was shown that such devices could be used as predictive models for drug testing; the Heart-on-a-Chip device obtained similar results to in vitro and rat-model studies for the evaluation of the effects of

pharmacological agents (isoproterenol) on diseased cardiac tissues (dose response study for the treatment of bradycardia), while the Lung-on-a-Chip provided new insights into lung function, such as the increased epithelial and endothelial uptake of silica nanoparticles during periods of augmented cyclic mechanical strain. These newly developed testing platforms therefore offered unique means to study complex biological processes, drug response and delivery, disease models, all incorporated onto a chip-sized device. Additionally, they presented an alternative solution to animal models, having the ability to incorporate patient-specific cells. Together with the advent of induced pluripotent stem cell (iPSC) research, the possibilities seemed endless; any cell-type could theoretically be generated to reproduce disease models from human patients [16]–[18] and tested directly onto the portable and re-usable platforms. Moreover, the simplicity and high-throughput techniques for their fabrication made these very cheap to manufacture, giving them the potential to significantly reduce the cost of pharmaceutical research, in which the cost of developing new drugs can exceed 2.5 billion dollars [19]. Since then, many more OoC platforms have been developed, spanning from Kidney [20], Gut [21], Liver-on-a-Chip models [22], [23], to a Blood-Brain Barrier-on-a-Chip [24].

Challenges facing microfluidic adoption in the biomedical community

Still, the use of LoC devices in biological laboratories and their adoption by the life-science community has remained limited; reasons cited for this lack of uptake include the technical complexity of the devices, high failure rates associated with gas-bubbles, biocompatibility concerns with the use of PDMS and the equipment/time/expertise requirements for their operation and manufacture. Technical complexity of devices is easily illustrated by microfluidic systems designed to perform routine biological assays such as

reverse-transcriptase PCR (RT-PCR) [25] and single-cell sequencing [26], which involve many external pumps, tubes, and syringes. Overall, microfluidics has remained an engineering-focused discipline, as around 90% of microfluidic papers are published in engineering peer-reviewed journals [27]–[29]. More effort is therefore needed to promote collaborative development between engineers and biologists, to ensure technologies are suited to, and therefore used, in biomedicine.

Open microfluidics and the advent of fluid-walled microfluidics

One implemented development to tackle the challenging sample handling in microfluidic devices was the introduction of open microfluidic systems. The need to confine fluids by solid walls is eliminated by removing at least one of the solid boundaries such as the cover, allowing users to access samples directly over the open platform [30]–[33]. As this may lead to issues such as evaporation, samples are often overlaid with an immiscible liquid (typically oil). One such platform is a microfluidic encapsulation device for the analysis of single cells, developed by Shemesh *et al.* [34]. The liquid walls and ceilings confining the aqueous phase allow the microfluidic platform to retain its open format [34], [35]. Although open systems address the sample accessibility limitations of traditional devices, they are mostly made of PDMS, with some alternatives using polystyrene [36] that still require longer manufacturing times.

Recently, Walsh *et al.* [37] developed a new kind of open microfluidic system using only materials common to biologists; tissue culture media and cell culture dishes. The technique uses a three-axis traverse that holds a dispensing needle above the surface of a Petri dish to shape fluids in two ways: forward printing [37] and jetting [38]. The needle is itself connected via tubing to a syringe held on a syringe pump. In forward printing, the

syringe is loaded with culture medium which is infused through the needle above the surface of a virgin dish. As the needle moves over the dish in a desired pattern, media is firmly pinned to the surface by interfacial forces and forms a circuit. This circuit is then overlaid with FC40, a bioinert and biocompatible fluorocarbon, to prevent evaporation. In jetting, a dish is covered in a thin skim of media which is itself overlaid with a layer of FC40. The syringe is this time loaded with FC40 and jets a thin stream of FC40 through the needle. When this FC40 jet contacts the surface of the dish, it displaces the media allowing the overlaying FC40 to replace it as it wets the dish better than media. This creates a fluid wall at the media:FC40 interface. Moving the needle over the dish then creates the outline of a circuit. While forward printing can be used to create narrow conduits by using smaller needles, the risk of evaporation becomes a limiting factor as printing times take longer. In contrast, jetting eliminates the risk of evaporation as conduits are printed directly under FC40. Moreover, narrow conduits and small features are more easily jetted as jets are much thinner than needles (typically less than 100 µm wide). Both techniques, offering versatility and ease of use, have the unique ability to generate rapid circuit prototypes within minutes, and can be used to perform cellular assays such as (but not limited to) chemotaxis of bacterial cells [37], single cell cloning, cryopreservation, transfection, and genome editing [39]. Moreover, they eliminate concerns of biocompatibility and air bubble related failures. Other similar fluid-walled systems have also been implemented to detect vascular endothelial growth factor via rolling circle amplification [40], or used exclusive liquid repellency to study the dispersion of fungal biofilms [41]. Altogether, fluid-walled technology may now be harnessed to implement OoC devices that more closely mimic *in vivo* conditions without the disadvantages of traditional methods.

The importance of flow in cell culture

Cells have traditionally been grown in vitro on the surface of agar plates and cell culture dishes or suspended in static or well-shaken liquid cultures. These experimental culture conditions have proved invaluable for establishing the foundations of microbial genetics and cell biology, but they fall short of capturing several critical features of cells' natural environments, and so they have limited potential for studying cell behaviour and ecology [42]. One such feature is chemical heterogeneity: agar plates and well-shaken liquid cultures typically expose cells to uniform chemical environments, which are rare in nature. Indeed, there is increasing evidence that complex chemical environments can influence many important processes including nutrient cycling in marine ecosystems [43], [44], the evolution of antibiotic resistance [45], [46], and key developmental processes [47], [48]. Another major feature that is lacking from traditional study methods is fluid flow, which is common in many natural habitats, including soil, freshwater, and marine environments [49]. Furthermore, many host-associated microorganisms also experience flow, for example within host vascular systems and intestinal tracts. Many of these microorganisms have clear adaptations to flow that are often critical for their ability to survive and impact their hosts [50]–[53]. Both chemical heterogeneity and fluid flow therefore have far-reaching importance for cell biology and ecology, and this necessitates moving away from an over-reliance on traditional study methods.

Chemotaxis: the study of directed cell migration

When cells experience environments with heterogeneous chemical signals, they often respond by migrating. The directed migration of cells in response to chemical concentration gradients is known as chemotaxis and is essential in regulating homeostasis [54]. Studying

chemotaxis *in vitro* therefore requires the ability to create and maintain stable concentration gradients and incorporate flow to mimic physiological conditions. Concentration gradients are typically obtained in microfluidic circuits by flowing two laminar streams of fluid side by side, one containing a chemoeffector, and allowing diffusion between the streams to generate a concentration gradient of that chemoeffector. While traditional microfluidic systems have been designed for chemotaxis studies [55]–[58], fluid-walled systems are currently limited in their ability to create well-defined flowing environments. As solid-walled systems have fixed geometries, solutions exist to determine fluid velocities and shear stresses inside microfluidic channels with various cross-sections [59]–[61]. Fluid-walled circuits, on the other hand, have elastic interfaces that morph in response to changes in pressure [37], [38]. As a result, when fluid flows through a fluid-walled conduit, conduit height decreases from the point of highest pressure (typically where a needle infuses fluid) to the point of lowest pressure (the conduit exit). The changing cross-sectional geometry of the conduit thus makes it difficult to predict fluid velocity, shear stress, gradient strength and width, and evaluate their impact on cell behaviour and physiology. It is therefore crucial to accurately predict and quantify fluid-walled conduits experiencing flow to ensure that culture conditions and parameters are set to the requirements of biologists and make this technology accessible to the wider biomedical community. A method to create well-defined heterogeneous environments for chemotaxis studies would then allow users to benefit from the multiple advantages of fluid-walled microfluidics, with the potential to isolate specific sub-populations of cells that exhibit phenotypic differences, all in real-time and without interrupting flows.

References

[1] G. M. Whitesides, “The origins and the future of microfluidics,” *Nature*, vol. 442, no. 7101, pp. 368–373, 2006, doi: 10.1038/nature05058.

[2] S. Haeberle and R. Zengerle, “Microfluidic platforms for lab-on-a-chip applications,” *Lab Chip*, vol. 7, no. 9, pp. 1094–1110, 2007, doi: 10.1039/B706364B.

[3] J. Friend and L. Yeo, “Fabrication of microfluidic devices using polydimethylsiloxane,” *Biomicrofluidics*, vol. 4, no. 2, p. 26502, Mar. 2010, doi: 10.1063/1.3259624.

[4] S. J. Lee and S. Y. Lee, “Micro total analysis system (μ-TAS) in biotechnology,” *Appl. Microbiol. Biotechnol.*, vol. 64, no. 3, pp. 289–299, 2004, doi: 10.1007/s00253-003-1515-0.

[5] M. L. Kovarik *et al.*, “Micro Total Analysis Systems for Cell Biology and Biochemical Assays,” *Anal. Chem.*, vol. 84, no. 2, pp. 516–540, Jan. 2012, doi: 10.1021/ac202611x.

[6] M. T. Guler, Z. Isiksacan, M. Serhatlioglu, and C. Elbuken, “Self-powered disposable prothrombin time measurement device with an integrated effervescent pump,” *Sensors Actuators B Chem.*, vol. 273, pp. 350–357, 2018, doi: https://doi.org/10.1016/j.snb.2018.06.042.

[7] S. T. Sanjay *et al.*, “Recent advances of controlled drug delivery using microfluidic platforms,” *Adv. Drug Deliv. Rev.*, vol. 128, pp. 3–28, 2018, doi: https://doi.org/10.1016/j.addr.2017.09.013.

[8] A. Webster, J. Greenman, and S. J. Haswell, “Development of microfluidic devices for biomedical and clinical application,” *J. Chem. Technol. Biotechnol.*, vol. 86, no. 1, pp. 10–17, Jan. 2011, doi: https://doi.org/10.1002/jctb.2482.

[9] E. W. K. Young and D. J. Beebe, “Fundamentals of microfluidic cell culture in controlled microenvironments,” *Chem. Soc. Rev.*, vol. 39, no. 3, pp. 1036–1048, Mar. 2010, doi: 10.1039/b909900j.

[10] C. Hansen and S. R. Quake, “Microfluidics in structural biology: smaller, faster… better,” *Curr. Opin. Struct. Biol.*, vol. 13, no. 5, pp. 538–544, 2003, doi:

https://doi.org/10.1016/j.sbi.2003.09.010.

[11] C.-Y. Lee, C.-L. Chang, Y.-N. Wang, and L.-M. Fu, “Microfluidic mixing: a review,” *Int. J. Mol. Sci.*, vol. 12, no. 5, pp. 3263–3287, 2011, doi: 10.3390/ijms12053263.

[12] K. Ward and Z. H. Fan, “Mixing in microfluidic devices and enhancement methods,” *J. Micromech. Microeng.*, vol. 25, no. 9, p. 94001, Sep. 2015, doi: 10.1088/0960-1317/25/9/094001.

[13] S. K. Tiwari, S. Bhat, and K. K. Mahato, “Design and Fabrication of Low-cost Microfluidic Channel for Biomedical Application,” *Sci. Rep.*, vol. 10, no. 1, p. 9215, 2020, doi: 10.1038/s41598-020-65995-x.

[14] A. Agarwal, J. A. Goss, A. Cho, M. L. McCain, and K. K. Parker, “Microfluidic heart on a chip for higher throughput pharmacological studies,” *Lab Chip*, vol. 13, no. 18, pp. 3599–3608, Sep. 2013, doi: 10.1039/c3lc50350j.

[15] D. Huh, B. D. Matthews, A. Mammoto, M. Montoya-Zavala, H. Y. Hsin, and D. E. Ingber, “Reconstituting Organ-Level Lung Functions on a Chip,” *Science (80-.).*, vol. 328, no. 5986, pp. 1662 LP – 1668, Jun. 2010, doi: 10.1126/science.1188302.

[16] K. Takahashi and S. Yamanaka, “Induction of Pluripotent Stem Cells from Mouse Embryonic and Adult Fibroblast Cultures by Defined Factors,” *Cell*, vol. 126, no. 4, pp. 663–676, 2006, doi: https://doi.org/10.1016/j.cell.2006.07.024.

[17] K. Takahashi *et al.*, “Induction of Pluripotent Stem Cells from Adult Human Fibroblasts by Defined Factors,” *Cell*, vol. 131, no. 5, pp. 861–872, 2007, doi: https://doi.org/10.1016/j.cell.2007.11.019.

[18] S. Yamanaka, “Induced Pluripotent Stem Cells: Past, Present, and Future,” *Cell Stem Cell*, vol. 10, no. 6, pp. 678–684, 2012, doi: https://doi.org/10.1016/j.stem.2012.05.005.

[19] J. Avorn, “The $2.6 Billion Pill — Methodologic and Policy Considerations,” *N. Engl. J. Med.*, vol. 372, no. 20, pp. 1877–1879, May 2015, doi: 10.1056/NEJMp1500848.

[20] M. J. Wilmer, C. P. Ng, H. L. Lanz, P. Vulto, L. Suter-Dick, and R. Masereeuw, “Kidney-on-a-

Chip Technology for Drug-Induced Nephrotoxicity Screening," *Trends Biotechnol*, vol. 34, no. 2, pp. 156–170, 2016, doi: 10.1016/j.tibtech.2015.11.001.

[21] A. Bein *et al.*, "Microfluidic Organ-on-a-Chip Models of Human Intestine," *Cell. Mol. Gastroenterol. Hepatol.*, vol. 5, no. 4, pp. 659–668, Apr. 2018, doi: 10.1016/j.jcmgh.2017.12.010.

[22] B. Delalat *et al.*, "Microengineered Bioartificial Liver Chip for Drug Toxicity Screening," *Adv. Funct. Mater.*, vol. 28, no. 28, p. 1801825, 2018, doi: doi:10.1002/adfm.201801825.

[23] M. Gröger, J. Dinger, M. Kiehntopf, F. T. Peters, U. Rauen, and A. S. Mosig, "Preservation of Cell Structure, Metabolism, and Biotransformation Activity of Liver-On-Chip Organ Models by Hypothermic Storage," *Adv. Healthc. Mater.*, vol. 7, no. 2, p. 1700616, 2018, doi: doi:10.1002/adhm.201700616.

[24] M. W. van der Helm, A. D. van der Meer, J. C. T. Eijkel, A. van den Berg, and L. I. Segerink, "Microfluidic organ-on-chip technology for blood-brain barrier research," *Tissue barriers*, vol. 4, no. 1, pp. e1142493–e1142493, Jan. 2016, doi: 10.1080/21688370.2016.1142493.

[25] D. J. Eastburn, A. Sciambi, and A. R. Abate, "Ultrahigh-Throughput Mammalian Single-Cell Reverse-Transcriptase Polymerase Chain Reaction in Microfluidic Drops," *Anal. Chem.*, vol. 85, no. 16, pp. 8016–8021, Aug. 2013, doi: 10.1021/ac402057q.

[26] A. M. Streets *et al.*, "Microfluidic single-cell whole-transcriptome sequencing," *Proc. Natl. Acad. Sci. U. S. A.*, vol. 111, no. 19, pp. 7048–7053, May 2014, doi: 10.1073/pnas.1402030111.

[27] E. K. Sackmann, A. L. Fulton, and D. J. Beebe, "The present and future role of microfluidics in biomedical research," *Nature*, vol. 507, no. 7491, pp. 181–189, 2014, doi: 10.1038/nature13118.

[28] E. Berthier, E. W. Young, and D. Beebe, "Engineers are from PDMS-land, Biologists are from Polystyrenia," *Lab Chip*, vol. 12, no. 7, pp. 1224–1237, 2012, doi: 10.1039/c2lc20982a.

[29] T. A. Duncombe, A. M. Tentori, and A. E. Herr, "Microfluidics: reframing biological enquiry.,"

Nat. Rev. Mol. Cell Biol., vol. 16, no. 9, pp. 554–567, Sep. 2015, doi: 10.1038/nrm4041.

[30] G. V Kaigala, R. D. Lovchik, and E. Delamarche, "Microfluidics in the 'Open Space' for Performing Localized Chemistry on Biological Interfaces," *Angew. Chemie Int. Ed.*, vol. 51, no. 45, pp. 11224–11240, Nov. 2012, doi: 10.1002/anie.201201798.

[31] J. Berthier, K. Brakke, and E. Berthier, *Open Microfluidics*. Wiley, 2016.

[32] S. B. Berry *et al.*, "Upgrading well plates using open microfluidic patterning," *Lab Chip*, vol. 17, no. 24, pp. 4253–4264, 2017, doi: 10.1039/C7LC00878C.

[33] J. Berthier, A. B. Theberge, and E. Berthier, "Open-Channel Microfluidics," *Fundamentals and applications*. Morgan & Claypool Publishers, 2019, doi: 10.1088/2053-2571/ab21ca.

[34] J. Shemesh *et al.*, "Stationary nanoliter droplet array with a substrate of choice for single adherent/nonadherent cell incubation and analysis," *Proc. Natl. Acad. Sci.*, vol. 111, no. 31, pp. 11293–11298, 2014, doi: 10.1073/pnas.1404472111.

[35] G.-S. Du, J.-Z. Pan, S.-P. Zhao, Y. Zhu, J. M. J. den Toonder, and Q. Fang, "Cell-Based Drug Combination Screening with a Microfluidic Droplet Array System," *Anal. Chem.*, vol. 85, no. 14, pp. 6740–6747, 2013, doi: 10.1021/ac400688f.

[36] J. Yu *et al.*, "Reconfigurable open microfluidics for studying the spatiotemporal dynamics of paracrine signalling.," *Nat. Biomed. Eng.*, vol. 3, no. 10, pp. 830–841, Oct. 2019, doi: 10.1038/s41551-019-0421-4.

[37] E. J. Walsh *et al.*, "Microfluidics with fluid walls," *Nat. Commun.*, vol. 8, no. 1, p. 816, 2017, doi: 10.1038/s41467-017-00846-4.

[38] C. Soitu, N. Stovall-Kurtz, C. Deroy, A. A. Castrejón-Pita, P. R. Cook, and E. J. Walsh, "Jet-Printing Microfluidic Devices on Demand," *Adv. Sci.*, 2020, doi: 10.1002/advs.202001854.

[39] C. Soitu *et al.*, "Microfluidic chambers using fluid walls for cell biology," *Proc. Natl. Acad. Sci.*, 2018, doi: 10.1073/pnas.1805449115.

[40] S. Feng, S. Mao, J. Dou, W. Li, H. Li, and J.-M. Lin, "An open-space microfluidic chip with fluid walls for online detection of VEGF via rolling circle amplification," *Chem. Sci.*, vol. 10, no. 37,

pp. 8571–8576, 2019, doi: 10.1039/C9SC02974E.

[41] C. Li *et al.*, "Under oil open-channel microfluidics empowered by exclusive liquid repellency," *Sci. Adv.*, vol. 6, no. 16, p. eaay9919, Apr. 2020, doi: 10.1126/sciadv.aay9919.

[42] D. Huber, A. Oskooei, X. Casadevall i Solvas, A. deMello, and G. V Kaigala, "Hydrodynamics in Cell Studies," *Chem. Rev.*, vol. 118, no. 4, pp. 2042–2079, Feb. 2018, doi: 10.1021/acs.chemrev.7b00317.

[43] R. Stocker, J. R. Seymour, A. Samadani, D. E. Hunt, and M. F. Polz, "Rapid chemotactic response enables marine bacteria to exploit ephemeral microscale nutrient patches," *Proc. Natl. Acad. Sci.*, vol. 105, no. 11, pp. 4209 LP – 4214, Mar. 2008, doi: 10.1073/pnas.0709765105.

[44] R. Stocker, "Marine Microbes See a Sea of Gradients," *Science (80-.).*, vol. 338, no. 6107, pp. 628 LP – 633, Nov. 2012, doi: 10.1126/science.1208929.

[45] Q. Zhang *et al.*, "Acceleration of emergence of bacterial antibiotic resistance in connected microenvironments.," *Science*, vol. 333, no. 6050, pp. 1764–1767, Sep. 2011, doi: 10.1126/science.1208747.

[46] R. Hermsen, J. B. Deris, and T. Hwa, "On the rapidity of antibiotic resistance evolution facilitated by a concentration gradient," *Proc. Natl. Acad. Sci.*, vol. 109, no. 27, pp. 10775 LP – 10780, Jul. 2012, doi: 10.1073/pnas.1117716109.

[47] D. Dormann and C. J. Weijer, "Chemotactic cell movement during Dictyostelium development and gastrulation," *Curr. Opin. Genet. Dev.*, vol. 16, no. 4, pp. 367–373, 2006, doi: https://doi.org/10.1016/j.gde.2006.06.003.

[48] M. Singh, C. Berkland, and M. S. Detamore, "Strategies and Applications for Incorporating Physical and Chemical Signal Gradients in Tissue Engineering," *Tissue Eng. Part B Rev.*, vol. 14, no. 4, pp. 341–366, Sep. 2008, doi: 10.1089/ten.teb.2008.0304.

[49] R. Rusconi and R. Stocker, "Microbes in flow," *Curr. Opin. Microbiol.*, vol. 25, pp. 1–8, 2015, doi: https://doi.org/10.1016/j.mib.2015.03.003.

[50] Y. Meng *et al.*, "Upstream migration of Xylella fastidiosa via pilus-driven twitching motility," *J. Bacteriol.*, vol. 187, no. 16, pp. 5560–5567, Aug. 2005, doi: 10.1128/JB.187.16.5560-5567.2005.

[51] H. A. Stone, "The Mechanical World of Microorganisms," *Bioscience*, vol. 60, no. 11, pp. 950–951, Dec. 2010, doi: 10.1525/bio.2010.60.11.12.

[52] Y. Shen, A. Siryaporn, S. Lecuyer, Z. Gitai, and H. A. Stone, "Flow directs surface-attached bacteria to twitch upstream," *Biophys. J.*, vol. 103, no. 1, pp. 146–151, Jul. 2012, doi: 10.1016/j.bpj.2012.05.045.

[53] A. Persat *et al.*, "The mechanical world of bacteria," *Cell*, vol. 161, no. 5, pp. 988–997, May 2015, doi: 10.1016/j.cell.2015.05.005.

[54] X. Yang, D. Dormann, A. E. Münsterberg, and C. J. Weijer, "Cell Movement Patterns during Gastrulation in the Chick Are Controlled by Positive and Negative Chemotaxis Mediated by FGF4 and FGF8," *Dev. Cell*, vol. 3, no. 3, pp. 425–437, 2002, doi: https://doi.org/10.1016/S1534-5807(02)00256-3.

[55] T. Ahmed, T. S. Shimizu, and R. Stocker, "Microfluidics for bacterial chemotaxis," *Integr. Biol.*, vol. 2, no. 11–12, pp. 604–629, 2010, doi: 10.1039/C0IB00049C.

[56] B. J. Kim and M. Wu, "Microfluidics for mammalian cell chemotaxis," *Ann. Biomed. Eng.*, vol. 40, no. 6, pp. 1316–1327, Jun. 2012, doi: 10.1007/s10439-011-0489-9.

[57] J. Song *et al.*, "A microfluidic device for studying chemotaxis mechanism of bacterial cancer targeting," *Sci. Rep.*, vol. 8, no. 1, p. 6394, 2018, doi: 10.1038/s41598-018-24748-7.

[58] W. Zhao, H. Zhao, M. Li, and C. Huang, "Microfluidic devices for neutrophil chemotaxis studies," *J. Transl. Med.*, vol. 18, no. 1, p. 168, 2020, doi: 10.1186/s12967-020-02335-7.

[59] M. Bahrami, M. M. Yovanovich, and J. R. Culham, "Pressure Drop of Fully-Developed, Laminar Flow in Microchannels of Arbitrary Cross-Section," *J. Fluids Eng.*, vol. 128, no. 5, pp. 1036–1044, Jan. 2006, doi: 10.1115/1.2234786.

[60] K. Zografos, R. W. Barber, D. R. Emerson, and M. S. N. Oliveira, "A design rule for constant

depth microfluidic networks for power-law fluids," *Microfluid. Nanofluidics*, vol. 19, no. 3, pp. 737–749, 2015, doi: 10.1007/s10404-015-1598-9.

[61] X. Lu, M. M. Galarneau, J. M. Higgins, and D. K. Wood, "A microfluidic platform to study the effects of vascular architecture and oxygen gradients on sickle blood flow," *Microcirculation*, vol. 24, no. 5, p. 10.1111/micc.12357, Jul. 2017, doi: 10.1111/micc.12357.

Chapter 3: Predicting flows through microfluidic circuits with fluid walls

Authors: Cyril Deroy, Nicholas Stovall-Kurtz, Federico Nebuloni, Cristian Soitu, Peter R. Cook, Edmond J. Walsh

Under review at time of thesis submission (October 03, 2021): Microsystems and Nanoengineering (Submitted August 08, 2021)

Published: Microsystems and Nanoengineering (November 18, 2021), 7, 93 doi:10.1038/s41378-021-00322-6

Abstract

The aqueous phase in traditional microfluidic circuits is usually confined by solid walls; flows through such circuits can often be predicted accurately. As solid walls limit access, open systems are being developed in which the aqueous phase is partly bounded by fluid walls (interfaces with air or immiscible liquids). However, such fluid walls inevitably morph due to pressure gradients during flow, so predicting flow fields remains challenging. We recently developed a version of open microfluidics suitable for live-cell biology in which the aqueous phase is confined by an interface with an immiscible and bioinert fluorocarbon (FC40). Here, we find common media additives (fetal bovine serum, serum replacement) induce elastic no-slip boundaries at this interface, and develop a semi-analytical model enabling prediction of flow fields. We confirm experimentally the accuracy of the model applied to single conduits and fractal vascular trees, and demonstrate how flow fields and shear stresses can be controlled to suit individual applications in cell biology.

Introduction

Flow is important in many biomedical applications, as cell survival and behaviour depend so critically on it [1]. It is also essential in organ-on-a-chip devices [2]–[4] where cells are perfused continuously to mimic in vivo conditions, and when studying the effects of transient shear stress on cells [5]. Defining flow fields in these systems is thus essential. The aqueous phase in conventional microfluidic devices is typically surrounded by solid walls (made, for example, of polydimethylsiloxane, PDMS), and flows through them can usually be predicted [6]–[8]. For example, equations based on pipe flow can be adapted for conduits with arbitrary cross-sections [9], and to model vascular circuits with branches of varying widths [10]–[13]. As solid walls restrict access, open microfluidics is being developed where parts of walls are replaced by interfaces with air or immiscible liquids [14]–[16], and equations describing rivulet [17], multiphase [18], and droplet-based flows [19] through conduits with free surfaces have been described.

Recently, an open system termed fluid-walled microfluidics has proven particularly suited to biomedical applications. Circuits are built using just the cell-culture media and Petri dishes that biologists use daily, plus the bioinert cell-friendly and immiscible fluorocarbon, FC40; the two liquids sitting in virgin dishes are reshaped into circuits in seconds [20]–[22]. Media in these circuits is confined by FC40 walls held by interfacial forces, and aqueous conduits have cross-sectional profiles of segments of circles that morph as pressures change during flow. Although predicting flows through such morphing cross-sections is challenging, asymptotic methods have been introduced and validated using numerical simulations for transient (passively-pumped) systems [23]. However, development of simpler methods, and their experimental validation, is still necessary. Here, we characterise how fluid walls change

during flow through a simple open-ended conduit. Surprisingly, we find that a common media component – fetal bovine serum (FBS) – induces elastic no-slip boundaries at the media:FC40 interface. We then develop a semi-analytical model which results in a simple power-law; it enables prediction of flow fields and shear stresses throughout a conduit. Finally, we confirm experimentally the accuracy of the model applied to single conduits and complex vascular trees.

Results

Circuit fabrication and operation

Microfluidic circuits are fabricated using a microjet [20]. A thin layer of cell-growth medium (i.e., DMEM) plus 10% fetal bovine serum (FBS) in a virgin Petri dish is overlaid with FC40, and the tip of a needle held by a 3-way traverse (a 'printer') is lowered through the FC40 until just above the medium (Fig. 1A). The needle is filled with FC40 and connected to a syringe pump; then, starting the pump jets FC40 through medium on to the bottom of the dish, and the submerged jet sweeps some medium aside. As FC40 wets polystyrene better than medium, some fluorocarbon remains stuck to the bottom. Moving the needle above the dish in the desired 2D pattern creates a fluid FC40 wall on the bottom of the dish. We begin with a simple open-ended conduit (Fig. 1Bi), where medium is infused through a dispensing tube/needle inserted through the fluid ceiling of the conduit (Fig. 1Biii); it flows down the conduit, and out through the open end into the rest of the dish (the sink; Fig. 1Ci).

The challenge: predicting flows when fluid walls morph

Unlike the solid walls in traditional microfluidic circuits that have fixed shapes, FC40 walls/ceilings morph during flow above an unchanging footprint. The curvature of confining FC40 walls is determined by interfacial forces, and hence can change during flow. As the Bond number is low, conduits have cross-sections like segments of circles; walls are pinned to the surface of the dish along the triple contact-line where medium, FC40, and polystyrene meet (Fig. 1C). Analogous to horizontal pipe-flow, there is a pressure gradient in the flow direction along a conduit, and hence fluid walls morph in response to this gradient. Laplace pressure at any axial position along the conduit is given by $\Delta P_{conduit} = \frac{\gamma}{R}$ (where γ is the interfacial

tension and R the radius of curvature). As ΔP is inversely proportional to R, a decrease in P results in an increase in R, which translates into a decrease in conduit height (defined as h_{max} in Fig. 1Ciii). Thus, conduit height falls from input end (high pressure) to open end (low pressure; contrast the dark blue sections in Fig. 1Cii and Fig. 1Ciii). Our challenge is to develop a semi-analytical solution that enables prediction of velocity and shear stress distributions throughout such conduits.

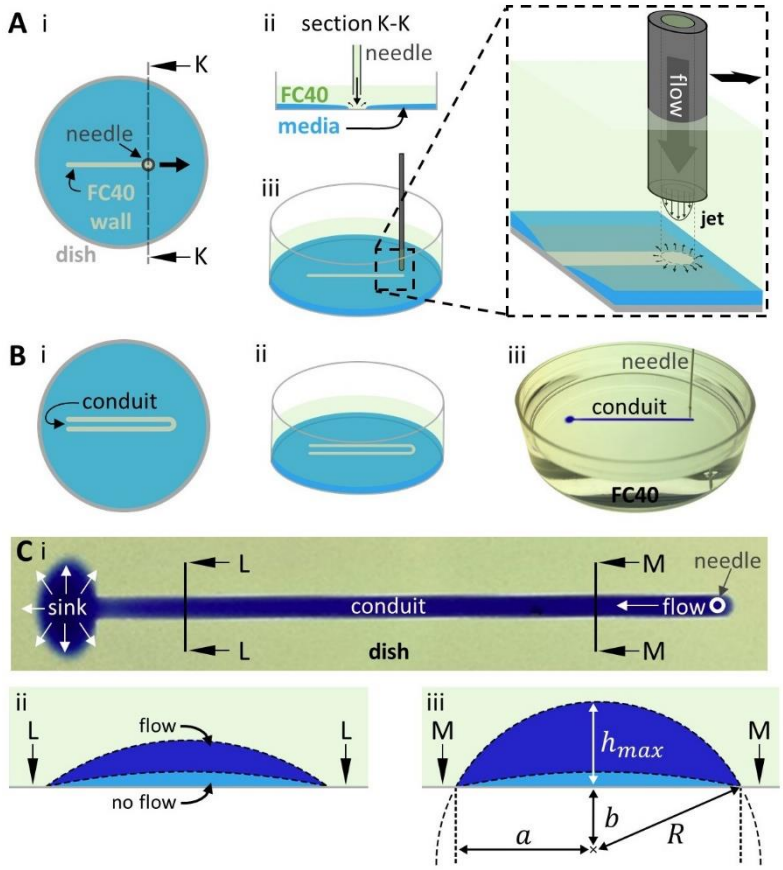


Fig. 1. Workflow. (A) Building one straight fluid wall by jetting. **(i)** After wetting a virgin dish with medium and overlaying immiscible FC40, a dispensing needle is lowered until just above the medium where it jets FC40 on to the bottom. As the needle moves laterally, the submerged jet sweeps medium aside to leave an FC40 wall pinned to the bottom. **(ii)** 2D view of section K-K. **(iii)** 3D side view of jet. **(B)** Operation of a simple circuit – an open-ended conduit. **(i)** 2D and **(ii)** 3D view of the conduit. **(iii)** A syringe pump drives

dye (added to aid visualization) through the conduit; the dye front has just reached the open end of the conduit and is emptying into the rest of the dish (the sink). **(C)** Conduit geometry. **(i)** Top view of conduit without needle (position indicated). **(ii)** Changes in conduit cross section at L-L in Ci during flow. Before initiating flow, the conduit is bounded by FC40 walls shaped like a spherical cap (light blue). During flow, walls morph due to the increased pressure and conduit height increases (dark blue). **(iii)** Changes at M-M. Before flow, the cross-section is like that at L-L; during flow, h_{max} increases more than at L-L as the pressure is higher. R = radius of curvature of cap. b = distance from centre of cap to dish surface. a = conduit half-width.

Measuring conduit height

As conduit height reflects local pressure, we first develop a method to measure it. Medium containing red fluorescent beads is perfused through a conduit sitting on an inverted microscope (Fig. 2A); most beads travel steadily through the conduit, but some remain stationary, stuck to the conduit floor (the dish) or ceiling (the media:FC40 interface; Fig. 2B). In still photographs taken with the focus on floor or ceiling, the moving majority appear as blurred streamlines due to the long exposure, and the static minority as bright in-focus dots (Fig. 2C). After measuring the distance of a stationary bead stuck to the ceiling from the conduit centreline (z), conduit height (h_{max}) is calculated using geometry (Fig. 2B) and correcting for refractive effects (Supplementary Information).

FBS creates a no-slip boundary at media:FC40 interfaces

As the conduit floor is solid, the no-slip boundary condition applies there and results in zero velocity at the medium:polystyrene interface; therefore, it is unsurprising that beads on the bottom remain stationary (Fig. 2Ci). However, it is surprising some are stationary at the upper interface (Fig. 2Cii) which one might anticipate would be in motion (the viscosity

ratio of FC40:medium is ~4). Testing medium with and without FBS shows that adding serum induces the no-slip condition. As the constitution of FBS is ill-defined and varies from batch to batch, we replaced it with the better-defined KnockOut serum replacement (SR) and found it has the same effect. It was previously shown that cells attach and grow at the interface between fluorocarbon fluids and tissue culture medium [24], [25]. As with solid surfaces, cells interact with a monolayer of denatured proteins that adsorb to the interface. This monolayer typically consists of serum proteins (of which there is an abundance of albumin), which allow cells to attach and thus presumably induce the no-slip condition in these liquid-liquid interfaces. In our experiments, medium flow past static FC40, so we reversed the situation; FC40 is jetted through FC40 overlaying a static drop containing beads. In the absence of FBS, FC40 flow induces rapid bead motion as forces are transmitted through the interface; on adding FBS to the drop, beads immediately stop moving (Movie S1). We conclude that FBS and SR (two of the most widely used additives in mammalian cell-culture media) rapidly induce formation of a no-slip boundary. We now apply this boundary condition to develop a theoretical model.

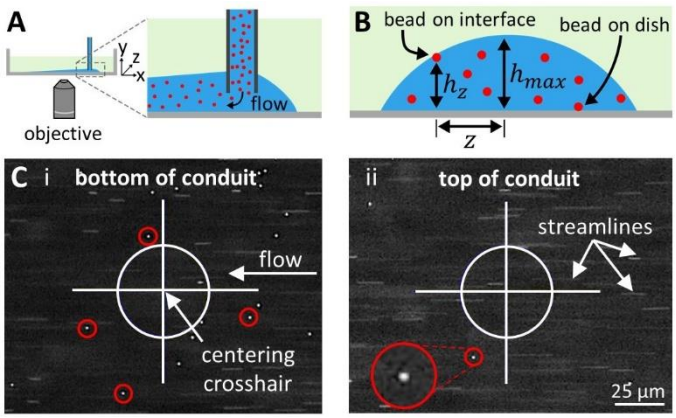


Fig. 2. Measuring conduit heights experimentally. (A) Overview. The conduit is imaged on a microscope as medium + red fluorescent beads flow through it. **(B)** Conduit cross-section. Most beads travel down the conduit, but a few are stuck on the bottom or the ceiling. h_{max} is calculated after measuring z (the distance of a bead stuck on the ceiling to the axial centre-line in the crosshair) and h_z, using the geometry of a segment of a circle. **(C)** Images of beads after focussing on the bottom **(i)** and **(ii)** top of the conduit. Stuck and stationary beads appear as dots, and moving ones as blurs ('streamlines') due to the long exposure.

Semi-analytical model to describe fluid-walled conduits

Our initial aim is to model a straight conduit with known flow rates provided by a syringe pump (Fig. 1C). We first consider the standard solution for flow between parallel plates derived from the momentum equation (Supplementary Information gives full derivations for this and other equations). The resultant pressure gradient is $\frac{dP}{dx} = \frac{8\mu u_{max}}{h_{max}^2}$ (μ = viscosity, u_{max} = maximum velocity). As the cross-section of fluid-walled conduits can be represented by the segment of a circle where height is expressed locally as $h_z = \sqrt{R^2 - z^2} - b$ (see Fig. 1Ciii and Fig. 2B for schematics of the conduit cross-section), the flow rate (Q) becomes ($Q = uA$; u = velocity, A = cross-sectional area):

$$Q = \frac{4}{3}\int_0^a \frac{h_z^3 u_{max}}{h_{max}^2}\,dz = \frac{4}{3}\frac{u_{max}}{h_{max}^2}\int_0^a \left(\sqrt{R^2 - z^2} - b\right)^3 dz \qquad (1)$$

The integrand is rearranged and nondimensionalized using $\eta = \frac{z}{a}$, and evaluated for the condition $a \gg h_{max}$ (defined as $\frac{h_{max}}{a} \leq 0.2$, Fig. S5) which – critically for the following solution – yields an approximately constant value for the integral to give $Q = 0.61\, u_{max}\, a\, h_{max}$. Substituting this into the pressure gradient for flow between two parallel

plates, we obtain $\frac{dP}{dx} = \frac{13.04\mu Q}{a\, h_{max}^3}$. For $a \gg h_{max}$, $R = \frac{a^2}{2h}$, which combined with $\Delta P_{conduit} = \frac{\gamma}{R}$, yields the semi-analytical expression for conduit height $h_{max}(x) = \left(\frac{26.08Q\mu ax}{\gamma} + h_0^4\right)^{0.25}$ (h_0 is the maximum height at the exit where $x = 0$). For a conduit height-to-width ratio $\frac{h_{max}}{a} = 0.2$ (within our operational range), the associated error is ~4%, which carries through from our simplification of the radius of curvature of a conduit from $a \gg h_{max}$.

This solution enables height at any position in a conduit to be predicted if the boundary condition h_0 is known. Evaluating the magnitude of the bracketed term $\frac{26.08Q\mu ax}{\gamma h_0^4}$, we find that for a conduit with $a = 400$ µm, $\mu = 1$ cP, $Q = 25$ µL/h, $\gamma = 0.04$ N/m, and $h_0 = 20$ µm (as an order of magnitude reference), the effect of the boundary condition on height more than 1 mm away from the exit is small. This provides a favourable corollary; height can be predicted by the simplified power law:

$$h_{max}(x) = \left(\frac{26.08Q\mu ax}{\gamma}\right)^{0.25} \quad (2)$$

Hence, we do not require h_0 to be known to predict conduit height for most experimental conditions of interest.

The semi-analytical solution predicts experimentally-measured heights

We next measure heights of conduits made with DMEM + 10% FBS (from the exit to 25 mm upstream) using the approach outlined in Figure 2, and compare results with those predicted by Eq. 2, using $\gamma = 0.022$ N/m (obtained from pendant-drop tensiometry; see

Supplementary Information) and $\mu = 0.94$ cP (at 25°C; [26]). In all cases, predicted results fit experimental data well – for example, as flow and conduit width vary (6.25 µL/h $\leq Q \leq$ 100 µL/h in Fig. 3i, and ~750-1175 µm in Fig. 3ii). Good fits are also obtained with conduits printed and perfused with medium plus 20% SR, and in conduits printed with medium plus 10% FBS and then perfused with water (Fig. 3iii); this suggests that components in FBS and SR are deposited on conduit walls and ceilings during conduit construction to create long-lived no-slip boundaries. Therefore, we examine the stability of the boundary with and without continuous flow for 24 h before measuring heights (with flow). Although the variance of height over time is small between experiments (Fig. S8), the dynamic nature of interfacial tension could be expected to introduce a time-dependent variable to explain the small differences measured. We also show that measured heights match predictions as they map onto a single reference plot (Fig. 3iv; Eq. S42). Finally, we compare predictions obtained from the semi-analytical solution with those from a numerical model that does not require the h/a simplification implicit in our power law; there is excellent agreement at scales relevant to this study (Fig. S6; Supplementary Information).

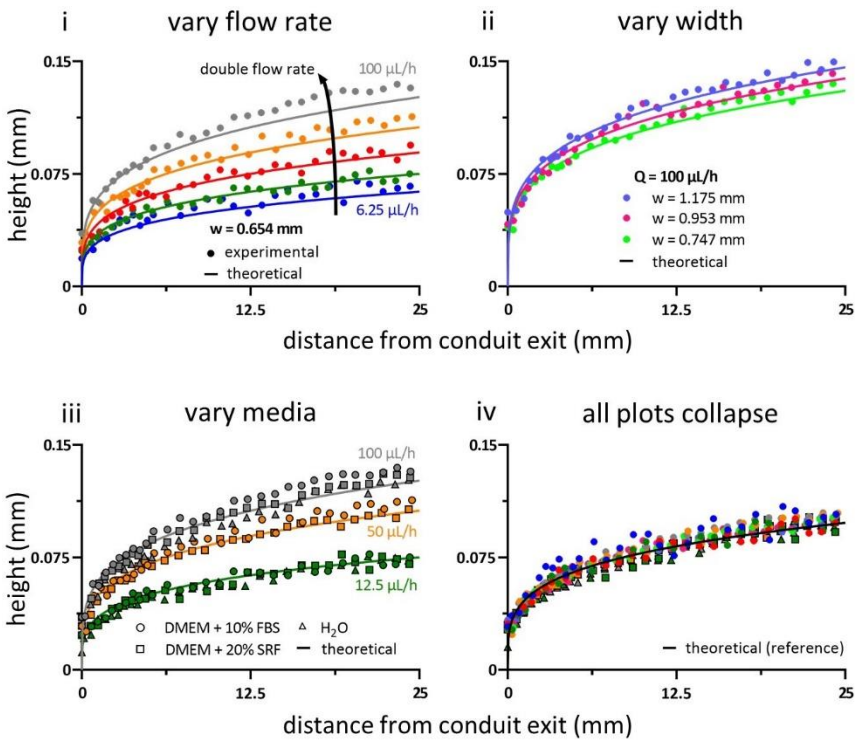


Fig. 3. Effects of varying conditions on maximum conduit height. Individual points: h_{max} measured as in Fig. 2 over conduit length (25 mm). Continuous lines: theoretical predictions based on Eq. 2 (in iv, using $Q = 25$ µL/h and $w = 953$ µm). 1 experimental repeat for each condition. **(i)** Varying flow rate (conduit width ~650 µm). **(ii)** Varying conduit width (flow rate 100 µL/h). **(iii)** Varying media flowing through conduit (width ~650 µm). Conduits were either prepared using DMEM + 10% FBS and perfused with the same medium (circular points), H_2O (triangular points), or prepared and perfused using DMEM + 20% SR (square points). Heights at each flow rate are almost identical to DMEM + 10% FBS. **(iv)** Height measurements of all conduits are collapsed onto a single reference plot according to Eq. S38 (colour codes as in i and ii), demonstrating that Eq. 2 predicts conduit heights for varying conditions.

Predicting wall shear stress

Wall shear stress, τ_{max}, is evaluated at $y = \pm\frac{h}{2}$, with $\tau_{max} = \mu\frac{\partial u}{\partial y}$ and $\frac{\partial u}{\partial y} = \frac{8yu_{max}}{h_{max}^2}$. We then use the relationship $u_{max(z)} = \frac{u_{max(0)}}{h_{max}^2}h_z^2$ to infer $\tau_{max(z)} = \tau_{max(0)}\frac{h_z}{h_{max}}$. τ_{max} is then expressed in terms of h_{max} using Eq. 2 to yield:

$$\tau_{max(z)} = 1.28\sqrt{\frac{\mu\gamma Q}{a^3 x}}\frac{h_z}{h_{max}} \tag{3}$$

Chokes reduce height variations down conduits

Controlling shear stress is essential for many cell studies; this is easily achieved in solid-walled systems with fixed geometries [12]. In our conduits, height increases from the exit as one progresses further upstream, and this translates into corresponding variations in shear stress. Additionally, $\frac{dh}{dx}$ progressively decreases as distance from the exit increases (from Eq. 2, $h \propto x^{0.25}$, and so $\frac{dh}{dx} \propto x^{-0.75}$). Consequently, approximately-uniform fields of wall shear stress ($\frac{d\tau}{dx}$) are only found tens of centimetres from the exit, so conduits with the relatively uniform fields required by biologists cannot be built in a 6 cm dish. Therefore, we add a short narrow conduit (a choke) to the exit of the conduit, so the choke bears most of the pressure drop and creates a field of nearly uniform shear throughout the conduit (Fig. 4Ai). Due to the choke, $h_{conduit} \propto \left(\frac{a_{conduit}}{a_{choke}}\right)^2$; then, the effective length (x_{eff}) introduced by the choke, at which $h = h_{conduit}$ for a conduit without a choke, is: $x_{eff} = x_{choke}\left(\frac{a_{conduit}}{a_{choke}}\right)^7$. From Eq. 3, $\left(\frac{d\tau}{dx}\right)_{no\ choke} \propto \left(\frac{1}{ax}\right)^{\frac{3}{2}}_{conduit}$, so $\left(\frac{d\tau}{dx}\right)_{choke} \propto \left(\frac{1}{a_{conduit}x_{eff}}\right)^{\frac{3}{2}}$. Hence, the change in

$\frac{d\tau}{dx}$ from the addition of a choke is $\frac{\left(\frac{d\tau}{dx}\right)_{no\ choke}}{\left(\frac{d\tau}{dx}\right)_{choke}} \propto \left(\frac{a_{conduit}}{a_{choke}}\right)^{\frac{21}{2}}$. Therefore, for conduits in Fig. 4B, the change in τ over 1 cm upstream of the choke is marginal (in order of increasing choke length, values are 0.85%, 0.20%, and 0.15% respectively), and wall shear stress is effectively constant in the flow direction.

To illustrate the effect of a choke on conduit height, we print a conduit with 10 connected drops (Fig. 4Aii). During flow, the pressure in each drop matches the local pressure in the conduit at the connection point; therefore, each drop serves as an independent pressure sensor. Without a choke, drop height decreases in the direction of flow as the pressure falls (Fig. 4Aiii). With a choke, all sensors have approximately similar heights (Fig. 4Aiv). Wall shear stresses calculated from Eq.3 also show that choked conduits have more constant fields along their lengths that are up to 2 orders of magnitude smaller than choke-free ones (Fig. 4D). Predicted velocity and shear-stress fields across conduit width are shown in Fig. 4D, inset. Strikingly, 25% of the width experiences less than 5% variation in shear stress (yellow region in inset). Human umbilical vein endothelial cells (HUVECs) – chosen because they are known to respond to shear stress – also grow as expected [5] in such a choked conduit and do not realign (as realignment typically occurs for shear stresses higher than 0.2 Pa [27]) (Fig. S12).

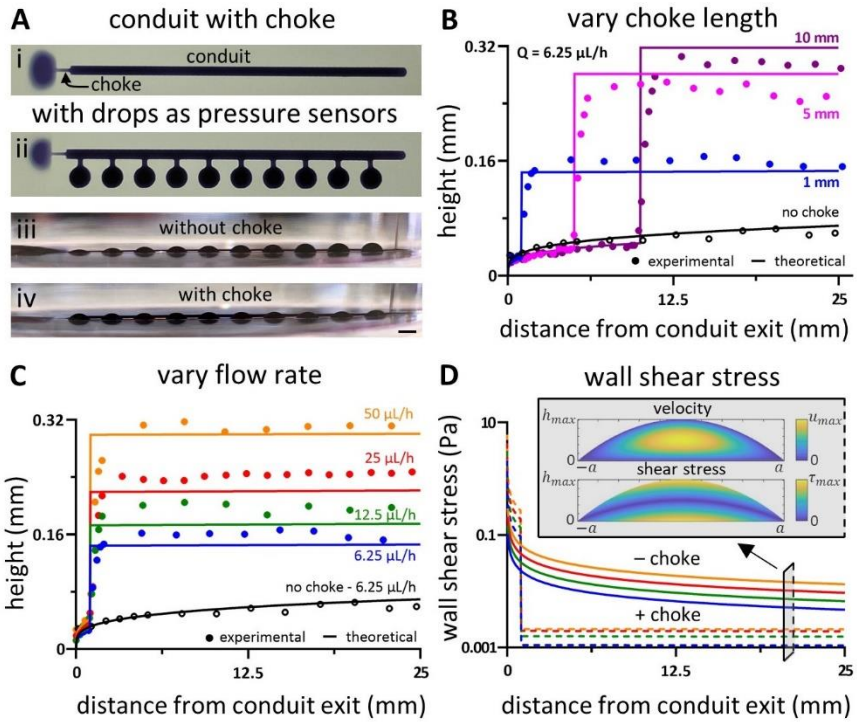


Fig. 4. Chokes suppress variations of h_{max} and shear stress along conduits. Generally, conduits (width ~950 µm) are connected to exit chokes (width ~400 µm). Lines in graphs show theoretical results from Eq. 2. **(A)** Images. Blue dye added to aid visualisation of flow to the left. Bar: 2 mm. **(i)** Top view of conduit (length 24 mm) with choke (length 1 mm). **(ii)** Top view of a conduit + choke (as i) with attached pressure sensors/drops. **(iii, iv)** Side views of a conduit (length 25 mm) + sensors, and conduit (length 24 mm) + sensors plus choke (1 mm). Sensor-drop height reflects the local pressure in the main conduit. Without a choke, drop height decreases in the direction of flow with distance from exit; with a choke, heights (and so pressures) remain more uniform down the conduit. **(B)** Varying choke length (1, 5 and 10 mm; as choke length increases, conduit length falls so all structures are 25 mm long). 1 experimental repeat for each condition. **(C)** Height variations are stabilized at different levels at different flow rates (conduit length 24 mm, choke length 1 mm). 1 experimental repeat for each condition. **(D)** Shear stress (calculated semi-analytically from Eq. 3) along the mid-line of conduits ± chokes (conduit length 24 mm, choke length 1 mm). Line colours reflect those in panel (C). Solid lines – without choke; dashed lines – with choke. Chokes ensure shear stress is more uniform down the conduit. Inset: normalised velocity and shear stress profiles applying to any flow rates across the circular cross-section of any conduit ± choke (see Supplementary Information).

Predicting flows in complex networks

This theory for single conduits can be extended to networks where conduits split or merge (as in vascular trees). We begin with a network in which input (parent) and output (daughter) conduits have the same width. Output flow (Q_d) is determined by continuity, so for one input (flow rate Q_p) splitting into n outputs, $Q_d = \frac{Q_p}{n}$. If instead, m inputs (with the same Q_p) merge into a single output, then $Q_d = m \times Q_p$. This process can be repeated to determine flows emerging from each node in a complex tree. The semi-analytical solution is then applied iteratively through each conduit starting from the exit.

We first study one conduit splitting into two daughters (Fig. 5A), then the same structure with reversed flow (Fig. 5B), and finally a bifurcating tree with four generations of daughters (Fig. 5C). All parents and daughters have the same widths, but the flow area at the junction increases so the local pressure drop is small and assumed to be negligible. Theoretical predictions fit well with experimental height measurements (Fig. 5). This theory may also be extended to networks in which conduits have different lengths and widths (Supplementary Information).

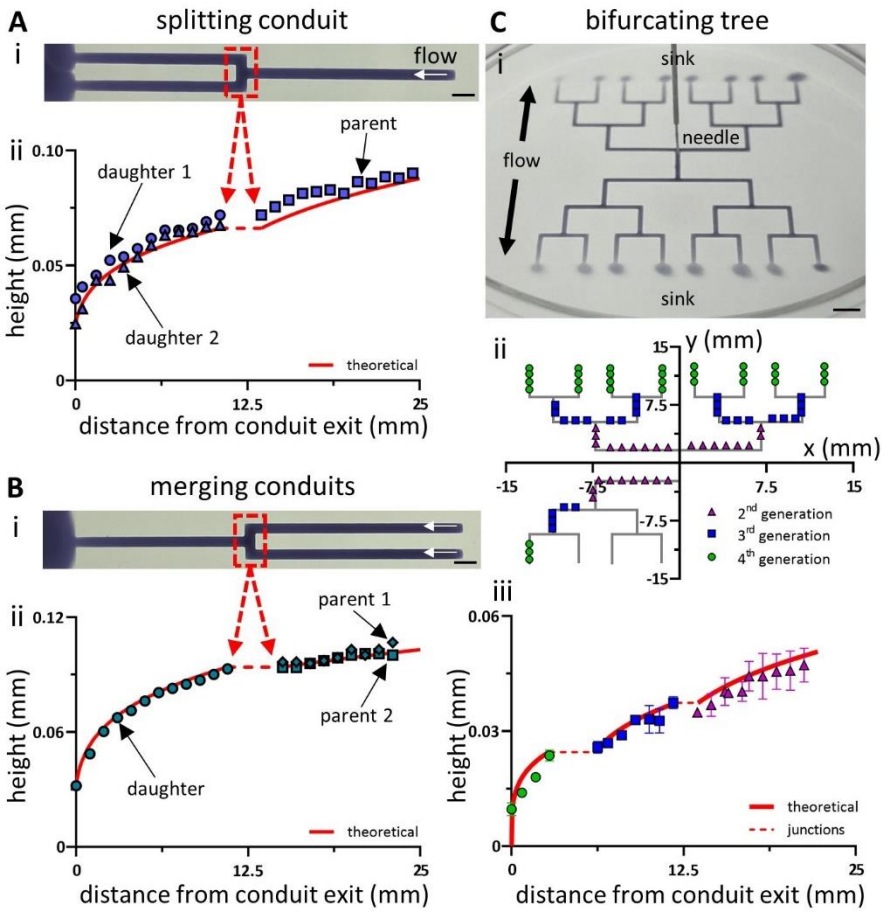


Fig. 5. Splitting, merging and bifurcating circuits. Conduit heights are measured as in Fig. 2. Red line in plots: theoretical height predictions from Eq. 2 (dashed portions correspond to junctions and assume no local pressure drop). Bars in images: 2 mm. 1 experimental repeat for each condition. **(A)** Splitting conduit. **(i)** Image (conduit width ~650 µm). **(ii)** Heights down parent and daughters (input into parent 25 µL/h). **(B)** Merging conduits. **(i)** Image (conduit width ~650 µm). **(ii)** Heights down conduits (both parents perfused at 25 µL/h). **(C)** Bifurcating tree. **(i)** Image (6 cm dish; conduit width ~550 µm). **(ii)** Tree plan (grey line) showing where heights are measured (coloured symbols indicate daughter generation). **(iii)** Plot indicating concordance between measured (symbols coloured as in Cii) and predicted heights.

Discussion

Our challenge was to predict flow through a straight fluid-walled conduit built using cell-culture media on a standard 6 cm Petri dish; during flow, the cross-section of such a conduit inevitably morphs above an unchanging footprint (i.e., it expands as flow increases, and shrinks with distance from input; Fig. 1C). Our approach is based on the recognition that conduit height reflects local pressure. Therefore, we developed a method to measure height (Fig. 2), and found that addition of FBS or SR to media creates a solid media:FC40 interface that induces the no-slip boundary condition which defines the boundary condition for our model (Fig. 2). Therefore, it is likely that fluids rich in albumin (e.g., in the vasculature, lymph, cerebrospinal fluid, and vitreous humor), will yield the same no-slip condition. We next establish a simple power law with a fixed exponent (Eq. 2) by approximating conduit cross-section and applying the no-slip boundary condition. This power-law enables prediction of conduit height, flow field, and shear stress (Eq. 3) anywhere in a conduit; it requires no additional boundary conditions beyond conduit footprint, flow rate, viscosity of medium, and interfacial tension. This level of information is essentially similar to that required with laminar flow through a solid-walled pipe, except pipe diameter now morphs in the flow direction to enable the pressure gradient induced by interfacial tension to satisfy the momentum equation. This law also agrees with numerical predictions for conduits satisfying $h/a \leq$ ~0.2, which is in the practical range. It enables users to design conduits and predict a priori flows and shear stresses matching their specific requirements, including ones with essentially uniform shear-stress profiles by adding chokes (in the absence of chokes such conduits would be too long to fit in a 6 cm dish). Moreover, the shear stresses generated in our system are typically below in vivo values for endothelial cells (0.2 Pa [27]), and thus do not cause cell realignment (Fig. S12). We also experimentally demonstrate the interplay between conduit

height and pressure by printing 10 drops connected at different points down a conduit; then, during flow, each drop serves as an independent pressure sensor (as height reflects local pressure; Fig. 4A). We also verify experimentally the accuracy of the model by varying flows through conduits with a range of widths (Fig. 3), as well as splitting and merging conduits (Fig. 5A,B) and a fractal vascular tree (Fig. 5C). As this form of open microfluidics offers multiple advantages over traditional closed systems [20]–[22], we anticipate this model will increase uptake of these circuits in domains benefiting from flow (e.g., when generating chemotactic gradients using laminar streams) and well-defined shear stress (e.g., when studying thromboses in vascular trees).

Materials and Methods

Fluid-walled microfluidic circuit fabrication

All circuits were fabricated using a custom-made programmable printer (iotaSciences Ltd, Oxford, UK). The printer is fitted with a syringe pump that drives a 1 mL glass syringe (Hamilton, Reno, Nevada, USA). The syringe is filled with the immiscible and bioinert fluorocarbon FC40 (FC40STAR®, iotaSciences Ltd, Oxford, UK) and connected via polytetrafluoroethylene (PTFE) tubing (26G, Adhesive Dispensing Ltd, Milton Keynes, UK) to a laser-cut jetting needle (25G, 70 µm inner diameter, Oxford Lasers, Didcot, UK) held by the printer's 3-axis traverse.

Circuits were made on 60 mm tissue culture-treated dishes (Corning, 430166). First, 1 mL of cell culture media is pipetted on the dish and swirled until it covers the entire bottom of the dish. Media was either DMEM (Merck) + 10% FBS (Merck) or DMEM + 20% SR (ThermoFisher). The dish is then tilted so excess media drains to the side, and most media removed by pipetting to leave a thin residual film (~30 µm thick) on the bottom. This film is now overlaid with 2 mL FC40 (Fig. 1A), the dish placed on the stage of the printer, and the jetting needle lowered until the tip is 0.5 mm above the bottom of the dish. FC40 is now jetted (8 µL/s) as the needle moves laterally above the surface of the dish. As the submerged FC40 jet contacts the dish's surface, it pushes media aside to leave fluid walls of FC40 pinned to the dish by interfacial forces. These walls then shape the conduit.

Perfusing fluid-walled conduits

A 250 µL glass syringe (Hamilton) filled with medium and placed in a syringe pump (PhD Ultra, Harvard Apparatus) is connected via PTFE tubing to a 25G stainless-steel hollow

needle (Adhesive Dispensing Ltd). The needle is lowered through the ceiling into the conduit ~30 mm from the exit until it is ~100 µm above the bottom of the dish, and the dish placed on the stage of an inverted microscope. The syringe pump is then started, and conduit heights measured once pressures in conduits reach equilibrium after ~30 min. Open-ended straight conduits are 25 mm long, unless stated otherwise.

Measuring conduit height

Conduits in Figures 3 and 4 were imaged on a Zeiss Axio Observer inverted microscope with a 10X Plan Apochromat Air objective (NA = 0.3), and in Figures 5 and S8 on an Olympus IX53 inverted microscope with a 40X objective (NA = 0.55). Conduit heights were measured as conduits were perfused with media plus red fluorescent beads (1:1000 mixture; 0.5 µm diameter; FluoSpheres, F8812, ThermoFisher). After equilibration for ~30 min after perfusion begins, some beads remain stationary on the surface of the dish or the media:FC40 interface and are used for height measurements (Fig. 2). To validate the theoretical model, we measure h_{max} experimentally and correct heights for apparent depth due to refraction (Eq. S40).

The Zeiss microscope has a motorised stage and a digital controller that can record coordinates to within tens of nm. It displays real-time images on a monitor, with a cross-hair indicating the exact position (Fig. 2C). Starting from the conduit exit, this digital controller is used to position the objective close to the center of the conduit, a static bead on the media:FC40 ceiling is brought into focus, coordinates recorded, the stage lowered to focus on a static bead on the dish surface (there are typically many), and coordinates again recorded. The stage is then moved laterally to record the edge coordinates of the conduit. The offset z between the bead on the ceiling and the centre of the conduit, and the corresponding height

at this point, h_z, are now calculated. h_{max} is then inferred using trigonometry, and measurements repeated along the length of the conduit. In the first 5 mm (where conduit height increases most rapidly), measurements are taken every 0.5 mm, and in the remaining 20 mm steps are increased to 1 mm. The stage of the Olympus microscope lacks digital control and is less precise, and the approximate location of the centre of the conduit is determined using the circular nature of the fluid interface; moving the objective upwards scans through beads stuck on the interface, which get closer to the top of the conduit as the objective is raised. The top is identified when only one or a few beads remain in focus (typically in an axial strip), and this position is recorded using the scale on the objective knob of the microscope (ticks spaced in 1 μm increments). The position on the surface of the dish directly below this bead is also recorded, and the difference gives h_{max}. This process is then repeated along the entire conduit as before. Pictures of the conduit are then taken with a 4X objective to obtain its average width.

Due to mismatches between the refractive indices of culture media and air, height differences measured on microscopes using the focal position of beads do not reflect axial movement of the microscope objective; rather, they appear smaller [28]. Height corrections are dependent on objective numerical aperture and refractive indices, which for our experiments was found to be $\Delta f = \alpha \times \Delta s$, where Δf is the actual conduit height, Δs is the measured height, and α is a constant ($\alpha = 1.36$ for Zeiss measurements; $\alpha = 1.45$ for Olympus measurements).

References

[1] D. Huber, A. Oskooei, X. Casadevall i Solvas, A. deMello, and G. V Kaigala, “Hydrodynamics in Cell Studies,” *Chem. Rev.*, vol. 118, no. 4, pp. 2042–2079, Feb. 2018, doi: 10.1021/acs.chemrev.7b00317.

[2] R. Novak *et al.*, “Robotic fluidic coupling and interrogation of multiple vascularized organ chips,” *Nat. Biomed. Eng.*, vol. 4, no. 4, pp. 407–420, 2020, doi: 10.1038/s41551-019-0497-x.

[3] S. E. Park, A. Georgescu, and D. Huh, “Organoids-on-a-chip,” *Science (80-.).*, vol. 364, no. 6444, pp. 960 LP – 965, Jun. 2019, doi: 10.1126/science.aaw7894.

[4] D. Tuveson and H. Clevers, “Cancer modeling meets human organoid technology,” *Science (80-.).*, vol. 364, no. 6444, pp. 952 LP – 955, Jun. 2019, doi: 10.1126/science.aaw6985.

[5] J. Shemesh, I. Jalilian, A. Shi, G. Heng Yeoh, M. L. Knothe Tate, and M. Ebrahimi Warkiani, “Flow-induced stress on adherent cells in microfluidic devices,” *Lab Chip*, vol. 15, no. 21, pp. 4114–4127, 2015, doi: 10.1039/C5LC00633C.

[6] H. A. Stone, A. D. Stroock, and A. Ajdari, “Engineering Flows in Small Devices: Microfluidics Toward a Lab-on-a-Chip,” *Annu. Rev. Fluid Mech.*, vol. 36, no. 1, pp. 381–411, Jan. 2004, doi: 10.1146/annurev.fluid.36.050802.122124.

[7] S. Blonski, D. Zaremba, M. Jachimek, S. Jakiela, T. Wacławczyk, and P. M. Korczyk, “Impact of inertia and channel angles on flow distribution in microfluidic junctions,” *Microfluid. Nanofluidics*, vol. 24, no. 2, p. 14, 2020, doi: 10.1007/s10404-020-2319-6.

[8] A. Raj, P. P. A. Suthanthiraraj, and A. K. Sen, “Pressure-driven flow through PDMS-based flexible microchannels and their applications in microfluidics,” *Microfluid. Nanofluidics*, vol. 22, no. 11, p. 128, 2018, doi: 10.1007/s10404-018-2150-5.

[9] M. Bahrami, M. M. Yovanovich, and J. R. Culham, “Pressure Drop of Fully-Developed, Laminar Flow in Microchannels of Arbitrary Cross-Section,” *J. Fluids Eng.*, vol. 128, no. 5, pp. 1036–1044, Jan. 2006, doi: 10.1115/1.2234786.

[10] E. Kaliviotis, J. M. Sherwood, and S. Balabani, “Local viscosity distribution in bifurcating

microfluidic blood flows," *Phys. Fluids*, vol. 30, no. 3, p. 30706, Feb. 2018, doi: 10.1063/1.5011373.

[11] X. Lu, M. M. Galarneau, J. M. Higgins, and D. K. Wood, "A microfluidic platform to study the effects of vascular architecture and oxygen gradients on sickle blood flow," *Microcirculation*, vol. 24, no. 5, p. 10.1111/micc.12357, Jul. 2017, doi: 10.1111/micc.12357.

[12] K. Zografos, R. W. Barber, D. R. Emerson, and M. S. N. Oliveira, "A design rule for constant depth microfluidic networks for power-law fluids," *Microfluid. Nanofluidics*, vol. 19, no. 3, pp. 737–749, 2015, doi: 10.1007/s10404-015-1598-9.

[13] E. Marušić-Paloka, "Fluid flow through a network of thin pipes," *Comptes Rendus l'Académie des Sci. - Ser. IIB - Mech.*, vol. 329, no. 2, pp. 103–108, 2001, doi: https://doi.org/10.1016/S1620-7742(00)01296-4.

[14] J. Berthier, K. Brakke, and E. Berthier, *Open Microfluidics*. Wiley, 2016.

[15] J. Berthier, A. B. Theberge, and E. Berthier, "Open-Channel Microfluidics," *Fundamentals and applications*. Morgan & Claypool Publishers, 2019, doi: 10.1088/2053-2571/ab21ca.

[16] C. Li *et al.*, "Under oil open-channel microfluidics empowered by exclusive liquid repellency," *Sci. Adv.*, vol. 6, no. 16, p. eaay9919, Apr. 2020, doi: 10.1126/sciadv.aay9919.

[17] G. D. Towell and L. B. Rothfeld, "Hydrodynamics of rivulet flow," *AIChE J.*, vol. 12, no. 5, pp. 972–980, Sep. 1966, doi: https://doi.org/10.1002/aic.690120524.

[18] S. Qian, S. W. Joo, Y. Jiang, and M. A. Cheney, "Free-surface problems in electrokinetic micro- and nanofluidics," *Mech. Res. Commun.*, vol. 36, no. 1, pp. 82–91, 2009, doi: https://doi.org/10.1016/j.mechrescom.2008.06.014.

[19] H. B. van Lengerich, M. J. Vogel, and P. H. Steen, "Coarsening of capillary drops coupled by conduit networks," *Phys. Rev. E*, vol. 82, no. 6, p. 66312, Dec. 2010, doi: 10.1103/PhysRevE.82.066312.

[20] C. Soitu, N. Stovall-Kurtz, C. Deroy, A. A. Castrejón-Pita, P. R. Cook, and E. J. Walsh, "Jet-Printing Microfluidic Devices on Demand," *Adv. Sci.*, 2020, doi: 10.1002/advs.202001854.

[21] C. Soitu *et al.*, “Microfluidic chambers using fluid walls for cell biology,” *Proc. Natl. Acad. Sci.*, 2018, doi: 10.1073/pnas.1805449115.

[22] E. J. Walsh *et al.*, “Microfluidics with fluid walls,” *Nat. Commun.*, vol. 8, no. 1, p. 816, 2017, doi: 10.1038/s41467-017-00846-4.

[23] S. N. Calver, E. A. Gaffney, E. J. Walsh, W. M. Durham, and J. M. Oliver, “On the thin-film asymptotics of surface tension driven microfluidics,” *J. Fluid Mech.*, vol. 901, p. A6, 2020, doi: DOI: 10.1017/jfm.2020.532.

[24] I. Giaever and C. R. Keese, “Behavior of cells at fluid interfaces.,” *Proc. Natl. Acad. Sci. U. S. A.*, vol. 80, no. 1, pp. 219–222, Jan. 1983, doi: 10.1073/pnas.80.1.219.

[25] C. R. Keese and I. Giaever, “Cell growth on liquid interfaces: Role of surface active compounds,” *Proc. Natl. Acad. Sci. U. S. A.*, vol. 80, no. 18, pp. 5622–5626, Sep. 1983, doi: 10.1073/pnas.80.18.5622.

[26] E. Fröhlich *et al.*, “Comparison of two in vitro systems to assess cellular effects of nanoparticles-containing aerosols,” *Toxicol. In Vitro*, vol. 27, no. 1, pp. 409–417, Feb. 2013, doi: 10.1016/j.tiv.2012.08.008.

[27] S. Zhao *et al.*, “Synergistic Effects of Fluid Shear Stress and Cyclic Circumferential Stretch on Vascular Endothelial Cell Morphology and Cytoskeleton,” *Arterioscler. Thromb. Vasc. Biol.*, vol. 15, no. 10, pp. 1781–1786, Oct. 1995, doi: 10.1161/01.ATV.15.10.1781.

[28] T. D. Visser, J. L. Oud, and G. J. Brakenhoff, “Refractive index and axial distance measurements in 3-D microscopy,” *Optik (Stuttg).*, vol. 90, no. 1, pp. 17–19, 1992.

Supplementary Information

List of symbols

$x = x$ *coordinate*
$y = y$ *coordinate*
$z = z$ *coordinate*
$u = x$ *component of velocity*
$v = y$ *component of velocity*
$Q =$ *flow rate*
$P =$ *pressure*
$\rho =$ *fluid density*
$\mu =$ *fluid viscosity*
$\gamma =$ *interfacial tension*
$\theta =$ *contact angle*
$h_{max} =$ *maximum conduit height (at the centreline)*
$h_0 =$ *conduit exit height*
$h_z =$ *conduit height a distance z from the centreline*
$a =$ *conduit half-width*
$R =$ *radius of curvature*
$b = R - h_{max}$
$u_{max(0)} =$ *maximum flow velocity along conduit centreline*
$u_{max(z)} =$ *maximum flow velocity a distance z from the centreline*
$\tau =$ *shear stress*
$\tau_{max(0)} =$ *maximum shear stress along conduit centreline*
$\tau_{max(z)} =$ *maximum shear stress a distance z from the centreline*

Semi-analytical solution for fluid-walled conduits

The solution to flow through fluid-walled conduits is derived from the simplified Navier-Stokes equation:

$$\rho\left(u\frac{\partial u}{\partial x} + v\frac{\partial u}{\partial y}\right) = -\frac{\partial P}{\partial x} + \mu\left(\frac{\partial^2 u}{\partial x^2} + \frac{\partial^2 u}{\partial y^2}\right) \qquad (S1)$$

Flow is laminar (the Reynolds number of our conduits never exceeds 0.1; Table S1), unidirectional ($v = 0$), and fully-developed ($\frac{\partial u}{\partial x} = \frac{\partial^2 u}{\partial x^2} = 0$). The simplified equation becomes:

$$\frac{\partial P}{\partial x} = \mu \frac{\partial^2 u}{\partial y^2} \qquad (S2)$$

From Fig. 1C, we determine these geometrical relationships:

$$a^2 + b^2 = R^2$$

$$R = b + h_{max}$$

$$R = \frac{a^2 + h_{max}^2}{2h_{max}} \qquad b = \frac{a^2 - h_{max}^2}{2h_{max}}$$

Conduit height, h_z, at any location across the half width (Fig. 2B) is:

$$h_z = \sqrt{R^2 - z^2} - b \qquad (S3)$$

At the centre of the conduit ($z = 0$), height is maximal and corresponds to h_{max}; at pinning lines ($z = \pm a$), it is 0. The width and length of the conduit are set by the user and do not change over time. However, h_{max} depends on the pressure which changes during flow as fluid walls morph; it increases with increasing pressure, and decreases in the direction of flow. From the provided boundary conditions, the dimensionless velocity profile is assumed to be the same as that used in the classical solution of Poiseuille flow between parallel plates, and – as media:FC40 interfaces act as solid boundaries – we assume the no-slip boundary condition applies:

$$@y = \pm\frac{h_{max}}{2}; u = 0 \quad and \quad @y = 0; \frac{du}{dy} = 0$$

Integrating Eq. S2 twice yields:

$$\frac{du}{dy} = \frac{1}{\mu}\frac{dP}{dx}y + c_1, \qquad u(y) = \frac{1}{2\mu}\frac{dP}{dx}y^2 + c_1 y + c_2$$

Applying boundary conditions, we find:

$$c_1 = 0; \quad c_2 = -\frac{1}{8\mu}\frac{dP}{dx}h_{max}^2$$

And so $u(y)$ can be expressed as:

$$u(y) = \frac{1}{2\mu}\frac{dP}{dx}\left(y^2 - \frac{h_{max}^2}{4}\right) \tag{S4}$$

Since $u(y) = u_{max}$ @ $y = 0$, the flow's maximum velocity becomes:

$$u_{max} = -\frac{h_{max}^2}{8\mu}\frac{dP}{dx} \tag{S5}$$

$$\therefore u(y) = \left(1 - \frac{4y^2}{h_{max}^2}\right)u_{max}, \qquad \frac{dP}{dx} \propto \frac{u_{max}}{h_{max}^2}$$

Across the conduit's width (in the z-direction), $\frac{dP}{dx}$ = constant; hence, the relationship between the maximum flow velocity across a width, $u_{max(z)}$, to the maximum conduit velocity, $u_{max(0)}$, is:

$$\frac{u_{max(0)}}{h_{max}^2} = \frac{u_{max(z)}}{h_z^2}$$

$$u_{max(z)} = \frac{u_{max(0)}}{h_{max}^2} h_z^2 \qquad (S6)$$

The total flow rate through the conduit is found by integrating the velocity profile:

$$Q = \int_{-a}^{a} \int_{-\frac{h_z}{2}}^{\frac{h_z}{2}} u(y) dy dz$$

Evaluating the first integral provides flow rate per unit length as:

$$Q' = \int_{-\frac{h_z}{2}}^{\frac{h_z}{2}} u(y) dy = -\frac{h_z^3}{12\mu} \frac{dP}{dx} = \frac{2}{3} u_{max(z)} h_z$$

$$\therefore Q = \int_{-a}^{a} \frac{2}{3} u_{max(z)} h_z dz \qquad (S7)$$

Substituting for u_z in Eq. S7 as in Eq. S6 yields:

$$Q = \frac{2}{3}\frac{u_{max(0)}}{h_{max}^2}\int_{-a}^{a} h_z^3 dz$$

And since from geometry $h_z = \sqrt{R^2 - z^2} - b$:

$$\therefore Q = \frac{4}{3}\frac{u_{max(0)}}{h_{max}^2}\int_{0}^{a}\left(\sqrt{R^2 - z^2} - b\right)^3 dz \qquad (S8)$$

The integrand is then normalised using $\eta = \frac{z}{a}$ and evaluated over $\frac{a}{h_{max}}$:

$$Q = \frac{4}{3}h_{max}u_{max(0)}a\int_{0}^{1}\frac{\left(\sqrt{R^2 - \eta^2 a^2} - b\right)^3}{h_{max}^3}d\eta \qquad (S9)$$

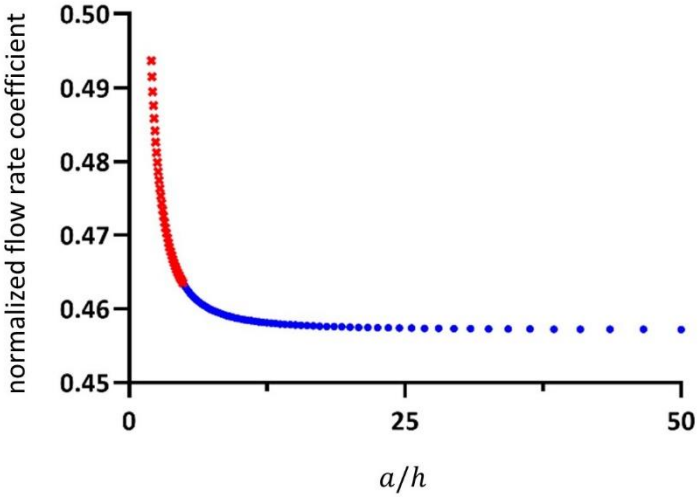


Fig. S1. Normalized volumetric flow rate coefficients for a range of conduit half width-to-height ratios.

The integrand in Eq. S9 is evaluated for $0 < a/h \leq 50$. Ratios less than 5 (red crosses, $a \sim h$) are ignored.

Ratios greater than 5 (blue dots, $a \gg h$) correspond to conduit geometries typically observed in this study. The average normalised flow rate coefficient in this region corresponds to 0.46.

For heights typically observed here ($a \gg h_{max}$; Fig S1), flow rate is:

$$Q = \frac{4}{3} h_{max} u_{max(0)} a(0.46)$$

$$\therefore u_{max(0)} = \frac{Q}{0.61 h_{max} a} \quad (S10)$$

Now substituting the relationship for $u_{max(0)}$ into Eq. S5 yields:

$$h_{max}^3 \frac{dP}{dx} = \frac{13.11 Q \mu}{a} \quad (S11)$$

The radius of curvature of the conduit is defined as $R = \frac{a^2 + h_{max}^2}{2h_{max}}$, however when $a \gg h_{max}$ the radius of curvature can be simplified as:

$$R = \frac{a^2}{2h_{max}} \left(1 + \frac{h_{max}^2}{a^2}\right) \approx \frac{a^2}{2h_{max}} \quad (S12)$$

Since change in hydrostatic pressure is assumed to be negligible along the conduit, the local pressure at any x-location can be characterized by the local Laplace pressure in accordance with the simplified Young-Laplace equation for interfaces represented as the arc of a circle

($\Delta P_{conduit} = \frac{\gamma}{R}$). Using the simplified cross-sectional radii of curvature expressed in Eq. S12 produces the following equation defining pressure increase across the interface:

$$\Delta P_{interface} = \frac{\gamma}{R} \approx \gamma \left(\frac{2h_{max}}{a^2}\right)$$

$$\therefore \frac{dP}{dx} = \frac{2\gamma}{a^2}\frac{dh}{dx} \tag{S13}$$

Substituting Eq. S13 into Eq. S11:

$$\frac{2\gamma}{a^2} h_{max}^3 dh = \frac{13.11 Q\mu}{a} dx \tag{S14}$$

$$\therefore h_{max}^3 dh = \frac{6.55 Q\mu a}{\gamma} dx \tag{S15}$$

Integrating Eq. S15 then gives:

$$h_{max}^4 = \frac{26.08 Q\mu a x}{\gamma} + c_1 \tag{S16}$$

Since at the exit, $h_{max} = h_0$, then $c_1 = h_0^4$. Hence the semi-analytical solution for predicting conduit centre-heights becomes:

$$h_{max}(x) = \left(\frac{26.08 Q\mu a x}{\gamma} + h_0^4\right)^{0.25} \tag{S17}$$

Reintroducing $P \approx \gamma\left(\frac{2h_{max}}{a^2}\right)$ into Eq. S17 solves for pressure as:

$$P_x = \left(\frac{417.28Q\mu\gamma^3 x}{a^7} + P_0^4\right)^{0.25} \quad (S18)$$

Importance of conduit exit-height

Eq. S17 requires an experimental measurement, conduit exit-height, h_0, to predict the height elsewhere in the conduit. However, consider the relative magnitude of the terms:

$$\frac{26.08Q\mu ax}{\gamma}, \qquad h_0^4$$

When $\frac{26.08Q\mu ax}{\gamma} \gg h_0^4$, exit height has a negligible effect on conduit height upstream. For given fluids, flow rate, and conduit width, the location along the conduit at which these two terms become equivalent is:

$$x = \frac{h_0^4\gamma}{26.08Q\mu a} \quad (S19)$$

For average flow rates and conduit widths used here ($Q = 25$ µL/h, $a = 0.5$ mm), $x \approx 92$ µm. At a conservative distance from the exit (i.e., an order of magnitude greater than x; 1 mm) height predictions converge across a range of exit heights (Fig. S2). Hence, a simplified semi-analytical solution requiring no experimental measurements can predict conduit height accurately away from the exit:

$$h_{max}(x) = \left(\frac{26.08Q\mu ax}{\gamma}\right)^{0.25} \qquad (S20)$$

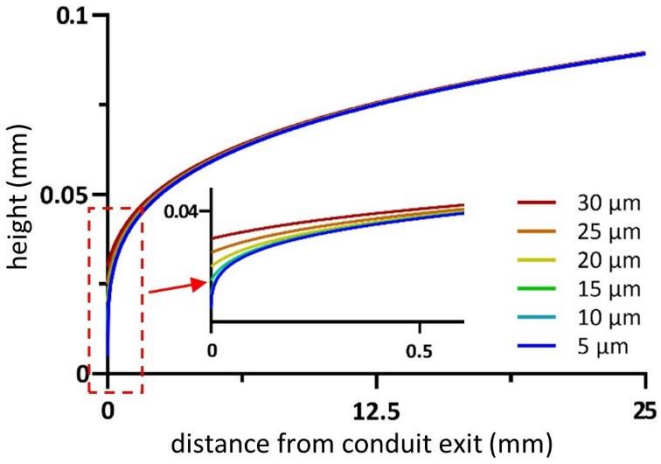


Fig. S2. The effect of exit height on conduit height is negligible. Conduit height (h_{max}) is calculated using Eq. S17 assuming exit heights (h_0) of 5 – 30 µm ($Q = 25$ µL/h, $a = 0.5$ mm). Inset: results for the first 0.6 mm. For low exit heights ($5 < h_0 < 20$), conduit heights differ markedly only in the first ~0.1 mm before converging; for larger exit heights ($h_0 = 25$ or 30 µm) convergence occurs later.

Numerical solution

The semi-analytical solution provides a simple powerful method to determine flows. However, it relies on geometrical assumptions (i.e., when deriving the normalised volumetric flow rate constant of Eq. S10, and $R = \frac{a^2}{2h}$). Therefore, we derived a numerical solution without these simplifications using the forward Euler method. Pressure along a conduit is solved iteratively in steps of Δx as:

$$P'(x) = \frac{P(x + \Delta x) - P(x)}{\Delta x}$$

$$\therefore P(x + \Delta x) = P(x) + \Delta x P'(x) \quad (S21)$$

From Eq. S8, volumetric flow rate is defined as:

$$Q = \frac{4}{3}\frac{u_{max}(x)}{h_{max}^2(x)}\int_0^a \left(\sqrt{R^2 - z^2} - b\right)^3 dz \quad (S22)$$

The integrand in Eq. S22 is a positive constant dependent only on local cross-section, represented by β:

$$Q = \frac{4}{3}\frac{u_{max}(x)}{h_{max}^2(x)}\beta(x) \quad (S23)$$

Rearranging for u_{max}:

$$u_{max}(x) = \frac{3}{4}\frac{h_{max}^2(x)}{\beta(x)}Q \quad (S24)$$

Given the initial value problem $P'(x) = \frac{8\mu u_{max}}{h_{max}^2}$ (Eq. S5), $P'(0) = \frac{8\mu u_0}{h_0^2}$, and $P(0) = \frac{\gamma}{R} = \frac{2\gamma h_0}{a^2 + h_0^2}$, Eq. S21 becomes:

$$P(\Delta x) = P(0) + \Delta x P'(0) \quad (S25)$$

$$P(\Delta x) = \frac{2\gamma h_0}{a^2 + h_0^2} + \frac{8\mu u_0}{h_0^2}\Delta x \qquad (S26)$$

From Eq. S24, $u_0 = \frac{3}{4}\frac{h_0^2}{\beta(0)}Q$, hence:

$$P(\Delta x) = \frac{2\gamma h_0}{a^2 + h_0^2} + \frac{6\mu Q}{\beta(0)}\Delta x \qquad (S27)$$

Rearranging the Young-Laplace equation yields the radius of curvature at Δx:

$$R(\Delta x) = \frac{\gamma}{P(\Delta x)} \qquad (S28)$$

This iteration is repeated for n steps ($n = \{1, \dots, L/\Delta x - 1\}$) along any conduit of length L, and is valid for as long as the half-width is greater than or equal to the local maximum height ($a > h_{max}$). If this height exceeds the half-width, the numerical solution fails (i.e., the conduit has a contact angle > 90°). It follows that:

$$R(n+1) = \frac{\gamma}{P(n+1)} \qquad (S29)$$

$$P(n+1) = P(n) + \frac{6\mu Q}{\beta(n)}\Delta x \qquad (S30)$$

$$P(n+1) = \frac{2\gamma h_{max}(n)}{a^2 + h_{max}^2(n)} + \frac{6\mu Q}{\beta(n)}\Delta x \qquad (S31)$$

Across geometries where $a \gg h_{max}$, there is good agreement between semi-analytical and numerical solutions (see later in Fig. S5).

Pendant-drop tensiometry

To determine the interfacial tension (IFT) between the various media used in this study and FC40, we used the First Ten Angstrom 1000B Manual Drop Shape Analyzer (Model B 23A 110) plus a Point Grey Firefly MV USB camera to record drops of FC40 formed in a cuvette of medium and infer the IFT through image analysis. To do so, a 34G needle (Adhesive Dispensing Ltd) is connected to a 50 µL glass syringe (Hamilton) via PTFE tubing. The syringe is filled with FC40 and loaded onto a syringe pump (Harvard Apparatus). The needle is then lowered inside a cuvette filled with medium. A drop of FC40 is then set by infusing a desired volume through the needle. A picture of the formed drop is taken, and the software determines the IFT. Drops were imaged for 5 h, and the IFT obtained by averaging values recorded 2.5 – 5 h after starting imaging, and then averaged again over the number of repeats (3 for each medium; Fig. S3). The values obtained are $\gamma_{FBS} = 22.8 \pm 0.44$ mN/m (DMEM + 10% FBS), $\gamma_{SR} = 22.2 \pm 0.99$ mN/m (DMEM + 20% SR), and $\gamma_{beads} = 20.7 \pm 0.58$ mN/m (DMEM + 10% FBS + beads). The system was also calibrated with water (a drop of water in a cuvette of FC40), yielding $\gamma_{H_20} = 51.8 \pm 0.74$ mN/m, which agrees with values accepted in the literature.

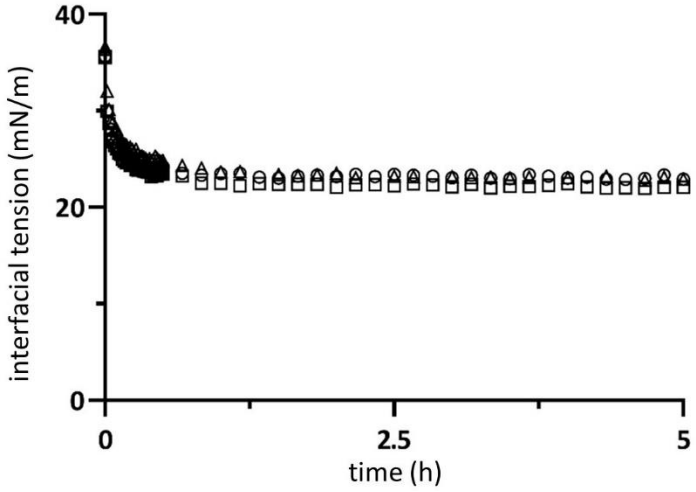


Fig. S3. Interfacial tension measurements between FC40 and DMEM + 10% FBS. Drops of FC40 were submerged in DMEM + 10% FBS, and the IFT measured over 5 h. Results of three repeats are shown, with each symbol corresponding to a repeat. In each repeat, IFT falls in the first 30 min to a plateau; the average value (γ_{FBS}) collected between 2.5 – 5 h was 22.8 ± 0.44 mN/m.

Reynolds number in fluid-walled conduits

Flow through conduits can be characterised by the Reynolds number, Re:

$$Re = \frac{\rho u_{avg} d_h}{\mu} \qquad (S32)$$

where d_h is the hydraulic diameter (often used as the characteristic length for flow through non-circular ducts or pipes in lieu of the traditional circular diameter). A duct's hydraulic diameter is:

$$d_h = \frac{4A}{P}$$

where A is cross sectional area and P is wetted perimeter. For fluidic conduits in this study, the hydraulic diameter is:

$$d_h = \frac{2\left(R^2\, sin^{-1}\left(\frac{a}{R}\right) - ab\right)}{R\, sin^{-1}\left(\frac{a}{R}\right) + a}$$

Table S1 gives Reynolds numbers calculated with Eq. S32 using experimental data from Fig. 3i:

Table S1. Reynolds number in fluid-walled conduits

flow rate [μL/h]	**distance from conduit exit** [mm]	$\boldsymbol{A}$ [mm^2]	$\boldsymbol{d_h}$ [μm]	$\boldsymbol{u_{avg}}$ [mm/s]	$\boldsymbol{Re}$
6.25	0	0.0079	23.990	0.2216	0.0056
	25	0.0295	88.846	0.0591	0.0056
12.5	0	0.0100	30.647	0.3457	0.0112
	25	0.0321	96.706	0.1080	0.0111
25	0	0.0109	33.307	0.6360	0.0225
	25	0.0412	122.726	0.1685	0.0219
50	0	0.0127	38.626	1.0976	0.0450
	25	0.0518	152.258	0.2682	0.0433
100	0	0.0153	46.596	1.8162	0.0898
	25	0.0618	178.807	0.4496	0.0853

Conduit capillary length

Throughout this study, it is assumed that gravity has a negligible effect on conduit geometry as interfacial forces dominate at the microscale. The Bond number (Bo), a dimensionless quantity representing the ratio of gravitational to interfacial forces acting on a fluidic system, gives the relative importance of these forces:

$$Bo = \frac{\Delta\rho g L^2}{\gamma} \qquad (S33)$$

Here, $\Delta\rho$ denotes the difference in density between medium in the conduit and the overlaying FC40, and L some characteristic length. A system's capillary length L_c corresponds to the characteristic length at which $Bo = 1$ indicating that gravitational forces begin to dominate. For conduits in this study, $L_c = 1.6$ mm. Therefore, to neglect gravity, the characteristic length must be much less than the capillary length (i.e., $L \ll L_c$). This can be determined by investigating the Bond number, which can be written as the ratio of hydrostatic to Laplace pressures:

$$Bo = \frac{\Delta\rho g h_{max}}{\frac{\gamma}{R}} \qquad (S34)$$

Using the assumption that $a \gg h_{max}$, the radius of curvature is simplified as $R = \frac{a^2}{2h_{max}}$ yielding:

$$Bo = \frac{\Delta\rho g a^2}{\gamma} \qquad (S35)$$

Comparing this to Eq. S33, it is easy to see the characteristic length is $L = a$. As the largest half-width in this study is $a \sim 0.6$ mm (Fig. 3ii; 2.5 times smaller than L_c), this corresponds to $Bo \sim 0.1$, showing that interfacial forces dominate and that gravity forces are negligible.

Semi-analytical solution for perfect slip at the media:FC40 interface

The semi-analytical solution is derived with the assumption of no-slip at the media:FC40 interface. This is analogous to assuming that the ratio of the viscosities of FC40 and medium is infinite such that $\lim_{\mu_{FC40}\to\infty} \frac{\mu_{FC40}}{\mu_{media}} = \infty$. To predict flow fields in conduits with any possible ratio of dynamic viscosities, we consider the other extreme in which perfect slip exists, in absence of any Marangoni effect, between immiscible fluids such that $\lim_{\mu_{FC40}\to 0} \frac{\mu_{FC40}}{\mu_{media}} = 0$.

The steps to derive the semi-analytical solution in such conditions mirror those outlined for the no-slip condition, and vary only by the boundary conditions applied. These are:

$$@y = \frac{h_{max}}{2};\ \frac{du}{dy} = 0 \quad and \quad @y = -\frac{h_{max}}{2};\ u = 0$$

Applying these conditions to the Navier-Stokes Eq. S2 yields:

$$h_{max}(x) = \left(\frac{6.5Q\mu ax}{\gamma} + h_0^4\right)^{0.25} \qquad (S36)$$

Slip and no-slip solutions are compared in Fig. S4.

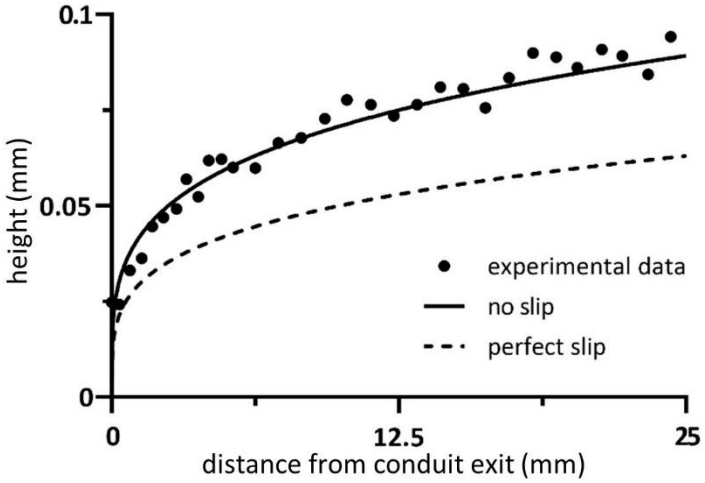


Fig. S4. Perfect slip versus no-slip semi-analytical solutions. Solutions are computed using Eq. S20 (no-slip) and Eq. S36 (slip; exit height assumed negligible) for a conduit (width 654 µm) perfused at 25 µL/h. Experimental data (reproduced from Fig. 3i) fit the no-slip condition.

Conduit failure

Conduits can withstand up to a maximum flow rate (Q_{max}) before reaching capillary instability which occurs when the contact angle exceeds $90°$ (defined as $\theta =$

$\sin^{-1}\left(\frac{2ah_{max}}{a^2+h_{max}^2}\right)$). This instability occurs when half-width equals maximum height ($a = h_{max}$), producing a perfect half-circular cross-section (Fig. S5).

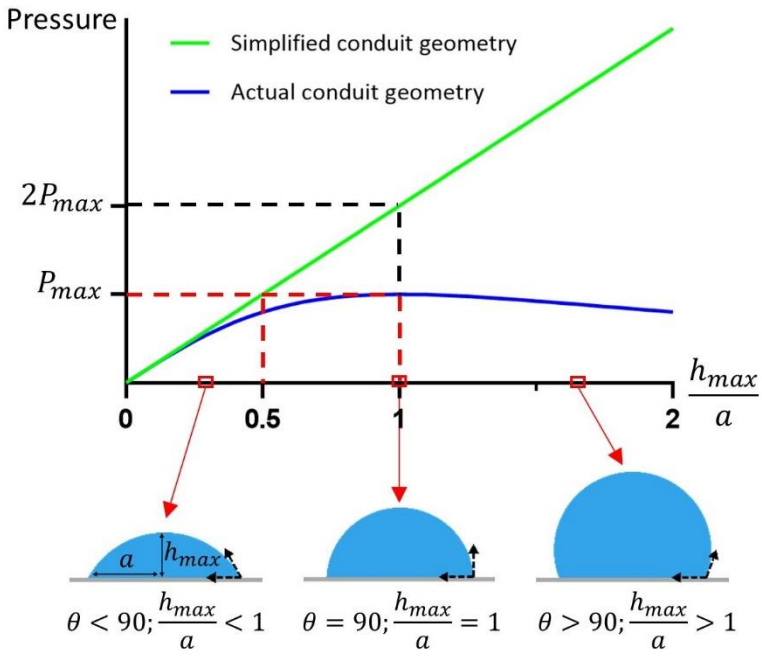


Fig. S5. Comparing pressures calculated using the simplified (green line) and exact numerical solutions (blue curve). For conduits with $\frac{h_{max}}{a} < 0.2$, the percent error between solutions is $\leq 4\%$, and – as $a \gg h_{max}$ – flow can be modelled as Poiseuille flow between two infinite parallel plates. As $\frac{h_{max}}{a}$ increases, this simplification becomes invalid and the two solutions deviate. The maximum pressure is reached when $\frac{h_{max}}{a} = 1$; thereafter, pressure decreases as $\frac{h_{max}}{a}$ increases above unity.

Flow through conduits relies on a negative pressure gradient in the direction of flow. The maximum pressure a conduit can withstand occurs when the contact angle reaches $\theta = 90°$; beyond this point, flow further upstream begins to pool creating a bulging conduit where $\theta > 90°$. This then leads to pinning-line failure (and the fluid wall breaks). The maximum flow rates achievable in conduits will depend on circuit geometry (i.e., conduit length and width)

and fluids used. Conduit failure will occur at the point of highest pressure in a straight conduit, and this will always be the inlet to the conduit. From the exact numerical model (blue curve in Fig. S5), we see that the maximum pressure is reached when $h_{max} = a$, and that this value can be extrapolated onto the simplified semi-analytical solution (Eq. S20, green curve in Fig. S5) when $h_{max} = 0.5a$. This h/a ratio is the limit at which the maximum flow rate is determined using the semi-analytical solution:

$$Q_{max} = \frac{\gamma}{26.08\mu a x} h_{max}^4$$

$$\therefore Q_{max} = \frac{\gamma a^3}{417.28\mu x} \quad (S37)$$

Fig. S5 highlights $\frac{h_{max}}{a}$ ratios where the simplified semi-analytical solution can be reliably used, which corresponds to $\frac{h_{max}}{a} \leq 0.2$, at which point there is $\leq 4\%$ error between semi-analytical and numerical solutions.

Collapsing numerical and semi-analytical solutions

There is good agreement between numerical and semi-analytical predictions of conduit properties for geometries investigated here. These theoretical projections can be collapsed onto a reference curve $h_{max,ref}$ by raising Q, a and μ to the 0.25 power and γ to the -0.25 power (see Equation S20) such as:

$$\frac{h_{max}}{h_{max,ref}} = \left(\frac{Q}{Q_{ref}}\right)^{0.25} \left(\frac{a}{a_{ref}}\right)^{0.25} \left(\frac{\mu}{\mu_{ref}}\right)^{0.25} \left(\frac{\gamma}{\gamma_{ref}}\right)^{-0.25} \quad (S38)$$

This equation accurately predicts the height profile of a conduit for any given volumetric flow rate, width, dynamic viscosity, and interfacial tension.

As our model is simplified by certain assumptions, we looked at their effect on predictions by comparing the semi-analytical model with the numerical model of the conduit (Fig. S6). Both models agree well with each other for conduit lengths of up to 100 mm, after which they diverge, differing by 6.5% at 300 mm. However, our conduits are typically ≤ 25 mm as they are printed on 6 cm dishes, so divergence is tiny.

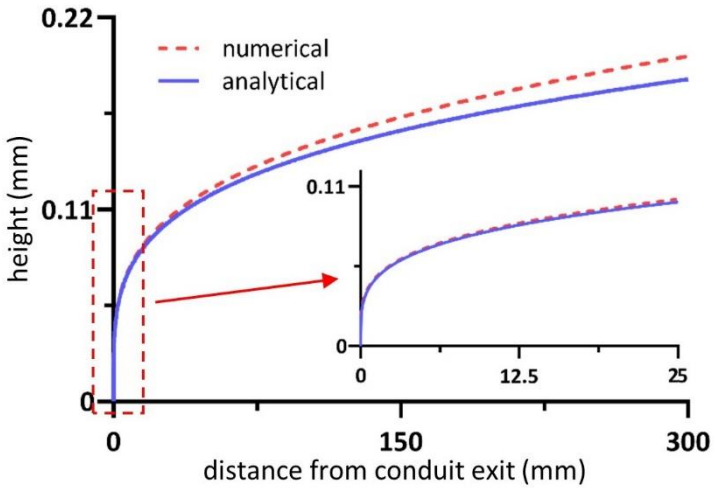


Fig. S6. Divergence of numerical and semi-analytical solutions. Heights were calculated using the iterative approach detailed in Eq. S21-31 (numerical solution), or Eq. S20 (semi-analytical solution), for a conduit with width 1 mm and flow rate 25 µL/h. Models diverge as conduit length increases, with a difference of 6.5% in conduit height 300 mm from the exit. For conduit lengths ≤25 mm relevant here (inset), the two models yield essentially similar results.

Error analysis for conduit-height predictions

To determine whether height measurements agree with theoretical predictions within an acceptable margin of error, the Root Sum of the Squares (RSS) error propagation method was used to calculate associated measurement uncertainty:

$$\varepsilon_{calc} = \sqrt{\left(\frac{\partial h_{max}}{\partial Q}\sigma_Q\right)^2 + \left(\frac{\partial h_{max}}{\partial \mu}\sigma_\mu\right)^2 + \left(\frac{\partial h_{max}}{\partial a}\sigma_a\right)^2 + \left(\frac{\partial h_{max}}{\partial x}\sigma_x\right)^2 + \left(\frac{\partial h_{max}}{\partial \gamma}\sigma_\gamma\right)^2}$$

Using u-substitution, the partial derivatives above (also known as sensitivity factors) are computed as follows:

$$\frac{\partial h_{max}}{\partial Q} = \frac{26.08\mu ax}{4\gamma\left(\frac{26.08Q\mu ax}{\gamma}\right)^{0.75}}$$

$$\frac{\partial h_{max}}{\partial \mu} = \frac{26.08Qax}{4\gamma\left(\frac{26.08Q\mu ax}{\gamma}\right)^{0.75}}$$

$$\frac{\partial h_{max}}{\partial a} = \frac{26.08Q\mu x}{4\gamma\left(\frac{26.08Q\mu ax}{\gamma}\right)^{0.75}}$$

$$\frac{\partial h_{max}}{\partial x} = \frac{26.08Q\mu a}{4\gamma\left(\frac{26.08Q\mu ax}{\gamma}\right)^{0.75}}$$

$$\frac{\partial h_{max}}{\partial \gamma} = \frac{26.08 Q \mu a x}{4\gamma^2 \left(\frac{26.08 Q \mu a x}{\gamma}\right)^{0.75}}$$

Next, the uncertainty of each individual variable (σ) is determined:

- σ_Q is the transducer uncertainty of the Harvard PhD Ultra syringe pump and from the user manual the pump's flow rate accuracy is $\pm 0.25\%$ ($\sigma_q = 0.0025Q$ µL/h).
- σ_μ is the standard deviation of dynamic viscosities taken from 10 separate solutions of DMEM + 10% FBS measured with a Hydramotion Viscolite 700 portable viscometer ($\sigma_\mu = 0.05$ mPa.s).
- σ_a is the standard deviation of conduit half-width along its 25 mm length (i.e., the error associated with jetting). For measurements performed on the Zeiss Axio Observer microscope, widths were measured at 35 distinct locations ($\sigma_a = 8$ µm).
- σ_x is determined by the microscope's specifications; for the Zeiss Axio Observer microscope, the accuracy of the stage in the x, y-plane corresponds to ± 1 µm ($\sigma_x = 1$ µm).
- σ_γ is unknown as interfacial tension is determined by fitting the semi-analytical solution to experimental data, and thus error in interfacial tension is not included.

Finally, error due to experimental uncertainty from the measurement of conduit height using beads (ε_{bead}) must also be included. This uncertainty takes into account the acquisition error (σ_{bead}) and twice bead diameter ($2d_{bead}$):

$$\varepsilon_{bead} = \sqrt{\sigma_{bead}^2 + 2d_{bead}^2}$$

To measure acquisition error, the distance between a single pair of beads (one on the surface of the dish and one on the media:FC40 interface) was measured 15 times and a standard deviation was calculated such that $\sigma_{bead} = 0.9$ µm. Unlike the calculated expanded sensitivity ε_{calc} which depends on location (i.e., the expected error increases as distance from the exit increases), ε_{bead} is a fixed quantity applied along the entire conduit such that the total propagated error is:

$$\varepsilon_{total} = \sqrt{\varepsilon_{calc}^2 + \varepsilon_{bead}^2}$$

Values for ε_{total} associated with height predictions are given in Fig. S7.

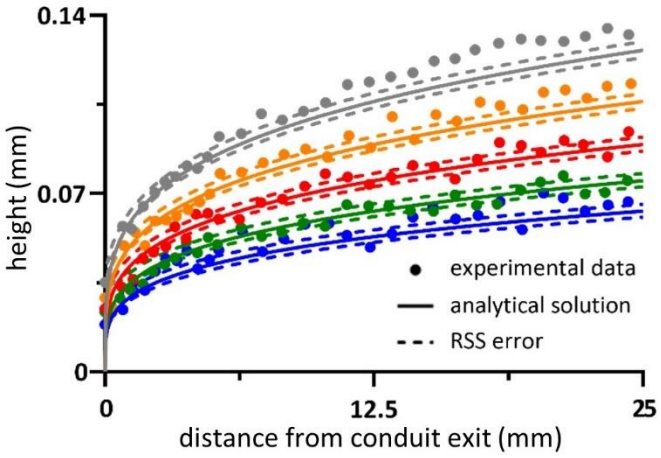


Fig. S7. Error (root sum of squares, RSS) propagation for semi-analytical predictions of conduit heights. Height predictions were calculated for conduits illustrated in Figure 3i (using Eq. S20) and errors (ε_{total}) determined (dashed lines bordering each coloured line – colour coding as in Fig. 3i).

Varying flow regimes

We studied the effect of flow regime on conduit height. First, we left a conduit at rest (no flow) for 24 h and took measurements the next day after starting flow. We then perfused a conduit overnight (for 24 h) and measured heights the following day. Comparing results with those obtained with freshly-printed conduits (Fig. 3i), although the variance of height over time is small between experiments (Fig. S8), the dynamic nature of interfacial tension could be expected to introduce a time-dependent variable to explain the small differences measured.

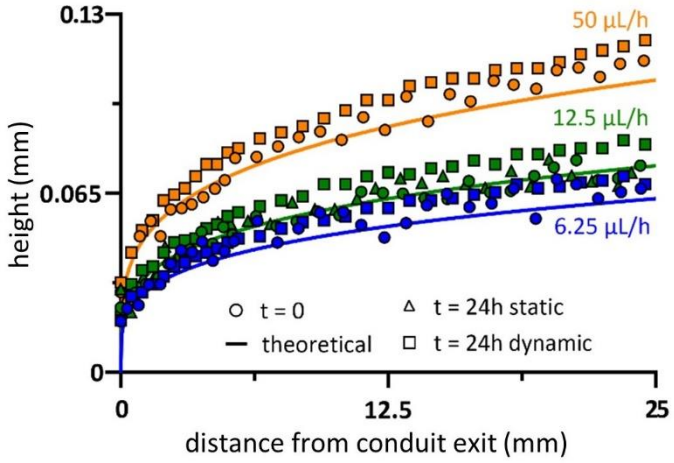


Fig. S8. Properties of fluid walls remain stable across different flow regimes. Heights in conduits experiencing different regimes were measured and compared with theoretical predictions (using Eq. 2). A conduit (width ~650 µm) was printed, left for 24 h without flow, then perfused at 12.5 µL/h, and heights measured ('t = 24 h static'). Another conduit was printed and infused for 24 h at 12.5 µL/h before measuring heights ('t = 24h dynamic'). Heights were also measured after decreasing flow to 6.25 µL/h, and then increasing it to 50 µL/h. Comparing these data with those in Fig. 3i ('t = 0') we find the different regimes had little effect on height.

Splitting conduits

In Fig. 5, we looked at the effect of one parent conduit splitting into two identical daughter conduits, and determined from continuity that flow through daughters is half the initial flow through the parent. This holds true generally for parents that split into n daughters so long as the geometry of daughters is identical. Then, $Q_d = \frac{Q_p}{n}$.

However, it is more difficult to predict flows through daughters of differing geometries. Consider Fig. S9 where some branches have different half widths a or length x:

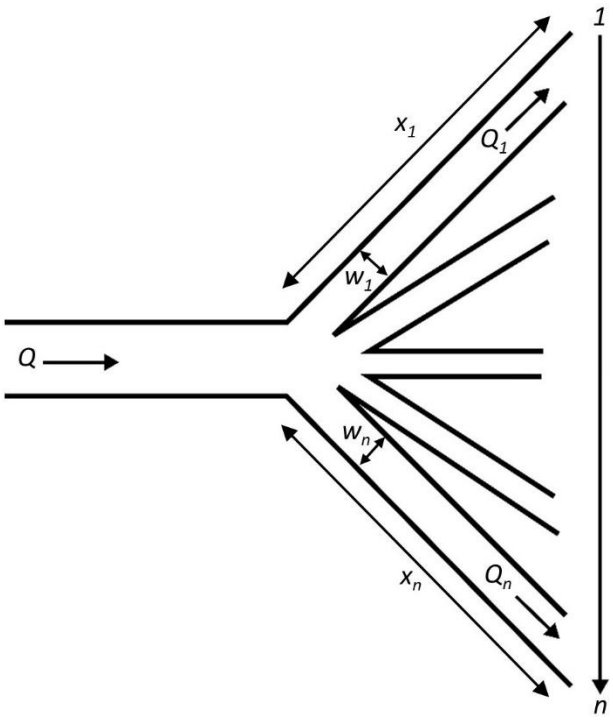


Fig. S9. Single parent conduit splitting into multiple daughter conduits. Each daughter conduit has a different length x or width w (half-width $a = \frac{w}{2}$), and therefore the resultant flow rate Q through each conduit will be different and determined by Eq. S39.

As the pressure P_{in} at the branch point must be the same for each branch, and since conduits are open ended (such that $P_0 = 0$), then $P_{in} - P_0 = \Delta P$ must be the same across each branch. From our scale analysis of the effect of exit height (h_0) on conduit shape, we know h_0 can be ignored if conduits are > 1 mm in length such that:

$$P_x = \left(\frac{417.28\gamma^3 \mu Q x}{a^7}\right)^{0.25}$$

Assuming each branching conduit is > 1 mm, the pressure drop in each must be the same, and we can equate the pressure gradient in any branch n to reference branch 1 as $P_n = P_1$:

$$\left(\frac{417.4\gamma^3 \mu Q_n x_n}{{a_n}^7}\right)^{0.25} = \left(\frac{417.4\gamma^3 \mu Q_1 x_1}{{a_1}^7}\right)^{0.25}$$

$$\frac{Q_n x_n}{{a_n}^7} = \frac{Q_1 x_1}{{a_1}^7}$$

$$Q_n = \frac{Q_1 {a_n}^7 x_1}{{a_1}^7 x_n}$$

Applying mass conservation, we know the input flow rate Q must equal the sum of all flow through branches (from 1 to n):

$$Q = \sum_1^n Q_n = \sum_1^n \frac{Q_1 {a_n}^7 x_1}{{a_1}^7 x_n}$$

We can remove Q_1 , x_1, and a_1 from the summation term as these are used as reference values for all other channels and are fixed:

$$Q = \frac{nQ_1x_1}{n{a_1}^7}\sum_1^n \frac{{a_n}^7}{x_n} = \frac{Q_1x_1}{{a_1}^7}\sum_1^n \frac{{a_n}^7}{x_n}$$

This gives:

$$Q_1 = \frac{Q{a_1}^7}{x_1\sum_1^n \frac{{a_n}^7}{x_n}} \quad (S39)$$

Since the reference conduit can be any of the daughter conduits, we can apply this equation to calculate flow fields through any conduit knowing only input flow rate Q and the geometrical properties of each conduit.

Height correction for apparent depth in microscope measurements

To determine conduit height using an inverted microscope, we first focus on a fluorescent bead at the media-FC40 interface. The height is then taken as the distance Δs by which the stage moves to focus on a bead on the surface of the dish. However, due to mismatches between the refractive indices of the medium containing the bead (water), and the medium surrounding the microscope objective (air), the focal position of the bead does not follow the axial movement of the stage. Rather, Δs appears smaller than reality.

To correct for this focal shift, consider Fig. S10 where the microscope stage is moved a distance Δs, and the resulting focal position is where the two red dashed lines converge, slightly below the original position of the bead. This derivation is based on a similar one presented in [28] but adds the extra layer of the polystyrene dish in the light path.

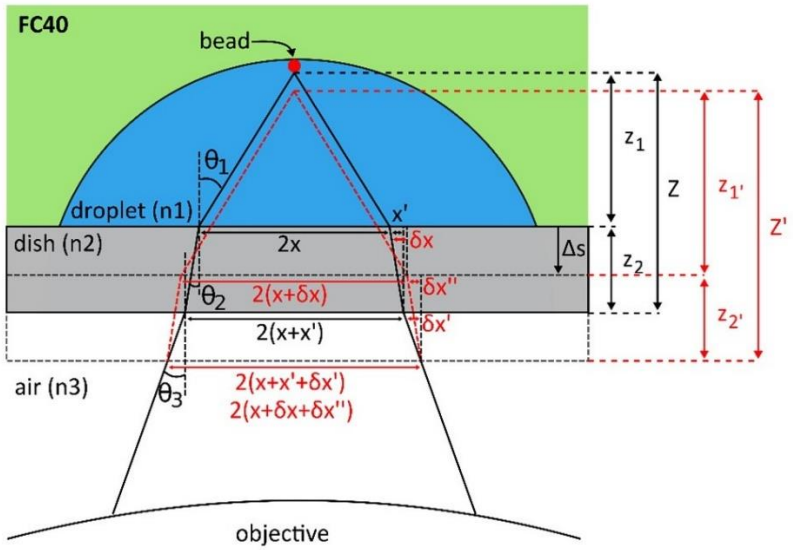


Fig. S10. Correcting focal shift when measuring conduit height on inverted microscopes. A drop of medium (which contains fluorescent beads and is overlaid with FC40) sits on a polystyrene dish on the stage of an inverted microscope. One red fluorescent bead stuck to the medium:FC40 interface at the peak of the spherical cap is brought into focus. Moving the stage a distance Δs closer to the objective moves the focus below the bead by a distance $\Delta f \neq \Delta s$ due to refraction of the light path across the different substrates. Using a combination of Snell's law and geometry, the correct value of Δf is determined using the numerical aperture of the objective lens, the refractive index of the culture medium around the bead, and the refractive index of the air at the objective, as in Eq. S40.

The marginal rays of the light cone emerging from the bead hit the dish at angle $\theta 1$, and have a half-width of x. Rays then travel through the dish at angle $\theta 2$ and emerge from

the dish into air at angle $\theta 3$ with a new half-width of $x + x'$, before entering the objective. As the microscope stage is moved, we can see that the angles of the rays stay the same, while half-widths of light cones vary.

If the original depth of focus is Z, and moving the microscope stage results in a new depth of focus Z', then the axial focal shift is given by $Z' - Z$.

In Fig. S10, we have the relationships:

$$Z = z_1 + z_2$$

$$Z' = z_1' + z_2{}'$$

Using trigonometry, we determine the following relations:

$$tan(\theta_1) = \frac{x}{z_1} \equiv z_1 = \frac{x}{tan(\theta_1)}$$

$$tan(\theta_2) = \frac{x'}{z_2} \equiv z_2 = \frac{x'}{tan(\theta_2)}$$

$$tan(\theta_1) = \frac{x + \delta x}{z_1{}'} \equiv z_1{}' = \frac{x + \delta x}{tan(\theta_1)}$$

$$tan(\theta_2) = \frac{\delta x''}{z_2{}'} \equiv z_2{}' = \frac{\delta x''}{tan(\theta_2)}$$

$$tan(\theta_3) = \frac{\delta x'}{\Delta s} \equiv \delta x' = \Delta s \times tan(\theta_3)$$

As the thickness $z2$ of the dish does not change, then:

$$z_2 = z_2' \rightarrow \frac{x'}{tan(\theta_2)} = \frac{\delta x''}{tan(\theta_2)} \rightarrow x' = \delta x''$$

Furthermore, we can see from the half-width of the light cone emerging from the dish after the stage has moved that:

$$x + x' + \delta x' = x + \delta x + \delta x''$$

$$\rightarrow x + x' + \delta x' = x + \delta x + x'$$

$$\therefore \delta x' = \delta x = \Delta s \times tan(\theta_3)$$

The focal shift is therefore:

$$\Delta f = Z' - Z = z_1' + z_2' - z_1 - z_2$$

$$\Delta f = z_1' - z_1 = \frac{x + \delta x}{tan(\theta_1)} - \frac{x}{tan(\theta_1)}$$

$$\Delta f = \frac{\delta x}{tan(\theta_1)}$$

$$\therefore \Delta f = \Delta s \frac{tan(\theta_3)}{tan(\theta_1)}$$

This can now be expressed in terms of the numerical aperture of the objective, NA:

$$NA = n1 \times sin(\theta_1) \leftrightarrow \theta_1 = sin^{-1}\left(\frac{NA}{n1}\right)$$

Therefore:

$$\Delta f = \Delta s \frac{\tan(sin^{-1}\left(\frac{NA}{n3}\right)}{\tan(sin^{-1}\left(\frac{NA}{n1}\right)} \qquad (S40)$$

For small NA, we use the small-angle approximation:

$$sin(\theta) = \theta, tan(\theta) = \theta$$

and:

$$\Delta f = \Delta s \frac{tan\left(\frac{NA}{n3}\right)}{tan\left(\frac{NA}{n1}\right)} = \Delta s \frac{n1}{n3}$$

To confirm the accuracy of Eq. S40 for height corrections, we measured the heights of sessile drops of known volumes with the Olympus microscope. Droplets of 0.5 and 1 µL were

deposited on polystyrene culture dishes, made from the same media + bead mixture used to measure conduit heights. As before, the diameter and heights of drops were measured, theoretical heights determined using the known volume and measured footprint. The heights measured using beads were then corrected using Eq. S40 and show good agreement with theory (using the height-to-volume equation for sessile drops [22]; average of 2% difference between theoretical and corrected heights across 21 individual measurements; Table S2).

Table S2. Comparison between sessile-drop height measurements and theoretical predictions using Eq. S40

drop volume (µL)	footprint diameter (mm)	measured height (mm)	theoretical height (mm)	corrected height (mm)	ratio corrected vs theoretical
0.5	1.666	0.294	0.422	0.427	1.012
	1.670	0.278	0.421	0.404	0.960
	1.663	0.270	0.424	0.392	0.926
	1.667	0.287	0.422	0.417	0.989
	1.678	0.295	0.418	0.429	1.026
	1.685	0.290	0.415	0.421	1.016
	1.680	0.262	0.417	0.381	0.913
	1.687	0.252	0.414	0.366	0.884
	1.696	0.273	0.411	0.397	0.966
1	2.058	0.368	0.549	0.535	0.974
	2.078	0.377	0.541	0.548	1.013
	2.101	0.370	0.532	0.538	1.012
	2.136	0.376	0.518	0.546	1.056
	2.134	0.345	0.518	0.501	0.967
	2.136	0.334	0.518	0.485	0.938
	2.165	0.315	0.506	0.458	0.904
	2.157	0.350	0.509	0.509	0.999
	2.167	0.338	0.506	0.491	0.972
	2.113	0.363	0.527	0.528	1.001
	2.126	0.350	0.521	0.509	0.975
	2.138	0.370	0.517	0.538	1.040

Maintaining constant shear along fluid-walled conduits

For conduits with chokes, the profile of both choke and conduit are determined using Eq. 2. While the exit height of the choke can be assumed to be zero, the conduit-choke junction determines conduit exit height ($x_{conduit} = 0$) as this will naturally be larger than the choke's starting height ($x_{choke} = L_{choke}$). We assume the transition between the choke start to conduit exit is small so the Laplace pressure is constant, and that the pressure-head difference due to FC40 is negligible; then, we equate the Laplace pressure in both regions such that $\Delta P_{conduit(x\,=\,0)} = \Delta P_{choke(x\,=\,L)}$ and hence $R_{conduit(x\,=\,0)} = R_{choke(x\,=\,L)}$. As the radius of curvature $R = \frac{a^2+h^2}{2h}$, we solve for conduit starting-height yielding:

$$h_{conduit(x\,=\,0)} = \frac{a_{choke}^2 + h_{choke(x=L)}^2 - \sqrt{\left(a_{choke}^2 + h_{choke(x=L)}^2\right)^2 - 4a_{conduit}^2 h_{choke(x\,=\,L)}^2}}{2h_{choke(x=L)}}$$

Here, a is fixed and defined when printing the conduit, and $h_{choke(x=L)}$ is the height of the choke before the junction and is calculated from the semi-analytical solution. Since the junction has a saddle shape, for conduits in Fig. 4B,C, the height of the choke, $h_{choke(x=L)}$, is taken at a distance away from the junction equivalent to one choke width (e.g., for choke width = 400 µm, $L_{choke} = 10$ mm, $h_{choke(x=L)} = 9.6$ mm). For conduits with geometries where $a_{conduit} \gg h_{conduit}$ and $a_{choke} \gg h_{choke}$, the radius of curvature is simplified to $R = \frac{a^2}{2h}$ and thus:

$$h_{conduit(x\,=\,0)} = \frac{a_{conduit}^2 h_{choke(x\,=\,L)}}{a_{choke}^2}$$

In this case, introducing a choke has the effect of increasing $h_{conduit}$ proportionately to $\frac{a_{conduit}^2}{a_{choke}^2}$, and maintains the conduit at an approximately constant height upstream of the choke due to the small pressure drop.

Semi-analytical solution for shear stress

We evaluate the wall shear stress at any location along conduit length and any z-location across its width. Starting from Eq. S6 and substituting u_{max} with Eq. S10 yields:

$$u_{max(z)} = \frac{Q{h_z}^2}{0.6{h_{max}}^3 a} \tag{S41}$$

Since $\tau = \mu\frac{du}{dy}$, and differentiating $u(y) = \left(1 - \frac{4y^2}{h_{max}^2}\right)u_{max}$ to obtain $\frac{du}{dy} = \frac{8y}{h_{max}^2}u_{max}$, we express the shear stress in the conduit as:

$$\tau_{max(z)} = \frac{8\mu y}{{h_z}^2}u_{max(z)} \tag{S42}$$

Substituting $u_{max(z)}$ from Eq. S41 into Eq. S42 we get:

$$\tau_{max(z)} = \frac{8Q\mu}{0.6{h_{max}}^3 a}y$$

Wall shear stress is evaluated at $y = \frac{h_z}{2}$ hence:

$$\tau_{max(z)} = \frac{4Q\mu h_z}{0.6{h_{max}}^3 a} \quad (S43)$$

At the conduit centre ($z = 0$), $h_z = h_{max}$, therefore Eq. S43 becomes:

$$\tau_{max(0)} = \frac{4Q\mu}{0.6h_{max}^2 a} \quad (S44)$$

Expressing $\tau_{max(z)}$ in terms of $\tau_{max(0)}$ using Eq. S44:

$$\tau_{max(z)} = \tau_{max(0)} \frac{h_z}{h_{max}} \quad (S45)$$

Now evaluating τ_{max} by substituting h_{max} with Eq. S20 finally yields:

$$\tau_{max(z)} = 1.28 \sqrt{\frac{\mu\gamma Q}{a^3 x}} \frac{h_z}{h_{max}} \quad (S46)$$

Effect of a choke on the gradient of wall shear stress

The addition of a choke creates a region of nearly uniform shear upstream of the choke (i.e., $\frac{d\tau}{dx}$ is very small). This shear distribution would be achieved in a conduit without choke, but at a much farther distance. The choke allows users to 'skip ahead' through a conduit to reach a desired shear stress distribution. Conduits with small $\frac{d\tau}{dx}$ can be obtained at operational scales (that fit in 60 mm dishes) that would require much longer lengths of

conduit otherwise. To investigate the order-of-magnitude effect of a choke on $\frac{d\tau}{dx}$, consider the two systems in Fig. S11:

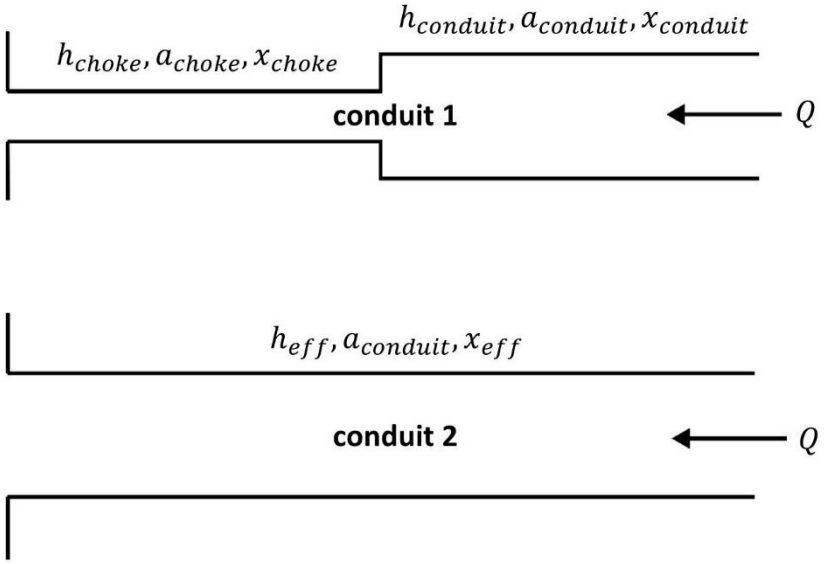


Fig. S11. Conduits with and without a choke. Both conduits are perfused at the same flow rate Q, and $a_{conduit}$ in conduit 1 is equivalent to $a_{conduit}$ in conduit 2.

Due to the choke in conduit 1, $h_{conduit} \approx h_{choke}\left(\frac{a_{conduit}}{a_{choke}}\right)^2$. From our semi-analytical equation:

$$h_{choke} = \left(\frac{26.08 Q \mu a_{choke} x_{choke}}{\gamma}\right)^{0.25}$$

$$\therefore h_{conduit} \approx \left(\frac{26.08 Q \mu a_{choke} x_{choke}}{\gamma}\right)^{0.25} \left(\frac{a_{conduit}}{a_{choke}}\right)^2 \quad (S47)$$

Next, for the same flow rate we determine the distance x_{eff} that conduit 2 (which has width $a_{conduit}$) would need to reach so that $h_{eff} = h_{conduit}$ at the junction between conduits (i.e., the effective length introduced by the choke):

$$\left(\frac{26.08Q\mu a_{conduit}x_{eff}}{\gamma}\right)^{0.25} = \left(\frac{26.08Q\mu a_{choke}x_{choke}}{\gamma}\right)^{0.25}\left(\frac{a_{conduit}}{a_{choke}}\right)^{2}$$

$$a_{conduit}x_{eff} = a_{choke}x_{choke}\left(\frac{a_{conduit}}{a_{choke}}\right)^{8}$$

$$\therefore x_{eff} = x_{choke}\left(\frac{a_{conduit}}{a_{choke}}\right)^{7} \quad (S48)$$

As an example, if $x_{choke} = 1$ mm, $a_{choke} = 0.2$ mm, and $a_{conduit} = 0.5$ mm, then $x_{eff} = 0.6$ m.

Next, we evaluate the relationship between $\frac{d\tau}{dx}$ and the distance x along the conduit. Shear stress in the conduit ($@h_{max(x)}$) is:

$$\tau = 1.28\left(\frac{Q\mu\gamma}{a^3x}\right)^{0.5} \quad (S49)$$

$$\therefore \tau \propto \left(\frac{1}{a^3x}\right)^{0.5}$$

As:

$$\frac{d}{dx}\left(\left(\frac{1}{a^3x}\right)^{0.5}\right) = -\frac{1}{2}a^3\left(\frac{1}{a^3x}\right)^{\frac{3}{2}}$$

Then:

$$\frac{d\tau}{dx} \propto a^3 \left(\frac{1}{a^3 x}\right)^{\frac{3}{2}} \propto \left(\frac{1}{ax}\right)^{\frac{3}{2}} \qquad (S50)$$

Using Eq. S48, the shear gradient after the choke is:

$$\left(\frac{d\tau}{dx}\right)_{choke} \propto \left(\frac{1}{a_{conduit} x_{eff}}\right)^{\frac{3}{2}} \propto \left(\frac{1}{a_{conduit} x_{choke} \left(\frac{a_{conduit}}{a_{choke}}\right)^7}\right)^{\frac{3}{2}} \qquad (S51)$$

The shear gradient for a conduit without choke at x_{choke} is:

$$\left(\frac{d\tau}{dx}\right)_{no\ choke} \propto \left(\frac{1}{a_{conduit} x_{choke}}\right)^{\frac{3}{2}} \qquad (S52)$$

Hence, the change in $\frac{d\tau}{dx}$ from the addition of a choke can be evaluated as:

$$\frac{\left(\frac{d\tau}{dx}\right)_{no\ choke}}{\left(\frac{d\tau}{dx}\right)_{choke}} \equiv \frac{\left(\frac{1}{a_{conduit} x_{choke}}\right)^{\frac{3}{2}}}{\left(\frac{1}{a_{conduit} x_{choke} \left(\frac{a_{conduit}}{a_{choke}}\right)^7}\right)^{\frac{3}{2}}} \equiv \left(\frac{a_{conduit}}{a_{choke}}\right)^{\frac{21}{2}} \qquad (S53)$$

In our example, $\frac{d\tau}{dx}$ in the conduit after the choke will be ~ 15000 fold smaller than $\frac{d\tau}{dx}$ in the straight conduit at the same distance from the exit (equivalent to a 99.99% decrease). Table

S3 gives the percent change in τ over 1 cm upstream of a choke, for various choke lengths and $\frac{a_{conduit}}{a_{choke}}$ ratios:

Table S3. % change in τ over 1 cm for varying half-width ratios and choke lengths

$\frac{a_{conduit}}{a_{choke}}$	% change in τ over 1 cm with choke length of:		
	1 mm	5 mm	10 mm
2.5	0.81	0.16	0.08
2	3.69	0.77	0.39
1.25	43.18	16.07	9.08
1	69.85	42.26	29.29

Error from $\frac{h}{a}$ simplification on shear stress gradient in choked conduits

The height of a conduit after a choke is estimated without simplifications as:

$$h_{conduit(exact)} = \frac{a_{choke}^2 + h_{choke}^2 - \sqrt{(a_{choke}^2 + h_{choke}^2)^2 - 4a_{conduit}^2 h_{choke}^2}}{2h_{choke}} \quad (S54)$$

However, Eq. S54 is simplified when assuming the radius of curvature is expressed as $R = \frac{a^2}{2h}$, yielding:

$$h_{conduit(simp)} = h_{choke}\left(\frac{a_{conduit}}{a_{choke}}\right)^2 \quad (S55)$$

The error or difference from this simplification is given as:

$$\frac{h_{conduit(exact)}}{h_{conduit(simp)}} = c \quad (S56)$$

where c is a constant dependent on h_{choke}, a_{choke}, and $a_{conduit}$. From Eq. S55, the effective length introduced by the choke is determined (as in Eq. S48):

$$x_{eff(simp)} = x_{choke}\left(\frac{a_{conduit}}{a_{choke}}\right)^7 \quad (S57)$$

Introducing Eq. S57 into the expression for wall shear stress (Eq. S49) yields:

$$\tau_{simp} = 1.28\left(\frac{Q\mu\gamma}{a^3 x_{eff}}\right)^{0.5} \quad (S58)$$

The radius of curvature simplification from Eq. S55 introduces an error (c) in Eq. S58; this is accounted for using Eq. S56, such that x_{eff} and τ become:

$$x_{eff(corrected)} = x_{choke}c^4\left(\frac{a_{conduit}}{a_{choke}}\right)^7 \quad (S59)$$

$$\tau_{corrected} = 1.28\left(\frac{Q\mu\gamma}{a^3 x_{eff(corrected)}}\right)^{0.5} \quad (S60)$$

Finally, as in Eq. S44, τ may also be expressed in terms of conduit height rather than effective length, using the exact (Eq. S54) or simplified equation (Eq. S55). The exact expression using Eq. S54 is:

$$\tau_{exact} = \frac{4Q\mu}{0.6h^2_{conduit(exact)}a_{conduit}} \quad (S61)$$

As shear stress in Fig. 4D is calculated using Eq. S61, we evaluate the effect of the radius of curvature simplification on τ (Eq. S58), and subsequent correction (Eq. S60), for the choked conduits in Fig. 4B. Table S4 summarizes the estimated % change in τ for these conduits over 1 cm upstream of the choke, showing equivalent results for Eq. S60 and S61:

Table S4. Effect of h/a simplification on τ predictions

choke length	1 mm	5 mm	10 mm
$h_{conduit(exact)}$ (Eq. S54) [µm]	157	287	322
$h_{conduit(simp)}$ (Eq. S55) [µm]	152	220	237
c (Eq. S56)	1.03	1.31	1.36
$x_{eff(simp)}$ (Eq. S57) [m]	0.58	2.54	3.28
$x_{eff(corrected)}$ (Eq. 59) [m]	0.66	7.39	11.19
τ_{simp} @ choke (Eq. S58) [Pa]	9.76E-04	4.65E-04	3.87E-04
τ_{simp} @ 1 cm (Eq. S58) [Pa]	9.68E-04	4.64E-04	3.87E-04
$d\tau/dx$ 1cm (%)	0.85	0.20	0.15
$\tau_{corrected}$ @ choke (Eq. S60) [Pa]	9.13E-04	2.73E-04	2.10E-04
$\tau_{corrected}$ @ 1 cm (Eq. S60) [Pa]	9.06E-04	2.73E-04	2.10E-04
$d\tau/dx$ 1cm (%)	0.75	0.07	0.04
τ_{exact} @ choke (Eq. S61) [Pa]	9.31E-04	2.78E-04	2.14E-04
τ_{exact} @ 1 cm (Eq. S61) [Pa]	9.24E-04	2.78E-04	2.14E-04
$d\tau/dx$ 1cm (%)	0.75	0.07	0.04

Culturing cells in fluid-walled conduits

We plated human umbilical vein endothelial cells (HUVECs) in conduits (± choke) and perfused them overnight (at 25 or 50 µL/h) to look at the effect of flow on cell viability. Fig. S11 shows that after 24 h, flow had little effect on HUVEC morphology or alignment, which is to be expected from the magnitude of the shear stress in such conduits (see Fig. 4D) [5].

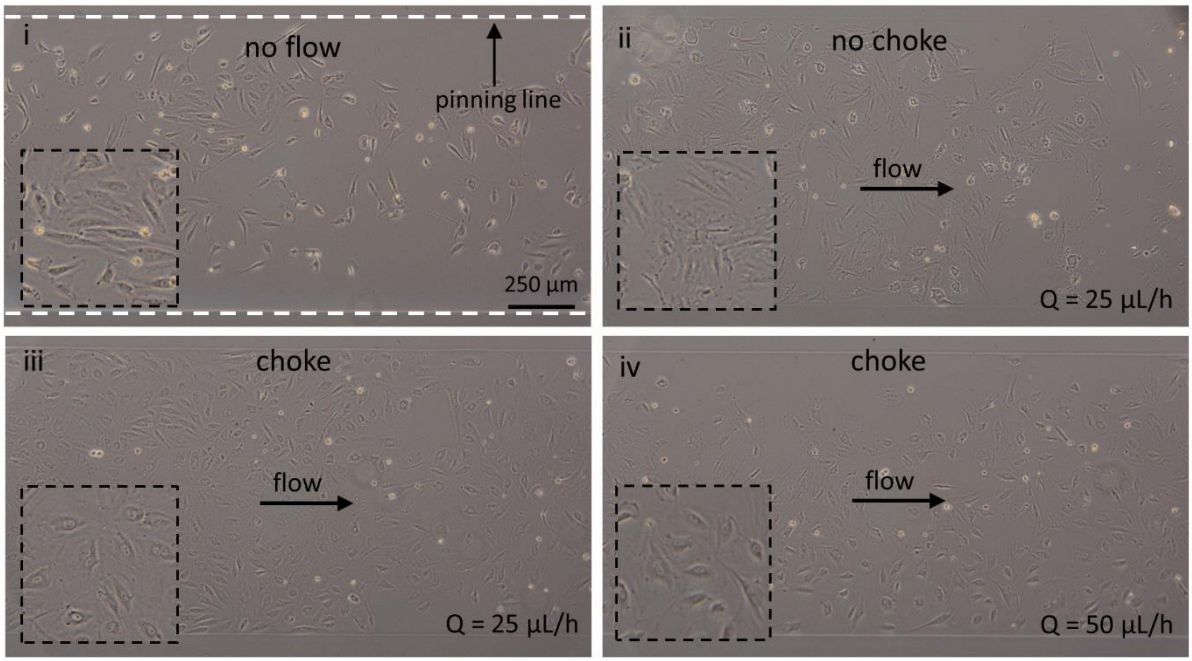


Fig. S12. HUVECs in fluid-walled conduits. Cells were plated in 4 conduits ± chokes (conduit width 1 mm; choke width 400 µm) and incubated overnight before flow was applied. Insets show close-ups of cells in conduits. **(i)** Control conduit without flow. White dashed lines indicate conduit pinning lines (triple contact line polystyrene-media-FC40). **(ii)** Conduit without choke, perfused at 25 µL/h. **(iii)** Conduit with choke, perfused at 25 µL/h. **(iv)** Conduit with choke, perfused at 50 µL/h.

Supplementary Movie

Movie S1. Addition of FBS to DMEM immediately induces the no-slip condition

Two square chambers (1.9 x 1.9 mm) each containing 400 nL DMEM plus 4 mg/mL red dye (Allura Red in H_2O, Sigma) and 3-10 µm glass beads (1:1000 dilution, Polysciences, Inc., 07666) are each surrounded by FC40 walls; these chambers sit in a dish filled with FC40 on the Olympus microscope (4x objective). Next, the jetting needle (diameter 500 µm) – held vertically by attachment to the microscope condenser, filled with FC40, and connected to a syringe pump – is lowered through the fluorocarbon until ~1 mm above the footprint of the FC40 wall between the two chambers. This needle gives the circular shadow in the middle of video images. The movie begins as the pump is started and projects a submerged FC40 jet downwards at 8 µL/s; this induces shear at the FC40:medium interface so beads in both chambers swirl rapidly. After

~10 s, 0.5 µL DMEM + 10% FBS is manually pipetted into the bottom chamber; beads in the inoculated chamber rapidly stop moving, as those in the upper one continue. This shows that FBS immediately induces a no-slip interface.

Video link: Movie S1

Statement of Authorship for joint/multi-authored papers for PGR thesis

To appear at the end of each thesis chapter submitted as an article/paper

The statement shall describe the candidate's and co-authors' independent research contributions in the thesis publications. For each publication there should exist a complete statement that is to be filled out and signed by the candidate and supervisor **(only required where there isn't already a statement of contribution within the paper itself).**

Title of Paper	Predicting flows through microfluidic circuits with fluid walls
Publication Status	Submitted for Publication
Publication Details	C. Deroy, N. Stovall-Kurtz, F. Nebuloni, C. Soitu, P. R. Cook, and E. J. Walsh, Microsystems and Nanoengineering, (Under Review).

Student Confirmation

Student Name:	Cyril Deroy		
Contribution to the Paper	Lead author, contributed to model development, designed and performed majority of experiments, led data collection, analysis, and figure preparation, coordinated and contributed to manuscript writing and editing.		
Signature		Date	27/09/2021

Supervisor Confirmation

By signing the Statement of Authorship, you are certifying that the candidate made a substantial contribution to the publication, and that the description described above is accurate.

Supervisor name and title: Prof. Edmond Walsh		
Supervisor comments		
Signature 	Date	27/09/21

This completed form should be included in the thesis, at the end of the relevant chapter.

Chapter 4: Reconfiguring microfluidic circuits to isolate and retrieve cells of interest

Authors: Cyril Deroy, James H. R. Wheeler, Agata Rumianek, David R. Greaves, Peter R. Cook, William M. Durham, Kevin Foster, Edmond J. Walsh

Abstract

The application of microfluidics to biology reveals that fluid flows profoundly influence cell physiology and behaviour. However, as conventional microfluidic devices are surrounded by solid walls, it is often difficult to isolate or extract specific cells from within flow environments for downstream analyses. We now describe a general and flexible approach to reconfigure microfluidic circuits in real-time and without interrupting flows using circuits with fluid walls. We fabricate 3D-printed adaptors that readily transform conventional microscopes into reconfiguring tools that can re-shape circuits made on standard Petri dishes with an accuracy of several microns. As proof of concept, we isolate and recover (with 80% viability) sub-populations of murine macrophages chemotaxing towards complement component 5a. We then apply the method to isolate and extract sub-populations of surface-attached bacteria (*Pseudomonas aeruginosa*) migrating towards lethally-high antibiotic concentrations and analyse their long-term viability using conventional cell culture approaches. The technique allows users to selectively extract specific sub-populations of live cells from within microfluidic devices with the potential to subsequently analyse their genetics and physiology. We anticipate that the addition of these simple new tools to the microscopes used daily by biomedical scientists will thus facilitate adoption of microfluidic approaches.

Introduction

Microfluidic experiments can generate well-defined physical and chemical stimuli that vary across the micrometre-scales relevant for individual cell behaviour and physiology. As such, they have been instrumental in advancing our understanding of microbial response phenotypes [1]. However, whilst cells within microfluidic devices can be visualised by time-lapse microscopy, it remains difficult to retrieve responding cells from conventional microfluidic devices made with polydimethylsiloxane (PDMS), as they are inaccessibly buried behind solid confining walls. This limits the ability to relate genotype to the phenotypic differences observed in these systems. Although open microfluidic systems in which at least one solid wall is removed can improve sample accessibility [2], it remains challenging to isolate and extract specific cells of interest from flowing micro-environments.

The recent development of fluid-walled microfluidics – where samples in the aqueous phase are confined behind a liquid interface made of the immiscible fluorocarbon, FC40 – allows fluid walls to be built by a three-axis traverse (a 'printer', [3]). This approach can be used to construct isolating fluid chambers around cells growing on standard Petri dishes [4]. However, these processes are conducted blindly, as cells are not imaged simultaneously through a microscope. This limits the degree to which circuit modifications can be targeted to specific events or cell behaviours that can only be observed microscopically. Furthermore, cells are often sensitive to changing flows [5]–[7], and so even moving a dish from a microfluidic device to a microscope can perturb cell position and physiology. Moreover, it remains challenging to isolate and extract desired cells from a population growing in flowing micro-environments. Therefore, we devised a general and flexible methodology to do so.

As proofs of concept, we isolate and extract sub-sets of cells from two very different populations – murine macrophages and early-stage biofilms of *Pseudomonas aeruginosa* – as cells migrate up flow-generated gradients of two very different chemoattractants (i.e., macrophages towards complement component 5a (C5a), [8], [9], and the bacteria – counter-intuitively – towards the lethal antibiotic, ciprofloxacin [10]). We first show that fluid-walled circuits can be reconfigured using the printer to isolate a targeted population of macrophages as they migrate towards C5a. Secondly, we 3D-print adaptors that can be attached to a conventional inverted microscope with a motorised stage; then, the microscope itself becomes a tool that is used both to image cells and isolate the desired population. This means that circuits can be reconfigured *in situ* on the microscope with continuous flow and imaging. Both these methods are easily tuned to a user's imaging system and requirements, so we anticipate that they will facilitate adoption of more microfluidic approaches in the biosciences.

Results

Workflow

The general workflow involves printing an 'm'-shaped circuit with two arms that join to form a central conduit connected to a sink, and seeding cells in the central conduit where they attach to the surface of the dish (**Fig. 1Ai**). Dishes are now transferred to a microscope where stable chemoattractant gradients are established over cells. Needles are inserted into each circuit arm, and medium infused through one and medium plus chemoattractant through the other; a third needle inserted into the sink simultaneously withdraws fluid at a rate matching the two inputs. All three needles are connected to syringe pumps via tubing and held above the circuit by a 3D-printed holder attached to the dish. Both input liquids flow as laminar streams down the central arm, and diffusion creates a stable gradient of chemoattractant across its width (**Fig. 1Aii**; **Fig. S1**; **Materials and Methods**). Once cells move up the gradient, new fluid walls are built around responding cells to isolate them from all others using either a 'printer' or modified microscope (**Fig. 1Aiii**), and cells extracted prior to downstream analysis (**Fig. 1Aiv**,**v**).

Printing fluid-walled microfluidic circuits

The circuit is made using a custom printer that consists of a dispensing needle connected to a syringe pump mounted on a three-axis traverse (**Fig. 1B**; [3]); the needle infuses growth medium onto the surface of a standard Petri dish (**Fig. 1Ci-iii**, see **Materials and Methods**). Once printed, the circuit is overlaid with FC40 – a biocompatible and immiscible fluorocarbon – that prevents circuit evaporation (**Fig. 1Civ**). At the microscale, interfacial forces firmly pin medium to the substrate, and fluid walls – interfaces between the two immiscible phases – confine medium to the printed pattern. Fluid is easily added to and

removed from such a circuit as fluid walls can be pierced at any point by pipets or dispensing needles; these walls spontaneously seal around inserted tubes, and then reseal without leaks when tubes are withdrawn. Fluid walls also morph above unchanging footprints to accommodate accompanying pressure differences (i.e., the pinning lines that make up the circuit footprint remain unchanged as circuit heights and contact angles change [3]). Soon after printing, pressure inside these circuits equilibrates and all flows cease. Note that these circuits can also be fabricated using a stylus or a micro-jet ([11], [12]).

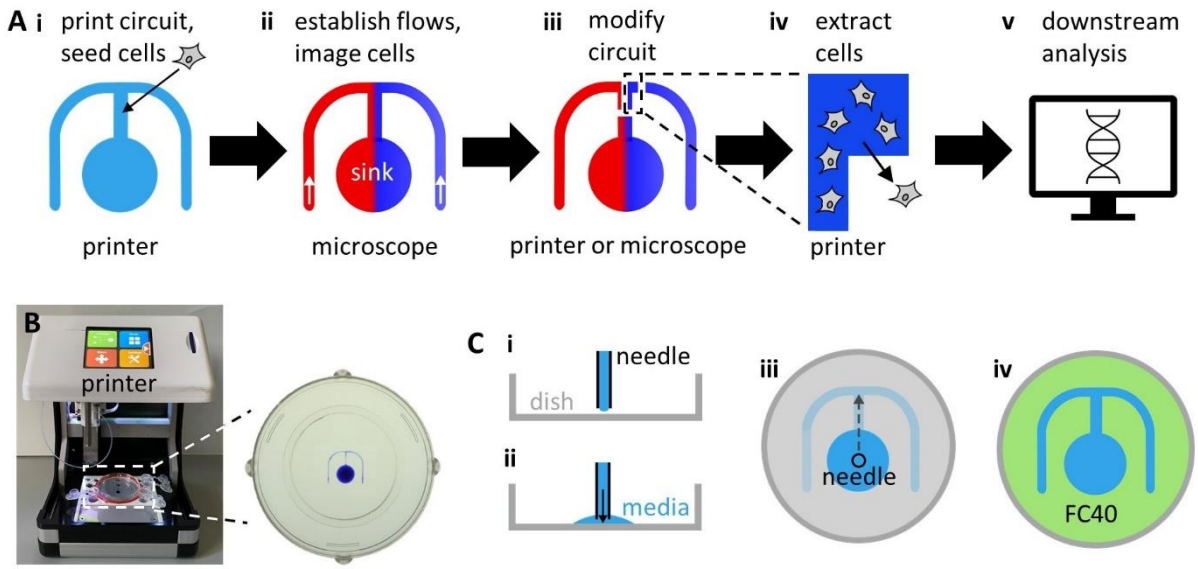


Fig. 1. Overview. **(A)** Workflow. **(i)** An 'm'-shaped circuit is printed on a dish, and cells seeded into the central arm. **(ii)** The dish is transferred to a microscope, dispensing needles inserted into lateral arms of the 'm', and media -/+ chemoattractant (red/blue) pumped into the circuit to flow to the sink; diffusion between laminar streams creates a stable chemoattractant gradient across the central conduit. The microscope is used to image chemotaxing cells and to identify rapidly-migrating ones. **(iii)** New isolating fluid walls are built around chemotaxing cells (on either the printer or microscope). **(iv)** The printer extracts isolated cells from the reconfigured chamber. **(v)** Cells are now analysed in any desired way (e.g., by RNA sequencing in this cartoon). **(B)** Printer with 6 cm dish. Close-up shows the dish with printed circuit (+ blue

dye for visualization). **(C)** Printing the circuit. **(i)** A dispensing needle is held by the printer above a dish. **(ii)** Media pumped on to the dish is held in place by interfacial forces. **(iii)** Moving the needle as it infuses media prints the circuit. **(iv)** Overlaying FC40 (green) prevents evaporation.

Managing positional information

During the next and subsequent steps in the workflow (**Fig. 1A**), the dish is moved back and forth between printer and microscope, and positional information about the circuit must be transferred between the two; this is achieved using 3D-printed adaptors that fix the orientation of the dish on the two instruments. Thus, a locating ring with a triangular protrusion attaches to the outside of the dish (**Fig. 2Ai**), and the ring and protrusion fit into appropriate indents in custom adaptors on the stages of the printer and microscope (**Fig. 2Aii,iii**).

Exposing cells to chemical gradients, imaging, and isolating migrating cells

Dishes are now transferred to a microscope, needles inserted, stable gradients of chemoattractant established over cells, cells imaged as some migrate up the gradient, and the desired sub-population identified (**Fig. 1Aii**). This sub-population is isolated by building new fluid walls around it (**Fig. 1Aiii**) using a PTFE (polytetrafluoroethylene) stylus with a conical tip. This is achieved in two ways that use the same principle; the stylus is attached either to the three-way traverse on the printer (**Fig. 2Bi**, inset), or to the condenser on a standard inverted microscope with a motorised stage (**Fig. 2Bii**; attachment again depends on the use of 3D-printed adaptors, **Supplementary SVG files**). In both cases, the stylus is lowered (either by the programmed traverse, or by lowering the condenser manually) through FC40 and the medium in the circuit until the tip contacts the surface of the dish. As

FC40 wets PTFE and polystyrene better than medium [13], this brings the FC40 down onto the bottom surface of the dish. Next, the stylus is moved relative to the substrate and as it moves, it displaces media from within the circuit. This displaced media is replaced by the surrounding FC40 creating new fluid walls that can be constructed around the desired sub-population of migrating cells (**Fig 2C**).

Prior to reconfiguring circuits on the printer (**Fig. 2Bi**), flow through the circuit on the microscope is stopped, and input and output needles withdrawn. Relative positions of responding and non-responding macrophages change little during transfer to the printer, or subsequently in the few minutes the printer takes to build new isolating walls at room temperature, as these cells adhere so strongly to polystyrene moving ~1 μm/ min at 37°C ([14]). However, a small proportion of bacterial cells often detach from surface-attached biofilms [15]–[17]. Under continuous flow, these planktonic cells are flushed through the circuit but any disturbance to flow can cause planktonic cells to become rapidly re-distributed within a circuit. To prevent this, we build the first fluid wall that separates chemotaxing bacteria directly on the microscope so that flows are not interrupted by having to move the circuit back onto the printer. In this case the stylus is fixed to the microscope condenser, and circuits are reconfigured as the motorised stage moves the dish relative to the stationary stylus. Then, new fluid walls are built as before in seconds with a precision largely determined by that of the stage (typically in the micrometre range). Uniquely, then, this allows chemotaxing cells to be isolated from others without interrupting flows or imaging.

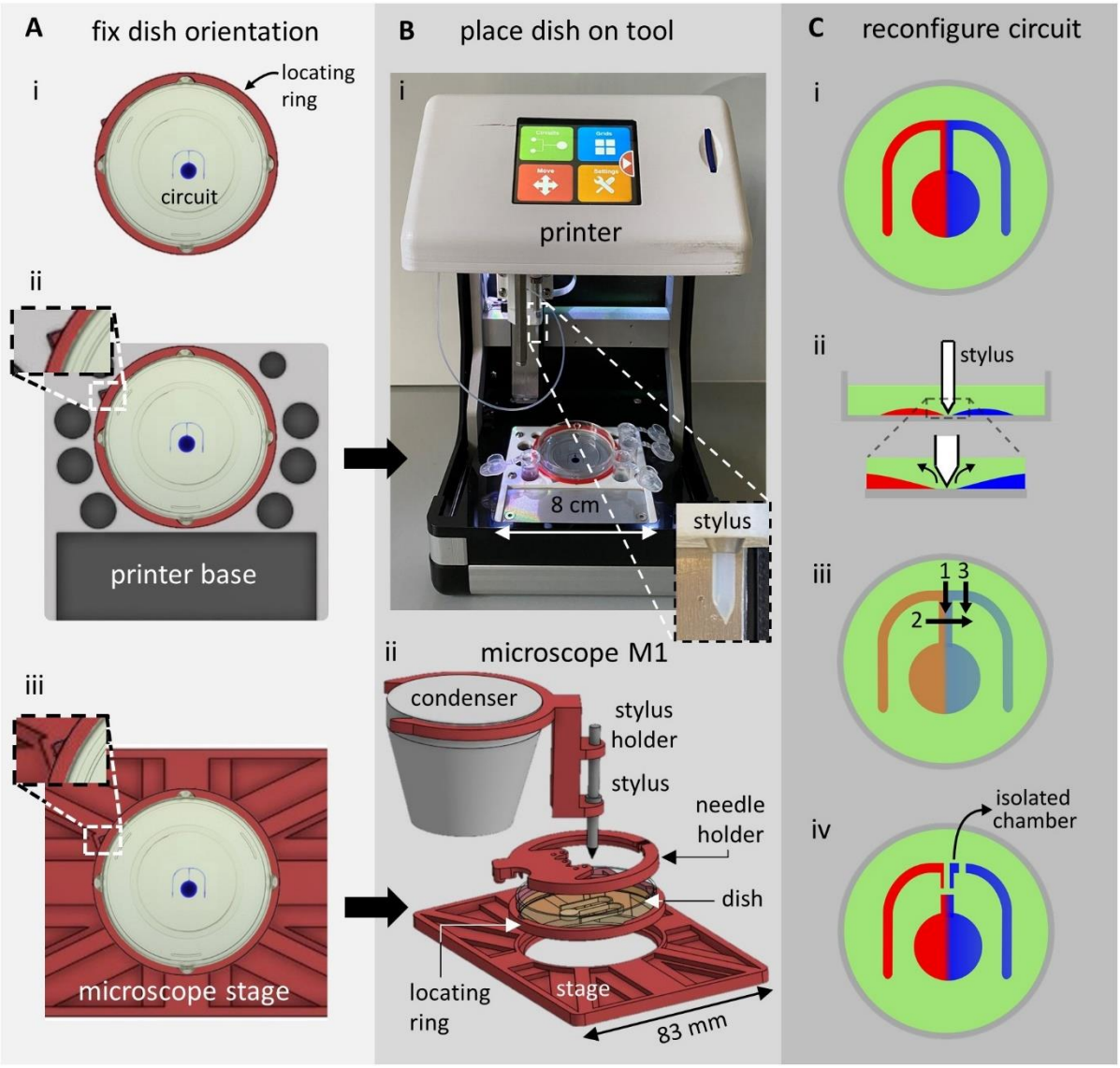


Fig. 2. Reconfiguring microfluidic environments on a printer or microscope. (A) Fixing orientation of dish. **(i)** A 3D-printed locating ring (red) with a triangular protrusion (top left). The ring fits around a 6 cm dish containing a circuit (+ blue dye for visualization). **(ii)** The stage of the printer bears a complementary triangular indentation that orients the dish. **(iii)** The ring also fits into an adaptor for the microscope stage (red, top-down view). **(B)** Reconfiguration tools. **(i)** Printer with dish in red locating ring. Inset: close-up of PTFE stylus used to reconfigure circuit. **(ii)** Microscope condenser with exploded view of 3D-printed attachments (red; see **Supplementary SVG files** for CAD models). **(C)** Cartoons illustrating circuit reconfiguration. **(i)** Circuit before reconfiguration (red/blue: media -/+ chemoattractant). **(ii)** The stylus is lowered on to the surface of the dish; it forces media aside and brings FC40 down to wet the dish where it

remains stuck to the bottom. **(iii)** The stylus builds new fluid walls along paths 1-3. **(iv)** This results in 3 new fluid walls that completely isolate part of the circuit from the rest.

Recovering macrophages chemotaxing towards C5a

Complement component 5a (C5a) is a protein that plays an important role in the innate immune response and acts as a chemoattractant that draws macrophages to infection sites [18]. As a proof-of-principle of the first workflow outlined above where circuits are reconfigured on the printer, a population of murine bone-marrow-derived macrophages (BMDMs) are exposed to gradients of C5a (**Fig. 3Ai**; exact circuit dimensions shown in **Fig. S2A**), and the migrating sub-population isolated and extracted.

Establishing the gradient

After printing the circuit and seeding cells, input and output needles are inserted into appropriate positions in the circuit using a 3D-printed holder (**Fig. S1A,B**), and input (i.e., medium ± 10 nM C5a) and output flows established (**Fig. 3Bi**). Previous assays using differently-coloured dyes confirm that diffusion creates a stable concentration gradient across the width of the central conduit (left-hand inset in **Fig. 3Bi**; maximum gradient width is ~53 μm – **Materials and Methods**).

Identifying the chemotaxing population

The dish is now placed in a commercially-available imaging system – an 'IncuCyte' ZOOM – that fits in a CO_2 incubator; the microscope objective can be programmed to collect images as it moves under stationary dishes. Note, however, that our approach is easily extended (using appropriate 3D-printed adaptors) to most automated microscopes suitable

for live-cell imaging of mammalian cells. In our case, cells in the IncuCyte are imaged for 28 h at 3 frames/h. Real-time observation reveals that many BMDMs chemotax towards C5a, as expected. **Figure 3Bii** illustrates one frame from **Movie S1**. Macrophages – initially randomly distributed throughout the conduit – accumulate roughly along the centre-line of the C5a gradient. To confirm directed movement, we analysed trajectories of 841 individual cells (using custom particle-tracking software, **Materials and Methods**). Where the C5a concentration gradient is steepest (close to the centre-line), there are many more trajectories towards C5a compared to those away from the chemoattractant (shown in blue and orange, respectively, in **Fig. 3Di**), and we confirm this bias in a rose plot (**Fig. 3Dii**). Results are consistent with known behaviours: BMDMs detect concentrations of 10 nM C5a and chemotax towards the attractant [8].

Isolating the chemotaxing sub-population

Migrating BMDMs are now isolated by constructing new fluid walls around them (**Fig 3C**). Flow through the circuit is halted and the dish returned to the printer where the stylus builds a new separating fluid wall ("wall 1" in **Fig. 3Ci**) down the centre-line of the conduit (**Fig. 3Cii**). Subsequently two additional walls are built across the width of the central conduit ("wall 2" and "3" in **Fig. 3Ci**) to create an entirely isolated fluid chamber containing ~500 nL of medium plus a sub-population of cells that had migrated towards C5a, in addition to any non-responders initially present.

Extracting the chemotaxing sub-population

The printer now infuses ethylenediaminetetraacetic acid (EDTA) – a calcium chelator that detaches macrophages from surfaces [19] – into the chamber, and after 10 min, the

aqueous phase containing now-suspended cells is withdrawn (along with a small amount of surrounding FC40) and manually plated into conventional tissue-culture dishes. Using this approach, ~87% migrating cells (as defined in **Fig. S3**) are recovered and plated, of which ~80% remain viable after 24 h. This value is equivalent to those achieved with conventional cultures of these fragile primary cells [19]. These results confirm that BMDMs undergo chemotaxis towards C5a within fluid-walled microfluidic circuits and that a sub-population rich in migrating cells can be isolated from the general cell population with excellent viability. Where desired, this approach could easily be extended to carry out detailed downstream molecular analysis of chemotaxing and non-chemotaxing populations in order to connect phenotypical differences to differences in gene expression (**Fig. 1Av**).

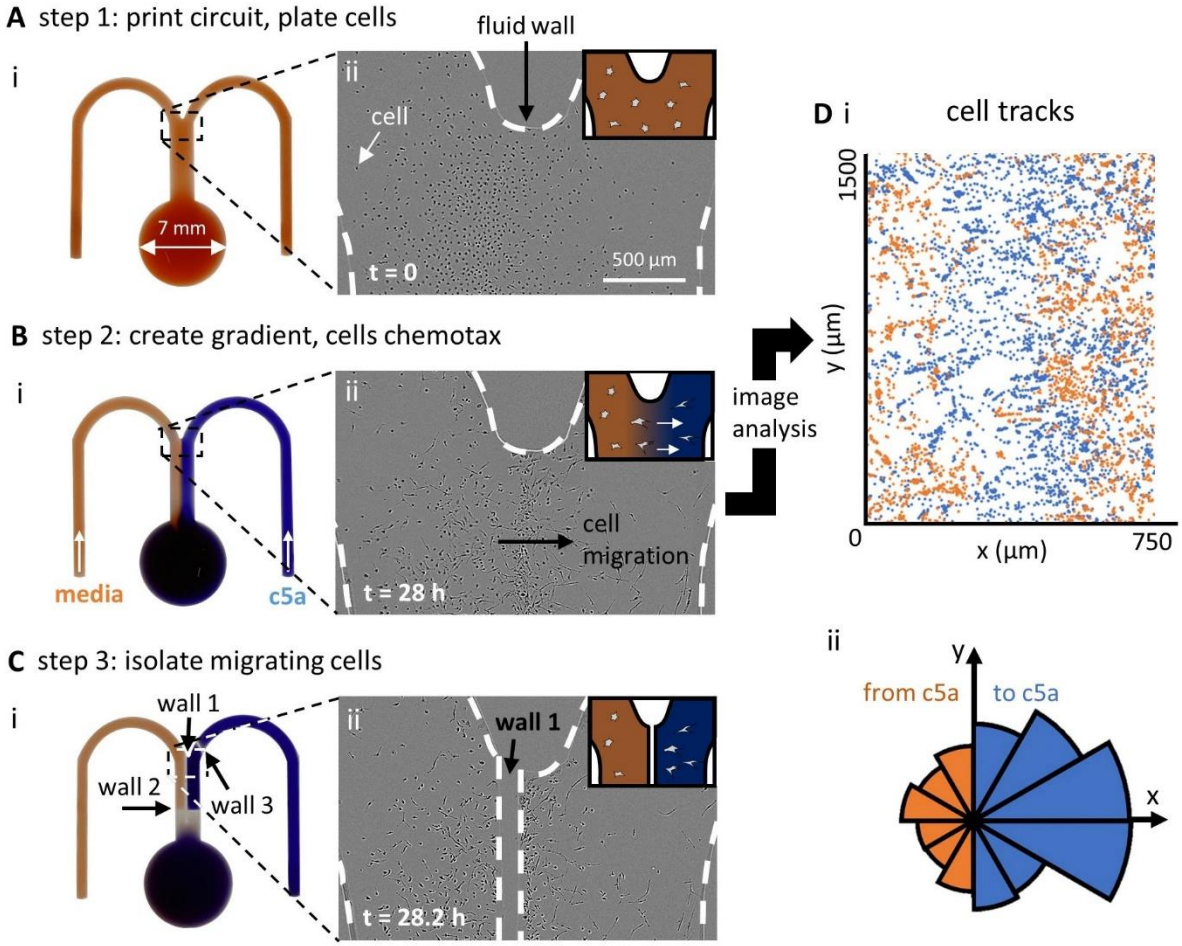


Fig. 3. Steps in building fluid walls around chemotaxing macrophages (BMDMs). (A) Step 1 (after printing a circuit and plating BMDMs; *t* = 0 h). **(i)** Image of 'm'-shaped circuit (with red dye to aid visualisation; dish invisible). **(ii)** Phase-contrast micrograph of area indicated in (A,i). Cells (dark dots) are confined by medium:FC40 walls (dashed lines). Inset: cartoon showing cells in media (red). **(B)** Step 2 (after establishing a chemoattractant gradient between laminar streams of media ± 10 nM C5a which flow down the conduit at 1 µL/min; *t* = 28 h). **(i)** Image of circuit. As before, red and blue dyes represent media and C5a. **(ii)** A micrograph of area in (B,i) taken from a movie in which many cells are seen to chemotax towards C5a on the right. Inset: cartoon showing cells chemotaxing towards C5a (blue). **(C)** Step 3 (after building three new fluid walls around chemotaxing cells on the printer; *t* = 28.2 h). **(i)** Image of circuit. New walls again faintly visible (positions also indicated by dashed white lines). Pumps are stopped before building new walls, and below wall 2 there has been time for diffusion to dissipate the dye gradient across the conduit. **(ii)** Micrograph of area in (C,i) showing wall 1 built down the conduit separating chemotaxing from non-chemotaxing cells. **(D)** Image analysis of cells seen in movie. **(i)** Trajectories of individual cells in (bii) (blue – towards C5a, orange – away from C5a). **(ii)** Rose plot indicating binned probability-density distribution of directed cell movement (total number of trajectories n = 841, three experimental repeats). Movement is strongly biased towards C5a.

Recovering *P. aeruginosa* cells migrating towards antibiotics

P. aeruginosa can grow free in solution and as a surface-attached bacterial biofilm. Early during the formation of a biofilm, surface-attached bacteria move by twitching motility using type-IV-pili to drag themselves across the substrate at speeds of ~0.2-0.5 µm/min [20], [21]. Twitching bacteria undergo chemotaxis towards (and not away from) lethally-high concentrations of antibiotics [10], a counter-intuitive behaviour that is currently under intensive investigation. However, several factors make studying bacterial chemotaxis towards antibiotics challenging. First, a population of *P. aeruginosa* cells frequently detach during the

earliest stages of biofilm development to become planktonic [15], where they use flagella to swim four orders of magnitude more quickly than surface-attached cells (at ~2,400 µm/min, [22]); consequently, they can traverse the microfluidic channels described above in seconds. Second, the steep gradients required to detect chemotaxis in our circuits break down within minutes once flows cease. This would expose cells to rapid changes in antibiotic concentration that can harm them and cause them to detach from the surface. Consequently, the chemotaxing sub-population in a biofilm is best isolated without perturbing flow. Note that flow velocity in the laminar streams we use is ~21,600 µm/min, so any cells becoming planktonic are rapidly flushed away (as the chemotactic gradient remains). Therefore, we designed a workflow to isolate chemotaxing cells under flow; it involves adding 3D-printed adaptors to a standard inverted microscope with a motorised stage to enable it to build new fluid walls.

Imaging bacteria within antibiotic gradients

Here, we use a smaller 'm'-shaped circuit as bacteria are an order of magnitude smaller than macrophages (**Fig. 4Ai**; **Fig. S2B**). *P. aeruginosa* cells are inoculated into the central conduit, where they attach to the dish and develop into an early-stage biofilm (**Fig. 4Aii**). Cells are seeded as a 1:1 co-culture of wild-type (WT) and mutant cells (*ΔpilG*) – the WT expresses the yellow fluorescent protein (YFP), and the mutant acts as an internal chemotaxis-null control as it lacks the *pilG* gene required for biased chemotaxis [21]. After mounting the dish on the microscope stage, media ± ciprofloxacin (an antibiotic often used clinically to treat *P. aeruginosa* infections) is infused into the circuit, and – as before – diffusion creates a stable gradient of attractant across the central conduit (maximum gradient width ~67 µm; **Materials and Methods**).

For these experiments, one input contains ciprofloxacin at 100 times the minimum inhibitory concentration (MIC, 10 μg/ml) required to inhibit cell growth [10]. Consequently, all cells initially exposed to high ciprofloxacin concentrations on the right of the central conduit either fail to grow and/or are lost from the substrate (**Fig. 4Aiii**) to be rapidly flushed away to the sink. As expected, some surface-attached cells on the left begin to migrate up the ciprofloxacin gradient (**Fig. 4Aiv**). To follow this migration, we image conduits for up to 36 h post-inoculation at 1 frame/min. After ~20 h, migrating WT cells accumulate in regions containing high ciprofloxacin concentrations (**Fig. 4B**); in contrast, mutant ones do not. Analysis of individual trajectories of >1,000 individual WT cells (see **Materials and Methods**) shows that in the taxis zone, there were 2-fold more trajectories moving towards the antibiotic compared to those moving away from it (shown in blue and orange, respectively, in **Fig. 4Di**) – a bias confirmed in a rose plot (**Fig. 4Dii**). We also use trajectories to detect when cells abruptly reverse direction and change their direction by ~180^{o}. It has been shown previously that these cells bias motility by reversing more frequently when moving away from, rather than towards, chemoattractants [21], [23], and this is confirmed here (**Fig. 4Diii**).

Reconfiguring circuits on a microscope to isolate migrating cells

After ~20 h, many cells have undergone chemotaxis towards ciprofloxacin and so we next isolate this migrating sub-population free from those establishing a biofilm in antibiotic-free regions of the circuit. As we have seen, this can only be achieved as flow continues. Therefore, we use 3D-printed adaptors to attach a PTFE stylus to the microscope condenser (**Fig. 2Bii**), and then use the motorised stage on the microscope to move the stylus relative to the dish – and so build one new fluid wall down the length of the central conduit separating

the bulk of the migrating population from the remainder (**Fig. 4C, Fig. S4**; **Materials and Methods**)**.** Once this wall is built, flows through the circuit are stopped and two additional walls were built across the width of the central conduit above and below the taxis zone to completely isolate cells that have undergone chemotaxis in a chamber containing ~100 nL (**Fig. S4C**).

Extracting chemotaxing cells and assessing their viability

Although migrating cells remain motile as they chemotax into high antibiotic concentrations, it is unclear whether they retain long-term viability and develop antibiotic resistance. To assess long-term viability, circuits are transferred back to the printer and the contents of the isolation chamber extracted (**Fig. S5A**). This fluid (containing any planktonic cells) is then plated on agar plates containing antibiotic-free growth medium to monitor colony growth. The viability of cells remaining within the isolation chamber is also monitored continuously. Any residual ciprofloxacin in the chamber is removed and replaced with antibiotic-free media, dishes returned to the microscope, and the entire isolation chamber imaged for at least 36 h to detect any cell growth and division. Neither cells extracted from the isolation chamber, nor those remaining behind in it, retained long-term viability. Why then does *P. aeruginosa* move towards antibiotics? It appears that chemotaxis towards antibiotics may be driven by an evolved response of surface-attached *P. aeruginosa* to move towards toxins produced by neighbouring competitors in an attempted counter-attack [10]. However, in the case of antibiotic gradients, this counter-attack proves futile, and the attackers die.

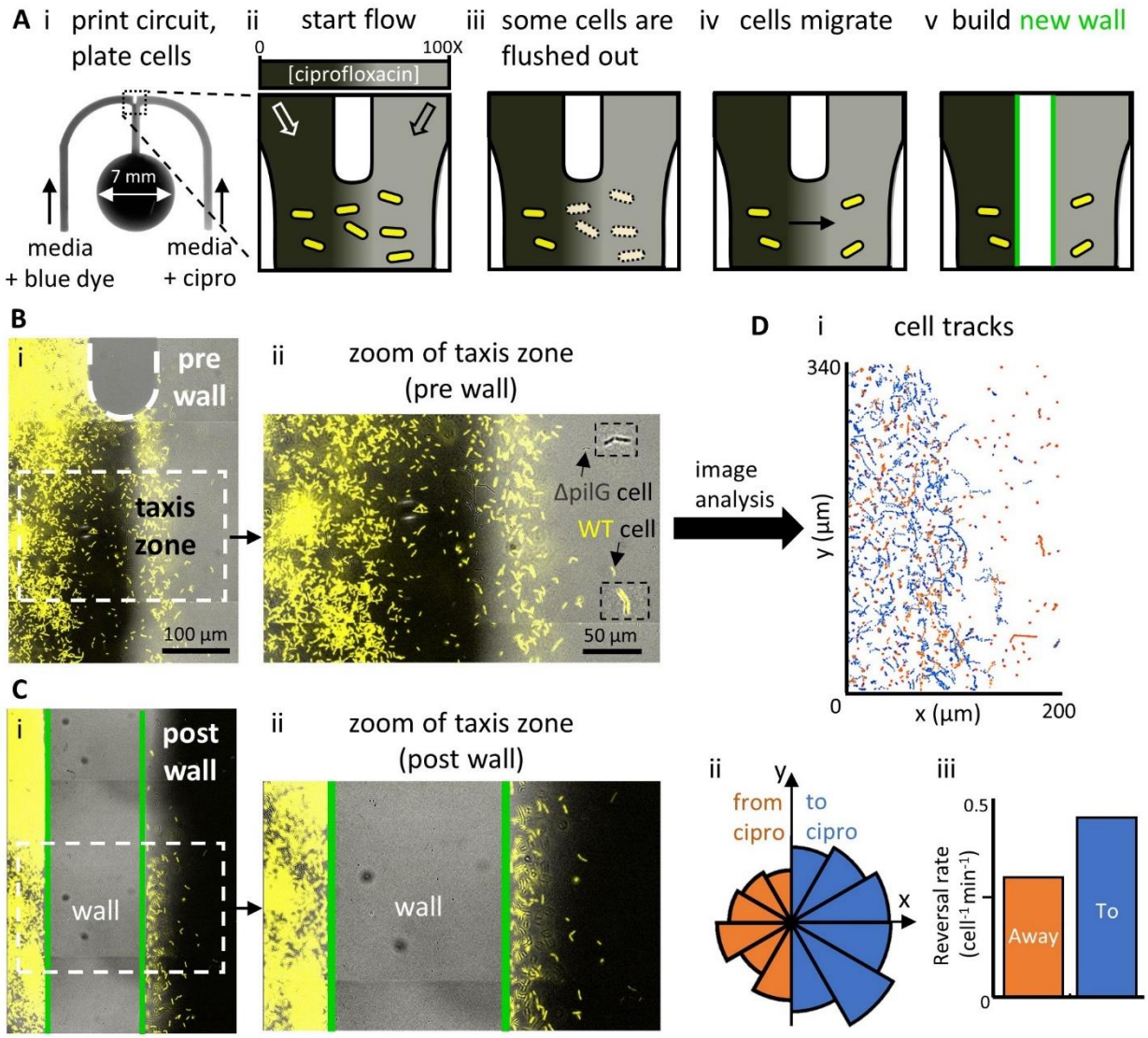


Fig. 4. Building fluid walls on a microscope to isolate bacteria chemotaxing towards an antibiotic. (A) Overview. **(i)** Micrograph of 'm'-shaped circuit. A 1:1 co-culture of YFP-labelled WT and unlabelled *ΔpilG* mutant (chemotaxis-null) *P. aeruginosa* are seeded in the conduit, and laminar streams of media + blue dye (dark grey) and media + ciprofloxacin (cipro, 10 µg/mL = 100X MIC; light grey) flow over them. **(ii-v)** Cartoons giving overview (grey scale reflects antibiotic concentration, only WT bacteria shown). After plating, WT bacteria grow in the conduit. Flow then establishes a concentration gradient by diffusion of antibiotic across the conduit; cells exposed to high concentrations on the right die and are washed away. Some bacteria then chemotax from the antibiotic-free region into the high concentration of ciprofloxacin. A new wall is then built between chemotaxing and non-responsive cells. **(B)** Micrographs of the top of the

central conduit before building a new isolating wall. **(i)** Merge of fluorescence and phase contrast images showing cells in a ciprofloxacin gradient (only fluorescent WT cells visible at this magnification). Most cells on the right have been killed and washed away, and some on the left are chemotaxing towards the antibiotic. **(ii)** Zoom of cells in taxis zone. The area is rich in yellow-fluorescing WT cells, with some phase-dark mutant cells (arrow and insets mark both types of cell). **(C)** Micrographs after building the wall. **(i)** Merge of fluorescence and phase contrast images showing cells (only WT visible) and the new wall (cells within it are removed during building). The chamber on the right now contains ciprofloxacin at 3 times the MIC plus blue dye (dark grey, see **Materials and Methods**). **(ii)** Zoom of taxis zone and new wall. **(D)** Image analysis of cells in the taxis zone prior to building new wall. **(i)** Trajectories of individual cells (blue/orange tracks – to/from antibiotic. **(ii)** Rose plot indicating binned probability density distribution of directed movement (total number of trajectories n = 1470; 3 experimental repeats). Movement is biased to the right. **(ii)** Cells bias motility towards antibiotic by reversing direction more frequently when moving away from the antibiotic.

Discussion

We report two general methods for isolating desired sub-populations of cells from within microfluidic circuits in which the aqueous phase is confined by fluid walls (**Fig. 1**) and exemplify them by isolating chemotaxing macrophages or bacteria free of their non-responding counterparts. In the first approach, circuits are fabricated, manipulated, and reconfigured on a custom-built three-way traverse. As these operations are performed blindly on the traverse, we design 3D-printed components that fit on the condenser unit of conventional inverted microscopes to transform them into micromanipulators capable of circuit reconfiguration (**Fig. 2**). This allows specific sub-populations of cells to be isolated with high precision using real-time, microscopic imaging as a guide. Our approach also allows flow through circuits to continue uninterrupted until immediately prior to circuit manipulation. Using the traverse, we first isolate macrophages chemotaxing towards C5a (**Fig. 3**). We then use the 3D-printed adaptors to target and isolate bacteria migrating towards antibiotic in real-time on a microscope (**Fig. 4**). Note that we also isolated macrophages by converting another standard inverted microscope in this way (**Fig. S8**).

Uniquely, this second approach allows isolation of the desired sub-population as flow and imaging continue. In both cases, the isolated sub-population can be extracted from the circuit and analysed using any desired technique. For example, RNA sequencing could be applied to identify which transcripts increase in number in the chemotactic sub-population. Moreover, as fluid walls can be built around single cells using this [4] and related approaches [12], single-cell transcriptomics could even be applied. Hence, this method allows behavioural phenotype to be linked to genotype. In summary, we hope this method will help facilitate the introduction of microfluidic techniques into biomedical labs, especially for the study of cells

living in the flowing environments that can so profoundly influence cell physiology, and which have largely remained inaccessible to modern analytical techniques.

Materials and Methods

Strains, media and culture conditions

To obtain BMDMs, bone marrow was extracted from C57BL/ 6-Tg (CD68-EGFP) 1Drg/ J (026827, the Jackson Laboratory) hind-limbs of hCD68-GFP transgenic mice bred on a C57BL/6 background, and ~50-80 million cells cultured (7 d, 37°C, 5% CO_2) in high-glucose Dulbecco's Modified Eagle's Medium (DMEM, Sigma) enriched with 10% L929-conditioned media (containing macrophage colony-stimulating factor), 10% fetal bovine serum (FBS, Sigma) and 1% penicillin plus streptomycin (P/S, Gibco). 8 mL growth media was used for the first 4 d; then, 3 mL media was removed and replaced with 5 mL fresh media. Cells were plated into circuits on day 6, and chemoattractants added on day 7.

The wild-type *P. aeruginosa* strain used throughout this study was PAO1 (Kolter collection ZK2019), expressing yellow fluorescent protein (YFP) from a constitutive promoter [21]. As an in-experiment control, we used a PAO1 strain harbouring an in-frame deletion of *PilG* (*ΔpilG*, [12]). All bacteria were grown from frozen stocks overnight in LB medium (ThermoFisher; 37°C; 250 rpm) and sub-cultured (1:30 dilution) in tryptone broth (TB, 10 g/L Bacto Tryptone; ThermoFisher) for 2.5 h (37°C; 250 rpm). Cells were then diluted in TB to an optical density (OD) at 600 nm of 0.6 before inoculation into circuits.

Imaging

BMDMs were imaged at a rate of 3 frames/h using an IncuCyte ZOOM, a commercially available live-cell imaging system (Sartorius, Gottingen, Germany). Bright-field images of *P. aeruginosa* were captured at a rate of 1 frame/min using a Zeiss Axio Observer inverted microscope with a Zeiss AxioCam MRm camera, a Zeiss Definite Focus system and a 20X Plan

Apochromat air objective. To excite the YFP fluorophore in the YFP-labelled WT control, we additionally performed epifluorescence imaging using a Zeiss HXP 120 illuminator (150 ms exposures). In all experiments, cell movement was followed in real-time and images were subsequently processed using Fiji [24] and analysed using Matlab.

Circuit design and fabrication

To study chemotaxis, we used 'm'-shaped microfluidic circuits to study both BMDMs and surface-attached *P. aeruginosa*, although the latter circuits were smaller in size (**Fig. S2**; note that BMDM cells are ~20 µm in diameter, and *P. aeruginosa* cells ~1 µm). All needles, glass syringes, and Teflon tubing were internally sterilised and washed by infusing 70% ethanol followed by sterile culture medium (either DMEM or TB), and then externally sterilised by bathing in 70% ethanol for 1 min followed by sterile medium for 1 min.

BMDM circuit

The BMDM circuit was printed using a modified, custom-made printer (iotaSciences Ltd, Oxford, UK). The three-axis traverse on the printer holds a 25G dispensing needle (Adhesive Dispensing Ltd) connected by PTFE tubing (Cole-Parmer) to a 250 µL glass syringe (Hamilton) controlled by a syringe pump (iotaSciences Ltd). The dispensing needle was brought 300 µm above the surface of the dish and then infused (10 µL/min) DMEM + 10% FBS + 10% L929 + 1% P/S + 2% fibronectin as it drew the circuit [3]. Once completed the circuit was overlaid with 2 mL FC40 (iotaSciences Ltd) to prevent evaporation. Circuits were printed on both 60 mm tissue culture-treated dishes (Corning, 430166), and 60 mm suspension dishes (Corning, 430589). As BMDMs are extremely adherent, suspension dishes were used when cells were to be extracted (**Fig. S3**).

P. aeruginosa circuit

The bacterial circuit was printed on the surface of untreated 50 mm glass-bottomed dishes (MatTek; the diameter of the glass bottom is 30 mm) as described above except that the needle was lowered to within 200 µm of the glass surface, and then moved across the dish as it infused (10 µL/min) DMEM + 10% FBS. After printing, circuits were immediately overlaid with 2 mL FC40. A thin and straight FC40 wall (length ~1 mm, width ~100 µm) was then built at the junction where the two-inlet arms merge into the central conduit (**Fig. S2B**), to allow incoming streams to meet roughly parallel to one another. This wall was made by jetting (**Fig. S6**; [12]). Briefly, the dispensing needle was used to generate a rapid jet of FC40. When this jet is targeted onto an existing circuit, the FC40 jet forces aside the aqueous phase making up the circuit, analogous to the PTFE stylus physically pushing media aside. The FC40 subsequently remains stuck to the dish (held by interfacial forces). We therefore jetted FC40 (6.5 µL/s) through a 70 µm diameter needle (Oxford Lasers) positioned 0.5 mm above the aqueous circuit as the needle traversed in a straight line (1000 mm/min) to create the ~100 µm wide dividing wall.

Exposing BMDMs to a gradient of C5a

Following circuit fabrication, the sink was sealed off from the central conduit by building a new wall across the bottom-end of the conduit with a PTFE stylus. This allowed cells to be added directly within the conduit, without flowing into the sink due to differences in pressure across these two reservoirs – the larger size of the sink (and hence radius of curvature) results in a lower Laplace pressure [3] and therefore any solution added to the conduit will flow directly into the sink down the resulting pressure gradient. Note that this

was not necessary when carrying out experiments with *P. aeruginosa* because we were able to use a much higher inoculum density allowing many cells to attach before drifting into the sink.

BMDMs (5 µL with 1000 cells/µL) were infused into the conduit, and the dish incubated overnight to allow cell attachment. Using a hydrophilic stainless-steel 25 G needle (identical to the one used to print circuits), the sink was reconnected with the conduit by manually dragging the needle between the two interfaces, allowing fluid walls to merge back with one another. Three syringes (Hamilton) were then loaded onto syringe pumps (PhD Ultra, Harvard Apparatus): one 5 mL glass syringe filled with DMEM + 10% FBS + 10% L929 + 1% P/S, another identical one with the same media + 10 nM C5a (recombinant mouse complement component 5a, R&D Systems), and a third 10 mL glass syringe with 1 mL growth media. The 5 mL syringes were mounted on the same syringe pump, while the 10 mL syringe was fitted on a separate one. All three syringes were connected to 25 G needles (Adhesive Dispensing Ltd) via PTFE tubing (1 m). A 3D-printed needle holder that attaches to the outside edge of the dish then aids manual placement of needles in the circuit (**Fig. S7**). To ensure needles were inserted 100 µm above the glass surface, the holder was first placed on a separate dish containing a glass coverslip (Menzel-Glaser #1 thickness) glued to the bottom. Needles were then lowered through the holder until they came into contact with the coverslip, at which point the needles were bent over the holder to ensure they remained at the same height throughout an experiment (**Fig. S7B,iii**). With needles in the holder at an appropriate height, the holder was transferred to the dish containing the circuit. The 5 mL syringes ± chemoattractant were connected to the left and right arms of the circuit respectively, and the 10 mL syringe to the sink. The circuit was then overlaid with an

additional 4 mL of FC40 and placed in the IncuCyte (inside an incubator at 37°C, 5% CO_2). The 5 mL syringes were set to infuse at 0.5 µL/min, while the 10 mL syringe was set to extract at 1 µL/min.

Exposing *P. aeruginosa* to a ciprofloxacin gradient

After fabrication, circuits were infused (0.5 µL/min) with 1.5 µL TB through each of the two inlet arms to flush out the DMEM + FBS used during fabrication. Flushed media flowed into the sink at the end of the central conduit and was subsequently removed. *P. aeruginosa* cells (3 µL with OD at 600 nm of 0.6) were then infused (0.4 µL/min) into one arm of the circuit upstream of the junction, and the circuit was left for 10 min to allow cells to attach to the glass surface.

Two 500 µL glass syringes (Hamilton) were then used to set up the antibiotic gradient – one containing TB plus Chicago Sky Blue dye (0.05 mg/mL) to enable visualisation of the (reverse) concentration gradient, the other with TB plus 10 µg/mL ciprofloxacin (corresponding to 100 times the MIC). This dye does not influence cell motility in surface-attached *P. aeruginosa* cells [21]. A third plastic 10 mL syringe (Becton Dickinson Plastipak) was loaded with 1 mL TB plus 10 µg/mL ciprofloxacin (corresponding to 10 times the MIC) and a fourth plastic 1 mL syringe (Becton Dickinson Plastipak) with 1 mL TB plus 0.3 µg/mL ciprofloxacin (corresponding to 3 times the MIC) and Chicago Sky Blue dye (0.05 mg/mL). Each syringe was fitted into an individual syringe pump (PhD Ultra, Harvard Apparatus), and connected to a 25G needle (Adhesive Dispensing Ltd) via PTFE tubing (1 m). The four needles were then placed into a needle holder (**Fig. S7**) and set to the appropriate height using the same 'zeroing' technique as before. The holder was transferred to the dish containing the

circuit, and needles lowered into the circuit: the needle connected to the glass syringe plus TB was lowered into the left arm, the second connected to the glass syringe plus antibiotic was lowered into the right arm, the third connected to the 10 mL plastic syringe was lowered into the sink, and the fourth connected to the 1 mL plastic syringe was lowered into the right arm upstream of the second inserted needle (**Fig. S7A**). A further 4 mL FC40 was then overlaid on the circuit to prevent any evaporation during the experiment.

To generate a concentration gradient of ciprofloxacin, TB plus 10 µg/mL ciprofloxacin was infused into one inlet arm, and TB plus dye into the other (0.1 µL/min each). The two fluids then joined as laminar streams after the dividing wall and flowed through the central conduit into the sink. Diffusion between streams then generated two concentration gradients across the conduit width; one due to antibiotic, the other due to dye. Visual observation of the dye gradient allowed us to be sure that flows were stable and laminar, and that diffusion gradients were established. Fluid was also simultaneously withdrawn at an equivalent flow rate (0.2 µL/min) through the needle in the sink into the 10 mL plastic syringe. After ~12 h, rates of infusion and withdrawal were halved to widen the ciprofloxacin gradient and so increase the number of cells that were exposed to the antibiotic gradient. All antibiotic-taxis experiments were carried out at 22°C.

Determining maximum gradient widths

Fluid walls morph in response to pressure changes and in a straight conduit, the height decreases with distance from the point of highest pressure (i.e., where the needle infuses media). It was recently shown that conduit heights and flow velocities in fluid-walled circuits can accurately be predicted from a simple semi-analytical model [25]. Using this equation, we

determined the average maximum height ($h_{max,avg}$) and particle velocity ($u_{max,avg}$) for each conduit in this study in order to estimate the average amount of time a particle spends in the conduit as $t_{avg} = \frac{L_{conduit}}{u_{max,avg}}$, where $L_{conduit}$ corresponds to the length of the conduit observed. We then used this time to calculate the maximum diffusion distance of a particle ($x_{particle}$) using Einstein's relation $x_{particle} = \sqrt{2D_{particle}t_{avg}}$, where $D_{particle}$ is the particle diffusion coefficient.

We first determined the diffusion coefficient of C5a from its predicted molecular mass of 9 kDa; using the Stokes-Einstein equation for diffusion, this yielded $D_{c5a} = 1.8 \times 10^{-10}$ m^2/s. Hence, for the BMDM circuit, $Q = 1$ µL/min, $h_{max,avg} \approx 100$ µm, $u_{max,avg} \approx 10{,}800$ µm/min, $L_{conduit} = 3$ mm, therefore the maximum gradient width obtained within the conduit is $x_{c5a} \approx 77$ µm. For the *P. aeruginosa* circuit, $Q = 0.2$ µL/min, $h_{max,avg} \approx 40$ µm, $u_{max,avg} \approx 21{,}600$ µm/min, $L_{conduit} = 2$ mm, $D_{cipro} = 4 \times 10^{-10}$ m^2/s [26], therefore, the maximum gradient width obtained within the conduit is $x_{cipro} \approx 67$ µm. As $t_{avg} \propto 1/Q$, if conduit dimensions don't change, then halving the flow rate would increase the gradient by a factor of $\sqrt{2}$, and so for the *P. aeruginosa* circuit $x_{cipro} \approx 95$ µm. However, since lowering the flow rate also decreases the height of the conduit (whereas the width stays unchanged due to the pinning lines), then 67 µm $< x_{cipro} <$ 95 µm.

3D-printed adaptors for easy manipulation of circuits on and off the microscope

The workflow requires transfer of circuits between microscope stage and printer. To ensure circuits retain the same orientation on both platforms, dishes were fitted into a carrier bearing a single triangular protrusion (positioned 63° counter-clockwise from the top). This

carrier was designed to fit in a fixed orientation into holders built into both the printer and microscope stages that bore complementary triangular indents (**Fig. 2**). Both carrier and holder were designed using Onshape (Boston, MA) and fabricated using a Flashforge Finder 3D-printer (Zhejiang, China). Carriers were designed for both Corning and MatTek dishes and can be easily adapted to fit any standard dish.

Calibrating a circuit before reconfiguration on a microscope

We designed a simple adaptor to fit a PTFE stylus onto the condenser of conventional microscopes, allowing us to reshape circuits without interrupting flows (**Fig. 2**). The adaptor was designed using Onshape and fabricated using a Flashforge Finder 3D-printer (**Supplementary SVG files**). To reconfigure circuits, the stylus was first held to one side of the condenser turret to not interfere with imaging. We then calculated the distance between the centre of the objective lens (the centre of the field of view) and the position of the stylus. To perform this calibration, we designed an 'L'-shaped conduit placed above the main circuit (**Fig. S4A,B**). The stylus was then lowered onto the surface of the dish in the gap between both arms of this 'L' and the coordinates of this position (p_1) was recorded. Next, we moved the microscope stage vertically, moving the stylus perpendicularly through the horizontal arm of the 'L' ('path 1' in **Fig. S4B**). After returning the microscope stage to p_1, we moved the stage horizontally, moving the stylus perpendicularly through the vertical arm of the 'L' ('path 2' in **Fig. S4B**). This created both a horizontal and vertical wall through the arms of the 'L'-shaped conduit (**Fig. S4B**). The offset between the coordinates of p_1 and the centre of these vertical and horizontal walls corresponded to the *x*- and *y*-offsets respectively between the objective lens (p_2) and the attached stylus. Using these offsets then allowed us to position the stylus precisely within any observable region of the dish. The precision with which any new walls

were built was thus determined by the movement resolution of the microscope stage (typically in the micrometre range) and the width of the stylus (typically tens of micrometres), although this precision can be slightly reduced by play in the ring that holds the stylus.

Isolating and extracting chemotaxing BMDMs both on and off the microscope

After ~28 h in the circuit, BMDMs began migrating towards higher C5a concentrations, creating a region of high cell density (**Fig. 3, Fig. S3, Fig. S8**); the first fluid wall was built to isolate this band from cells remaining in low C5a concentrations. Since BMDMs are so adherent [19], flows can be stopped prior to reconfiguring the circuit without risking cross-contamination from detaching cells. The reconfiguration was then performed by placing the dish on the printer which builds the new walls. Wall coordinates were determined by analysing cell trajectories, and the stylus was washed after building each wall with 70% ethanol to prevent cross-contamination (**Fig. 3, Fig. S3**). Additionally, circuits were also reconfigured on the stage of an IX53 inverted microscope (Olympus) using a modified version of the adapter holding the PTFE stylus on the condenser. The stylus was positioned directly above the objective lens and the circuit was dragged past it in real time by moving the stage of the microscope as described previously (**Fig. S8**).

Automated retrieval of isolated BMDMs

The circuit was returned to the printer to extract the small volume remaining in the isolation chamber. First, the chamber was washed twice by sequentially adding and removing 0.5 µL PBS (5 µL/min), followed by 1 µL 10 mM EDTA (a metal chelator that reduces adhesion of integrins [19]) in PBS (5 µL/min), and then incubating for 10 min at 37°C. The chamber was then gently but firmly tapped from below the dish using a pen to ensure that most cells were

dislodged (confirmed visually on the microscope). To extract dislodged cells, a volume of 1.5 µL was withdrawn (5 µL/min) from the chamber using an extracting needle that had been pre-loaded with 20 µL cell media to ensure that withdrawn cells were immediately exposed to nutrient-rich media (**Fig. S3**). The needle then dispensed (100 µL/min) 5 µL of its contents into an Eppendorf tube containing 95 µL cell media, the contents of which were then transferred to a 35 mm TC-treated dish (Corning, 430165) and incubated for 24 h to assess cell viability.

Assessing BMDM viability post-extraction

To assess viability of extracted BMDMs, we counted the number of cells contained within the isolation chamber immediately after building the surrounding walls and compared this to the number of cells extracted and transferred to the new dish. We defined a specific region of interest including only the population of chemotaxing cells (ROI – dashed outline in **Fig. S3B-D**) from which we extracted ~87% of cells. In total, ~80% of these extracted cells were viable (defined as cells re-attaching to the surface of the dish; **Fig. S3F**).

Isolating and extracting migrating *P. aeruginosa* cells

We prepared circuits for reconfiguration by additionally infusing (0.05 µL/min) TB plus ciprofloxacin at 3 times the MIC through the same circuit arm through which we infuse TB plus ciprofloxacin at 10 times the MIC. This temporarily doubles the flow rate through this circuit arm, which shifts the gradient towards the antibiotic-free side. After obtaining visual confirmation of this shift by observing a change in the position of the dye gradient (~30 s), infusion through the syringes containing antibiotic-free TB and the syringe containing TB plus ciprofloxacin at 100 times the MIC was paused in order to fill the conduit with ciprofloxacin at 3 times the MIC. Lowering the ciprofloxacin concentration in this way ensured that after

circuit reconfiguration, any cells migrating towards high ciprofloxacin concentrations were not exposed to a sudden step-increase in ciprofloxacin concentration to 100 times the MIC.

During circuit reconfiguration, we first built a fluid wall along the length of the central conduit to isolate specific sub-populations of migrating bacteria from the high density of non-migrating cells present in antibiotic-free regions (**Fig. 4C**). After building this first wall, we continued to infuse TB plus ciprofloxacin at 3 times the MIC for 5 min to wash away any antibiotic-naïve planktonic cells that could have been inadvertently forced across from antibiotic-free regions side during circuit reconfiguration. Flow was then halted and two additional walls were built across the width of the central conduit to completely seal off an isolated fluid chamber containing migrating bacteria (**Fig. S4C**). Before building each wall, the stylus was raised and sterilised with 70% ethanol to avoid contamination from cells it may have contacted previously.

Extracting planktonic P. aeruginosa from the isolation chamber

Isolated bacteria remained in fluid chambers containing ciprofloxacin at 3 times the MIC for 2 h, an antibiotic treatment that kills 99.99% of antibiotic-naïve cells [12]. Cells were monitored by imaging (0.1 frame/min) and whilst most cells remained surface-attached, some detached and were lost from the field of view. We therefore analysed the viability of both surface-attached and planktonic populations. We first analysed the planktonic fraction by extracting chamber contents and plating them onto antibiotic-free LB agar plates. To this end, culture dishes were returned to the printer, and an extracting needle was pre-loaded with 50 µL TB media plus Chicago Sky Blue dye (0.05 g/mL); this ensured that withdrawn cells were immediately exposed to a nutrient-rich environment, whilst the blue dye allowed visual

monitoring of the exchange of nanolitre volumes in the chamber. The needle was lowered to within 100 µm of the dish surface, and 1 µL was withdrawn (2 µL/min). This volume exceeded the total in the chamber, so some FC40 was also withdrawn. The needle then ejected (100 µL/min) 5 µL into an Eppendorf tube containing 95 µL LB media. The contents of the Eppendorf tube were then spread on LB agar plates, incubated (92 h, 37°C) and colony growth monitored.

Assaying viability of surface-attached P. aeruginosa

To analyse the viability of cells remaining attached to the surface, the chamber (still covered in a thin layer of TB overlaid with FC40) was washed five times with TB media plus dye to dilute the antibiotic to a negligible level. The contents of the chamber during each wash were also recovered in separate Eppendorf tubes containing 95 µL LB media, and later plated to monitor colony growth. Each wash involved infusing (0.1 µL/min) 0.1 µL TB media plus dye into the chamber and removing 1 µL from it (including some FC40). The dishes were then returned to the microscope and the bottom-surface of the entire chamber imaged for 60 h (0.1 frames/min) to monitor cell behaviour and viability. After 60 h, we infused (0.1 µL/min) 0.1 µL of exponential-phase cell suspension (diluted to an OD at 600 nm of 0.015) into the chamber to introduce ~20 viable cells. These cells grew and rapidly filled the entire chamber after ~12 h; this acted as a positive control indicating that the concentration of antibiotic remaining in the isolated area was negligible (**Fig. S5B**).

Image analysis

To quantify the motility of individual bacteria and macrophages, we tracked thousands of cells using a cell-tracking approach we developed previously [21]. Briefly, a

series of bright-field images were stabilised and the background pixel intensity normalised using the 'Image Stabiliser' and 'Normalise Local Contrast' plugins in Fiji [24]. The background was then subtracted (using 'Subtract Background,' in Fiji) and the pixel intensity inverted to generate an image series with high-pixel intensity cells on a low-pixel intensity background. These cells were then tracked using the freely-available 'Trackmate' plugin for Fiji [27]. Further analyses of the resulting trajectories including the quantification of reversal rates and cells' chemotactic bias were performed in Matlab, as previously described [21].

References

[1] R. Rusconi, M. Garren, and R. Stocker, “Microfluidics expanding the frontiers of microbial ecology,” *Annu. Rev. Biophys.*, vol. 43, pp. 65–91, 2014, doi: 10.1146/annurev-biophys-051013-022916.

[2] G. V Kaigala, R. D. Lovchik, and E. Delamarche, “Microfluidics in the ‘Open Space’ for Performing Localized Chemistry on Biological Interfaces,” *Angew. Chemie Int. Ed.*, vol. 51, no. 45, pp. 11224–11240, Nov. 2012, doi: 10.1002/anie.201201798.

[3] E. J. Walsh *et al.*, “Microfluidics with fluid walls,” *Nat. Commun.*, vol. 8, no. 1, p. 816, 2017, doi: 10.1038/s41467-017-00846-4.

[4] C. Soitu, A. Feuerborn, C. Deroy, A. A. Castrejón-Pita, P. R. Cook, and E. J. Walsh, “Raising fluid walls around living cells,” *Sci. Adv.*, vol. 5, no. 6, 2019, doi: 10.1126/sciadv.aav8002.

[5] V. E. Deneke and S. Di Talia, “Chemical waves in cell and developmental biology,” *J. Cell Biol.*, vol. 217, no. 4, pp. 1193–1204, Jan. 2018, doi: 10.1083/jcb.201701158.

[6] R. Stocker, J. R. Seymour, A. Samadani, D. E. Hunt, and M. F. Polz, “Rapid chemotactic response enables marine bacteria to exploit ephemeral microscale nutrient patches,” *Proc. Natl. Acad. Sci.*, vol. 105, no. 11, pp. 4209 LP – 4214, Mar. 2008, doi: 10.1073/pnas.0709765105.

[7] R. Rusconi and R. Stocker, “Microbes in flow,” *Curr. Opin. Microbiol.*, vol. 25, pp. 1–8, 2015, doi: https://doi.org/10.1016/j.mib.2015.03.003.

[8] L. Taylor, M. H. Brodermann, D. McCaffary, A. J. Iqbal, and D. R. Greaves, “Netrin-1 Reduces Monocyte and Macrophage Chemotaxis towards the Complement Component C5a,” *PLoS One*, vol. 11, no. 8, p. e0160685, Aug. 2016, [Online]. Available: https://doi.org/10.1371/journal.pone.0160685.

[9] A. J. Iqbal *et al.*, “A Real Time Chemotaxis Assay Unveils Unique Migratory Profiles amongst Different Primary Murine Macrophages,” *PLoS One*, vol. 8, no. 3, p. e58744, Mar. 2013, [Online]. Available: https://doi.org/10.1371/journal.pone.0058744.

[10] N. M. Oliveira *et al.*, "Bacteria perform suicidal chemotaxis towards antibiotics," *(Manuscript in Preparation)*, 2021.

[11] C. Soitu *et al.*, "Microfluidic chambers using fluid walls for cell biology," *Proc. Natl. Acad. Sci.*, 2018, doi: 10.1073/pnas.1805449115.

[12] C. Soitu, N. Stovall-Kurtz, C. Deroy, A. A. Castrejón-Pita, P. R. Cook, and E. J. Walsh, "Jet-Printing Microfluidic Devices on Demand," *Adv. Sci.*, 2020, doi: 10.1002/advs.202001854.

[13] C. Li *et al.*, "Exclusive Liquid Repellency: An Open Multi-Liquid-Phase Technology for Rare Cell Culture and Single-Cell Processing," *ACS Appl. Mater. Interfaces*, vol. 10, no. 20, pp. 17065–17070, May 2018, doi: 10.1021/acsami.8b03627.

[14] F. J. Pixley, "Macrophage Migration and Its Regulation by CSF-1," *Int. J. Cell Biol.*, vol. 2012, p. 501962, 2012, doi: 10.1155/2012/501962.

[15] M. L. Gibiansky *et al.*, "Bacteria Use Type IV Pili to Walk Upright and Detach from Surfaces," *Science (80-.).*, vol. 330, no. 6001, pp. 197 LP – 197, Oct. 2010, doi: 10.1126/science.1194238.

[16] J. B. Kaplan, "Biofilm dispersal: mechanisms, clinical implications, and potential therapeutic uses," *J. Dent. Res.*, vol. 89, no. 3, pp. 205–218, Mar. 2010, doi: 10.1177/0022034509359403.

[17] M. Berlanga and R. Guerrero, "Living together in biofilms: the microbial cell factory and its biotechnological implications," *Microb. Cell Fact.*, vol. 15, no. 1, p. 165, 2016, doi: 10.1186/s12934-016-0569-5.

[18] R. R. Kew, "The Complement System," in *Pathobiology of Human Disease*, L. M. McManus and R. N. B. T.-P. of H. D. Mitchell, Eds. San Diego: Academic Press, 2014, pp. 231–243.

[19] S. Chen, E. C. So, S. E. Strome, and X. Zhang, "Impact of Detachment Methods on M2 Macrophage Phenotype and Function.," *J. Immunol. Methods*, vol. 426, pp. 56–61, Nov. 2015, doi: 10.1016/j.jim.2015.08.001.

[20] L. L. Burrows, "Pseudomonas aeruginosa Twitching Motility: Type IV Pili in Action," *Annu. Rev. Microbiol.*, vol. 66, no. 1, pp. 493–520, Sep. 2012, doi: 10.1146/annurev-micro-092611-

150055.

[21] N. M. Oliveira, K. R. Foster, and W. M. Durham, “Single-cell twitching chemotaxis in developing biofilms,” *Proc. Natl. Acad. Sci.*, vol. 113, no. 23, pp. 6532 LP – 6537, Jun. 2016, doi: 10.1073/pnas.1600760113.

[22] C. Qiuxian, L. Zhaojun, O. Qi, L. Chunxiong, G. V. D., and A. F. M., “Singly Flagellated Pseudomonas aeruginosa Chemotaxes Efficiently by Unbiased Motor Regulation,” *MBio*, vol. 7, no. 2, pp. e00013-16, Aug. 2021, doi: 10.1128/mBio.00013-16.

[23] I. Sampedro, R. E. Parales, T. Krell, and J. E. Hill, “Pseudomonas chemotaxis.,” *FEMS Microbiol. Rev.*, vol. 39, no. 1, pp. 17–46, Jan. 2015, doi: 10.1111/1574-6976.12081.

[24] J. Schindelin *et al.*, “Fiji: an open-source platform for biological-image analysis.,” *Nat. Methods*, vol. 9, no. 7, pp. 676–682, Jun. 2012, doi: 10.1038/nmeth.2019.

[25] C. Deroy, N. Stovall-Kurtz, F. Nebuloni, C. Soitu, P. R. Cook, and E. J. Walsh, “Predicting flows through microfluidic circuits with fluid walls,” *(Manuscript Submitted)*, 2021.

[26] S. Wąsik, M. Arabski, Z. Drulis-Kawa, and J. Gubernator, “Laser interferometry analysis of ciprofloxacin and ampicillin diffusion from liposomal solutions to water phase.,” *Eur. Biophys. J.*, vol. 42, no. 7, pp. 549–558, Jul. 2013, doi: 10.1007/s00249-013-0904-2.

[27] J.-Y. Tinevez *et al.*, “TrackMate: An open and extensible platform for single-particle tracking,” *Methods*, vol. 115, pp. 80–90, 2017, doi: https://doi.org/10.1016/j.ymeth.2016.09.016.

Supplementary Figures

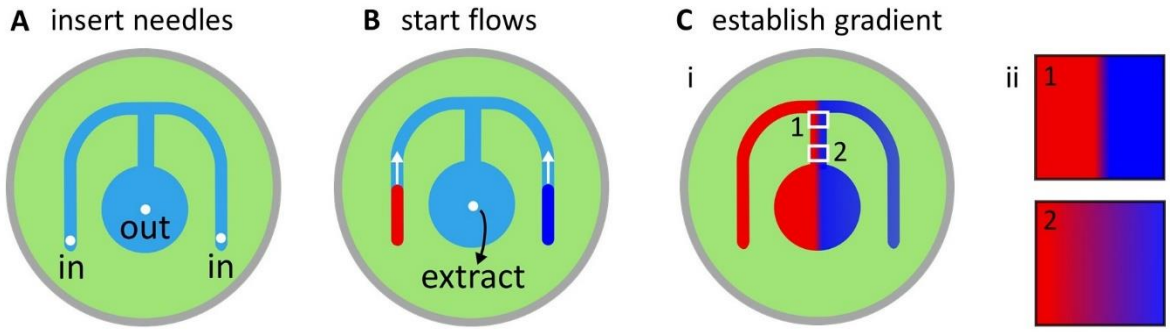


Fig. S1. Establishing gradients in fluid-walled circuits in an 'm'-shaped circuit. (A) Needles connected to syringe pumps via tubing are inserted into the arms and sink. **(B)** Red and blue dyes are pumped into the two arms and withdrawn from the sink at an equivalent flow rate. **(C)** As laminar streams of red and blue dyes meet in the central conduit, they flow side by side and diffuse laterally across the conduit. **(i)** White boxes labelled 1 and 2 illustrate regions with differences in diffusional mixing along the length of the conduit, and correspond to insets **(ii,1)** (where the gradient is steeper near the top of the conduit) and **(ii,2)** (where the gradient widens along the bottom of the conduit as particles have more time to diffuse), respectively.

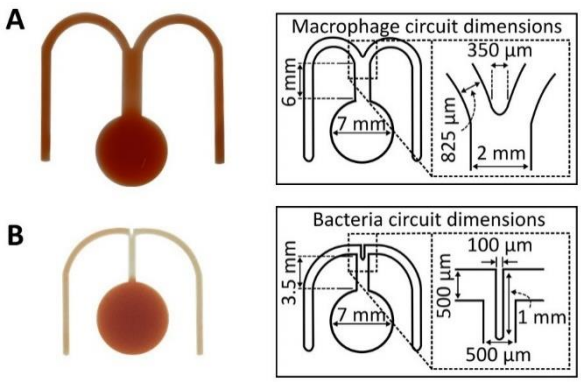


Fig. S2. Dimensions of circuits used to study macrophage and bacterial chemotaxis. (A) Left: micrograph of the circuit used with macrophages (red dye added to aid visualisation). Right: circuit dimensions. **(B)** Left: micrograph of the circuit used with bacteria (red dye added to aid visualisation). Right: circuit dimensions.

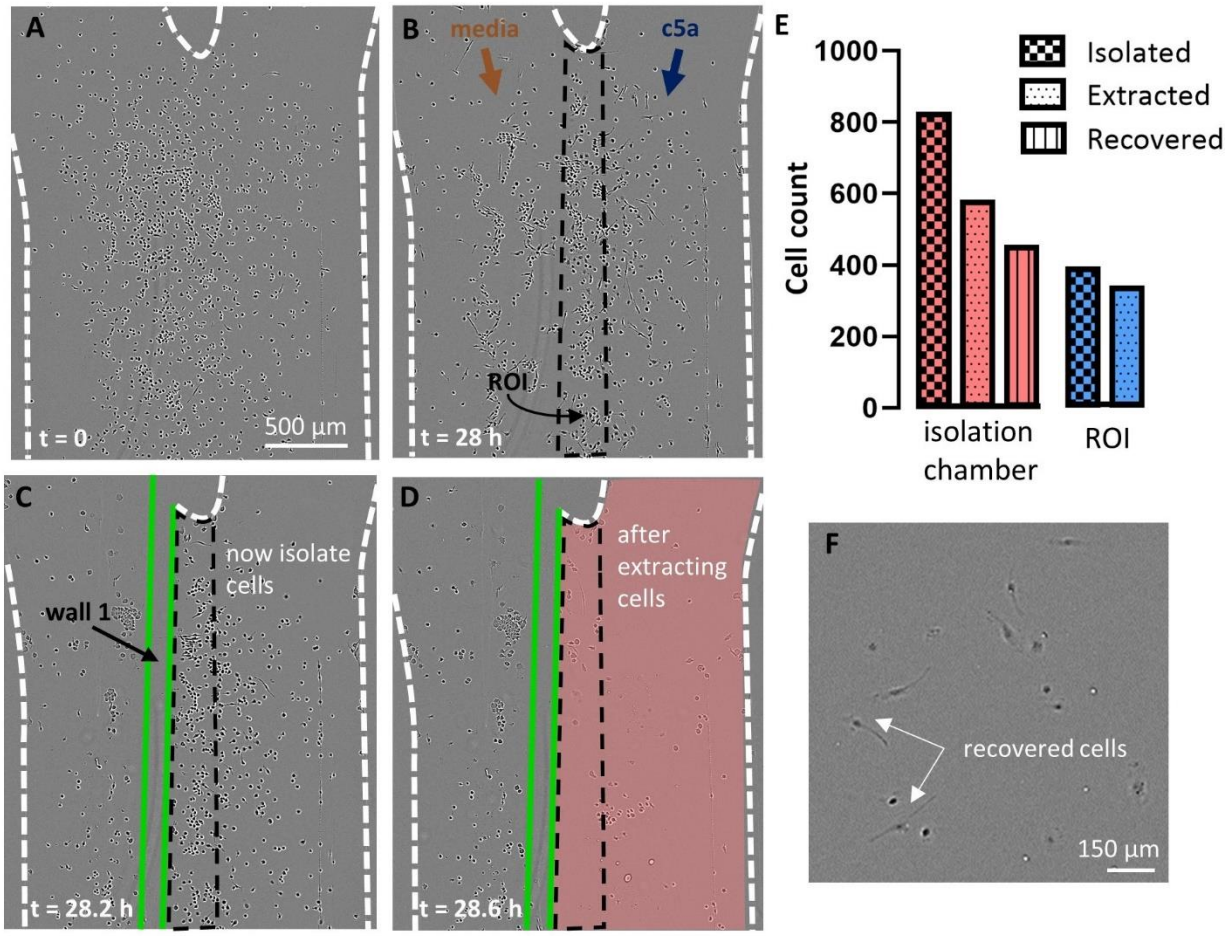


Fig. S3. Isolation, extraction, and recovery of chemotaxing BMDMs. Phase-contrast images were collected on the IncuCyte. **(A)** Image of BMDMs taken immediately after plating in the central conduit of the 'm'-shaped circuit. **(B)** Image of the conduit after 28 h as laminar streams of media and C5a flow over cells. Some cells sense the C5a gradient and migrate to the right to leave a zone with fewer cells. Analysis of the movie allows us to determine the region containing migrating cells (region of interest 'ROI', outlined). **(C)** Image of newly-built 'wall 1' (green, made using the stylus on the printer). A further two walls (not shown in image) are then built to completely seal off the region rich in chemotaxing cells from the rest of the circuit. **(D)** Image of the isolation chamber (pink) containing the ROI after extracting cells using the printer. **(E)** Graph quantifying the number of cells isolated, extracted, and recovered from within the isolation chamber and the ROI. Within the isolation chamber (which includes the ROI), 70.2% of isolated cells were successfully extracted with the printer (which includes 87% of the cells in the ROI). 80% of these extracted cells were later recovered after plating onto new culture dishes. **(F)** Image of recovered BMDMs from the

isolation chamber after transfer into new dishes and incubation for 24 h. Cells have reattached and present their characteristic pseudopodia.

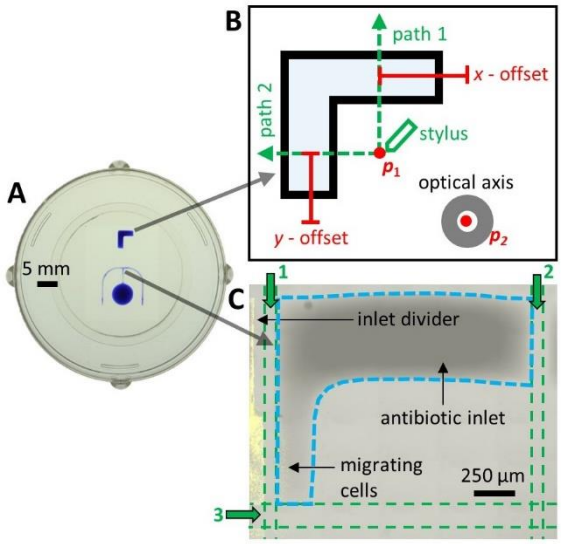


Fig. S4. Reconfiguring microfluidic circuits on a microscope to isolate chemotaxing *P. aeruginosa* without interrupting flow. (A) Image of dish with 'm' and 'L'-shaped circuits (both contain blue dye to aid visualisation). **(B)** Plan of 'L'-shaped circuit used to ascertain *x*, *y* offsets of stylus from the optical axis. After printing circuits, the condenser is lowered so the attached stylus touches the surface of the dish at an arbitrarily-chosen point (p_1) lying orthogonal to arms of the 'L'. Next, the motorised stage moves so that the stylus follows paths 1 and 2 over the dish surface. During movement, media in contact with the glass is displaced by the stylus, and – as FC40 wets glass better than media – FC40 walls pinned to the glass are built along paths 1 and 2. Mid-points in these newly-built walls are imaged through the objective lens, and *x*, *y* offsets from the optical axis (p_2) recorded. **(C)** Overlaid fluorescence and bright-field images of 'm'-shaped circuit (at junction between antibiotic arm and central conduit) that contains wild-type YFP-labelled *P. aeruginosa* cells, (a high density can be seen as the yellow on the left). Live-cell imaging of the biofilm over the previous ~24 h shows that many cells to the right of what will become path 1 were chemotaxing towards ciprofloxacin. Therefore, new FC40 walls were built successively along paths 1-3 (green arrows) to isolate these cells from others (see **Materials and Methods**). The volume within the dashed blue outline is now isolated from the rest of the dish. In this low-power view, individual cells yield insufficient fluorescence signal to be detected.

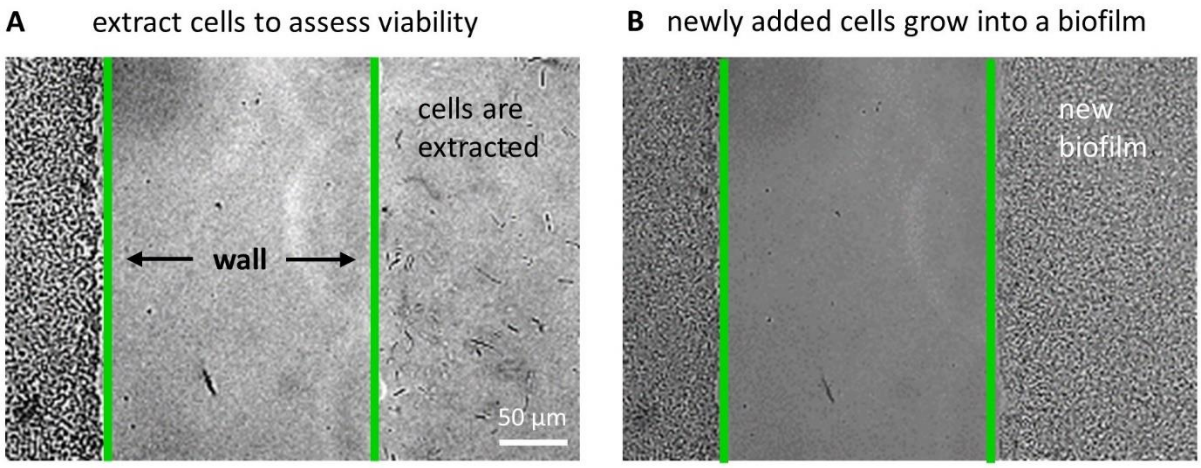


Fig. S5. Phase-contrast images showing that *P. aeruginosa* in newly-reconfigured circuits can be extracted or added to monitor division potential. (A) Image after extracting cells to the right of the wall; few cells remain in the chamber, and the dense biofilm to the left serves as a control. Subsequent plating of extracted cells on LB plates yields no colonies, showing none can divide. **(B)** Image taken 12 h after re-adding ~20 new WT cells in antibiotic-free media to the extracted area shows that washing the chamber thoroughly can remove essentially all antibiotic. The chamber is now completely covered in a biofilm of WT cells (indicating that cell growth and division is possible in the isolated region and that there is negligible residual antibiotic).

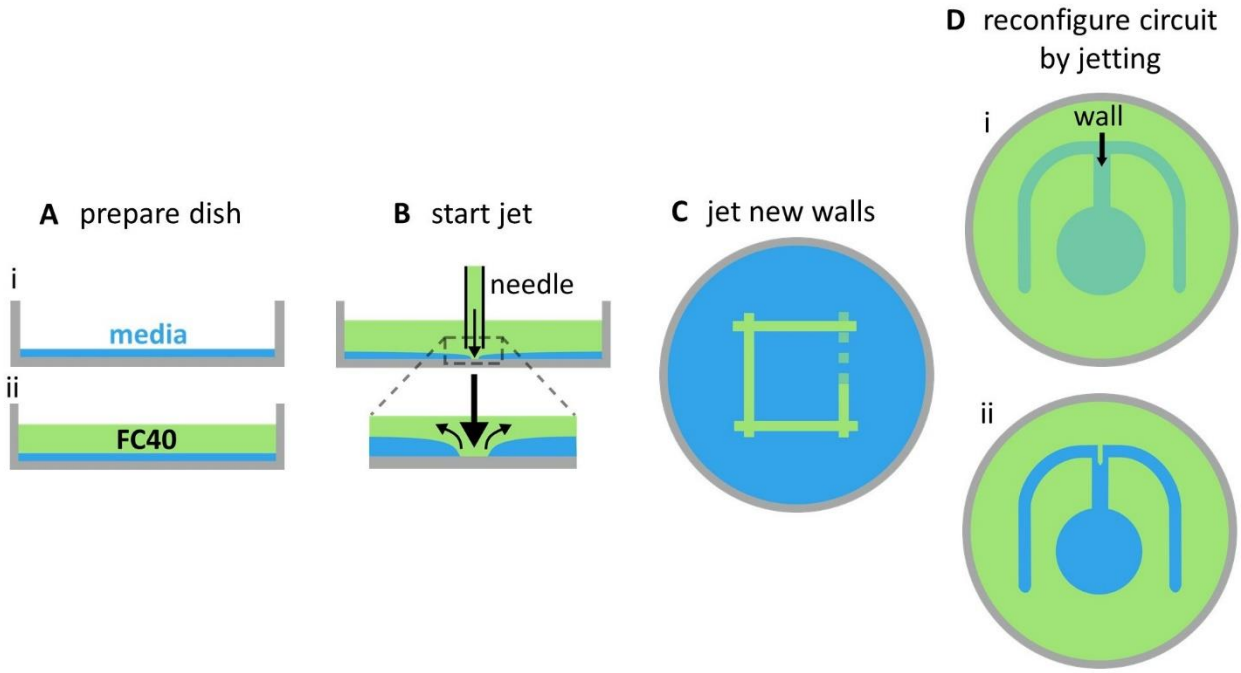


Fig. S6. Jetting enables fine-scale reconfiguration of microfluidic arrangements. (A) Preparing a dish for jetting. **(i)** A virgin Petri dish is overlaid with a thin film of media. **(ii)** Media is overlaid with a layer of FC40. **(B)** A dispensing needle loaded with FC40 is held in the FC40 above the dish. The needle 'jets' FC40, forcing media aside and allowing FC40 to wet the dish. FC40 wets the surface better than media, so it remains stuck to it. **(C)** Fluid walls may be built by moving the needle over the dish, shown here in the fabrication of a square. **(D)** We use jetting to create just the thin dividing wall at the point where both arms of the 'm'-shaped circuit used for *P. aeruginosa* meet (**Fig. S2B**). **(i)** The jetting needle moves along the path indicated by the black arrow to build a new wall. **(ii)** Representation of the completed circuit after jetting.

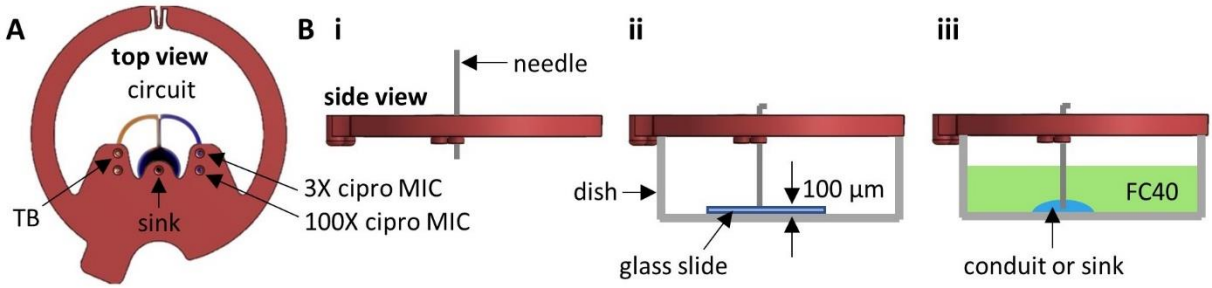


Fig. S7. Calibrating the height of needles used to infuse and withdraw fluid through fluid walls. (A) Image (top view) of a needle holder (red, CAD model) attached to a dish containing an 'm'-shaped circuit into which red and blue dyes have been pumped into the side arms (the edge of the dish is hidden by the circumference of the needle holder. The holder has holes (labelled) through which needles can be inserted that are positioned directly above appropriate points in the circuits. **(B)** Adjusting the height of an input needle (CAD views from side -/+ cartoons below; a similar procedure is used with the other two needles). **(i)** The needle is inserted through the needle holder. **(ii)** The needle is fitted to the dish with a glass cover-slip (height 100 µm) glued to the bottom, and lowered until it contacts the cover-slip; then, the needle is bent to fix its vertical position in the holder. **(iii)** When the needle holder is placed on a dish with a circuit, the needle is now at the correct height relative to the circuit.

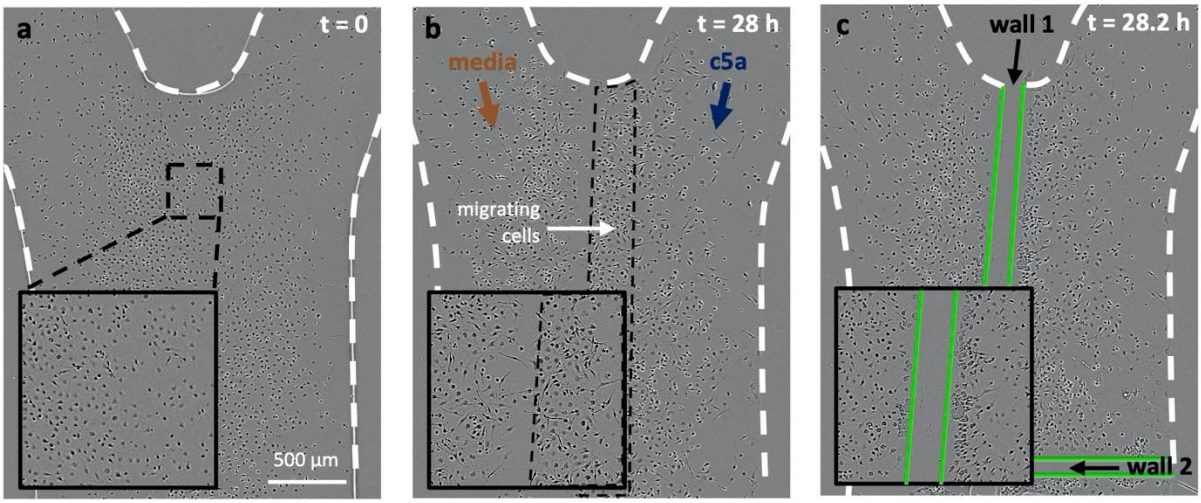


Fig. S8. Reconfiguring a microfluidic circuit on a microscope to isolate populations of chemotaxing BMDMs. Chemotaxing BMDMs in response to a gradient of C5a are isolated from the population of non-migrating cells using live microscopy, by using an adaptor fitted to the condenser of the microscope (as in **Fig. 2**) **(A)** BMDMs are plated into the central arm of an 'm'-shaped circuit (inset shows close-up of cells). **(B)** Two laminar streams of a chemoattractant (C5a, right) and cell culture media (left) are generated over the cells. Diffusion creates a stable concentration gradient of C5a along the length of the conduit. Cells within the gradient sense the increasing concentration of C5a and migrate towards it over ~28 h. Analysis of the movie made allows us to determine the region containing the population of migrating cells (in the dashed box). **(C)** The microscope is fitted with a similar adaptor to that shown in **Figure 2** which holds a PTFE stylus used to make a new fluid wall along the length of the conduit (green, 'wall 1'). This isolates the population of migrating cells (to the right of wall 1) from non-responsive cells. 'Wall 2' downstream and 'wall 3' upstream (not visible in the image) are then made to completely seal the cells from the rest of the circuit (as in **Fig. 3C**).

Supplementary Videos

Movie S1. Phase contrast movie of chemotaxing macrophages. BMDMs in a C5a gradient (media input at left, and 10 nM C5a at right); they chemotax towards C5a over ~28 h.

Video link: Movie S1

Movie S2. Phase contrast movie of chemotaxing bacterial cells. *P. aeruginosa* in ciprofloxacin gradient (TB + a phase-dark blue dye is input at left to give the dark region, and the antibiotic at 100X MIC is input on the right to give the phase-light region); they chemotax towards the antibiotic over ~24h. The gradient extends over ~70 µm.

Video link: Movie S2

Supplementary STEP files of the 3D-printed parts

STEP files from the CAD models of the 3D-printed adaptors used to transform a microscope into a reconfiguring tool, including:

- Dish Holder
- Needle Holder
- Microscope Stage Insert
- Microscope Stylus Holder

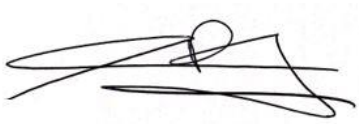
Statement of Authorship for joint/multi-authored papers for PGR thesis

To appear at the end of each thesis chapter submitted as an article/paper

The statement shall describe the candidate's and co-authors' independent research contributions in the thesis publications. For each publication there should exist a complete statement that is to be filled out and signed by the candidate and supervisor **(only required where there isn't already a statement of contribution within the paper itself).**

Title of Paper	Reconfiguring microfluidic circuits to isolate and retrieve cells of interest
Publication Status	Unpublished and unsubmitted work written in a manuscript style
Publication Details	C. Deroy, J. H. Wheeler, A. Rumianek, D. R. Greaves, P. R. Cook, W. M. Durham, K. Foster, and E. J. Walsh.

Student Confirmation

Student Name:	Cyril Deroy		
Contribution to the Paper	Lead author, designed and performed all experiments, designed and printed all 3D adaptors, collected and analysed data, prepared all figures, coordinated and contributed to manuscript writing and editing.		
Signature		Date	27/09/2021

Supervisor Confirmation

By signing the Statement of Authorship, you are certifying that the candidate made a substantial contribution to the publication, and that the description described above is accurate.

Supervisor name and title: Prof. Edmond Walsh		
Supervisor comments		
Signature 	Date	27/09/21

This completed form should be included in the thesis, at the end of the relevant chapter.

Chapter 5: Fluid-walled microfluidic assay for macrophage chemotaxis

Authors: Cyril Deroy, Agata Rumianek, James H. R. Wheeler, David R. Greaves, Peter R. Cook, Edmond J. Walsh

Abstract

Chemotaxis plays an essential role in regulating the immune system by directing the migration of macrophages to infection sites. While many tools are available to study chemotaxis *in vitro*, current microfluidic methods fail to offer many desirable features; these include placing cells in pre-defined patterns, imaging them in real-time as they migrate, extracting specific sub-populations for downstream analysis, and high-throughput capabilities allowing comparison of multiple cell-types. Using a fluid-shaping technology, we build microfluidic circuits on standard Petri dishes, deposit primary murine macrophages in different patterns, and image them as they chemotax towards complement component 5a (C5a); concentration gradients are established by diffusion in both flow-free and flowing environments that allow spatiotemporal shifting of gradients. We then quantify cell directionality and velocity, and relate responses to concentration gradients determined using a theoretical model; only cells at leading edges respond, as others at the same local concentration do not. We also develop circuits facilitating comparison of multiple cell-types responding to one C5a source, as well as in individual wells of 6-well plates.

Introduction

Cells often experience environments with heterogeneous chemical signals. These signals typically induce cell migration and play crucial roles in regulating homeostasis [1]. Directed migration of cells in response to chemical concentration gradients, known as chemotaxis, is fundamental to numerous biological processes. For instance, chemotactic signals are essential for the immune system, as they direct immune cells throughout the body to sites of inflammation. However, they also contribute to pathological processes such as atherosclerotic plaque formation, where lipid-laden macrophages (foam cells) build-up in regions of high-cholesterol within arteries to form plaques that can lead to atherosclerosis [2].

To study chemotaxis, transwell assays (introduced in the early 1960s with the Boyden chamber) offer an easy solution; a porous insert containing cells is placed inside a well loaded with chemoattractant, and once a concentration gradient is established by diffusion, cells migrate through micrometre-sized pores into the well, and chemotaxis is quantified by removing the insert and counting cells in the well [3]. Other variants (e.g., xCELLigence real-time chemotaxis system) coat the membrane in a gold microelectrode to measure impedance changes that arise from cells crossing the membrane [4]. Alternatives to transwell assays were also introduced to address some of its limitations, including tracking and monitoring single cells (as in Dunn chambers) [5], and detecting cell reversibility or fugetaxis (as in under-agarose migration assays) [6]. More recently, microfluidic systems have been developed [7] that enable control of stable gradients [8], distinguishing between various types of cell movement (e.g., chemotaxis, chemokinesis or random cell migration, and fugetaxis [9]), tracking individual cells in real-time [10], performing parallel and high-throughput screens

[11], and minimising reliance on specialised equipment [12]. While microfluidics show promise, its uptake in biomedical research has been impeded by the technical complexity required to operate devices, long prototyping and fabrication times, the problematic biocompatibility of polydimethylsiloxane (PDMS), and failure rates associated with air bubbles blocking or disturbing flow patterns [13], [14].

Here, we introduce open microfluidic circuits designed for chemotaxis studies. Using a recently-developed fluid-shaping technology [15], [16], we design and print both static (passive) and dynamic (active) circuits on standard 35 mm Petri dishes, seed primary murine bone-marrow derived macrophages (BMDMs) into circuits, and monitor the well-documented chemotaxis towards complement component 5a (C5a) [17]. We then extend the method to perform higher-throughput assays in 6-well plates. Due to the unique flexibility of the approach, we demonstrate previously under-appreciated self-limiting behaviours and spatiotemporal sensing mechanisms of BMDM chemotaxis.

Results

Workflow and operation

Printing circuits

Circuits are printed on standard 35 mm Petri dishes using a custom-built printer as described previously [16]. Briefly, the printer consists of a 3-axis traverse that holds a dispensing needle used to add/remove cells, or jet FC40. We first print cells in any desired 2D pattern by simply infusing culture medium containing suspended BMDMs through the dispensing needle and on to the surface of a dish (**Fig. 1Ai**). The dish is then placed inside an incubator for 5 minutes to allow cells to attach, and then the bottom of the dish is gently and completely covered with media; as macrophages are strongly adherent, they remain firmly attached to the dish where they were originally deposited (**Fig. 1Aii**). Most media is now removed to leave a thin layer, which is immediately covered with FC40 – a bioinert and liquid fluorocarbon that prevents media evaporation. After returning the dish to the printer in the same original orientation, another dispensing needle jets a stream of FC40 through the thin layer of medium on to the bottom of the dish (**Fig. 1Aiii**); this jet pushes media aside so FC40 locally contacts – and adheres to – the bottom of the dish. This process reshapes the fluid-fluid interface between media and fluorocarbon, to create what we will refer to as a fluid wall. The jet is then moved to create what will become the footprint of the fluid walls that outline the circuit. Using this technique, we create both passive dumbbell-shaped circuits (**Fig. 1Aiv**) and active 'm'-shaped circuits (**Fig. 1Av**).

Loading and generating stable gradients in passive circuits

Passive circuits have the advantage of not requiring additional equipment such as syringe pumps, tubes, and needles to generate concentration gradients. Instead, reagents are

pipetted directly through the fluid walls into the circuit (**Fig. 1Bi-ii**), either manually or robotically on the printer. As reagents are added sequentially in each dumbbell chamber, it is necessary to ensure that concentration gradients are established by diffusion (and not by advection induced by pressure differences). Pressures in the circuit are originally at equilibrium. Then, medium (1 µL) is added to the top chamber (red dye in **Fig. 1Bi**) to increase its Laplace pressure (defined as $\Delta P = \frac{\gamma}{R}$, where $\gamma =$ interfacial tension, $R =$ radius of curvature, and $P_{top} = 20$ Pa); consequently, medium starts to flow down to the bottom chamber (**Fig. 1Bii**). At this point, a small volume of chemoattractant (0.5 µL) is added to the bottom chamber (blue dye in **Fig. 1Bii**; $P_{bottom} = 11$ Pa). In turn, this increases the Laplace pressure in the bottom chamber, decreases the pressure gradient throughout the circuit ($P_{circuit} = 9$ Pa), and the system rapidly equilibrates once 0.25 µL media have entered the bottom chamber (shown as red dye entering the blue chamber in **Fig. 1Biii**). Without flow, diffusion now creates a steady concentration gradient of attractant throughout the conduit (**Fig. 1Biv,v**).

Steady-state and gradient stability

The rate of change in concentration of a substance by diffusion is described by Fick's second law as $\frac{\partial c}{\partial t} = D\frac{\partial^2 c}{\partial x^2}$ ($c =$ concentration, $t =$ time, $x =$ distance, $D =$ diffusion coefficient). During the initial transient phase, the concentration gradient in the conduit is defined using the one-dimensional solution to the diffusion equation in a semi-infinite medium, $c(x,t) = c_0 erfc\left(\frac{x}{2\sqrt{Dt}}\right)$ ($c_0 =$ concentration at the boundary) [18]. From this expression, we estimate the time required for the concentration gradient to reach steady-state after the addition of chemoattractant in the bottom chamber of the circuit. This time is

set to correspond to 15% of the initial concentration c_0 reaching the end of the conduit, and is defined as $t_{SS} = \frac{x^2}{4D \times erfc^{-1}(0.15)}$, where $x =$ conduit length. After reaching steady state, the concentration gradient in the conduit is linear and set to vary from 0 to 10 nM. As $t_{SS} \propto x^2$, doubling conduit length will quadruple the time to reach steady-state (e.g., for C5a in our system, if $x = 2$ mm, $t_{SS} \approx 1.5$ h; if $x = 4$ mm, $t_{SS} \approx 6$ h; **Table S1**).

We next determine the rate of mass transfer through a conduit from Fick's first law of diffusion $J = -D\frac{dc}{dx}$ ($J = \frac{\dot{m}}{A}$, $\dot{m} =$ mass flow rate, $A =$ area) to assess the duration of these stable gradients (and predict maximum experimental runtimes). Assuming the concentration gradient remains approximately constant until 5% of the analyte's initial concentration c_0 reaches the top chamber where it becomes evenly distributed ($c_{end} = 0.05c_0$), we define the maximum experimental runtime as $t_{end} = 1.05\frac{xm_{c5a}}{DAc_0}$ ($A =$ conduit cross-sectional area, $m =$ mass of C5a). The cross-sectional area of a conduit is expressed as $A = \frac{a^2}{2\,sin^2\,\theta}\left(\frac{\theta\pi}{90} - sin2\theta\right)$, where $a =$ conduit half-width and $\theta =$ contact angle. In this study, conduits have fixed widths so $t_{end} \propto x$, thus t_{end} varies proportionally to conduit length (e.g., for $x = 2$ mm, $t_{end} \approx 15$ h; for $x = 4$ mm, $t_{end} \approx 30$ h; **Fig. S1**, **Table S1**).

Moving dishes containing passive circuits does not impair gradient formation

As passive circuits are printed and prepared on the printer and then moved to the microscope for imaging, movement-induced convective flows could perturb gradients. We therefore monitored gradient uniformity; 12 circuits were printed, loaded with fluorescein as previously described, and moved from the printer (placed inside a biosafety cabinet to ensure sterility) to an imaging system contained in an incubator (an IncuCyte ZOOM). A fluorescent

scan of the whole dish is then taken to evaluate the gradient in each individual circuit. As shown in **Figure 1C**, the fluorescein front is located at approximately the same distance from the bottom chamber in each conduit, confirming that gradients in all were identical.

Setting up gradients in active circuits

Stable concentration gradients in 'm'-shaped circuits are established as described elsewhere [19]. Briefly, two syringes are prepared with medium ± chemoattractant, placed on a syringe pump, connected to needles via polytetrafluoroethylene (PTFE) tubing, and inserted into the left and right arms of the circuit respectively. The syringes then start infusing at a constant flow rate, so media (red dye added in **Fig. 1Di**) and media + chemoattractant (represented by blue dye in **Fig.1Di**) meet as laminar streams in the central conduit. Diffusion then creates a stable concentration gradient across the width of the conduit. The steepness of this gradient is controlled by varying the overall flow rate in the conduit (lower rates yield shallower gradients, **Fig.1Dii**). A third needle connected to another syringe on a separate pump is inserted into the sink and withdraws fluid at an equivalent flow rate.

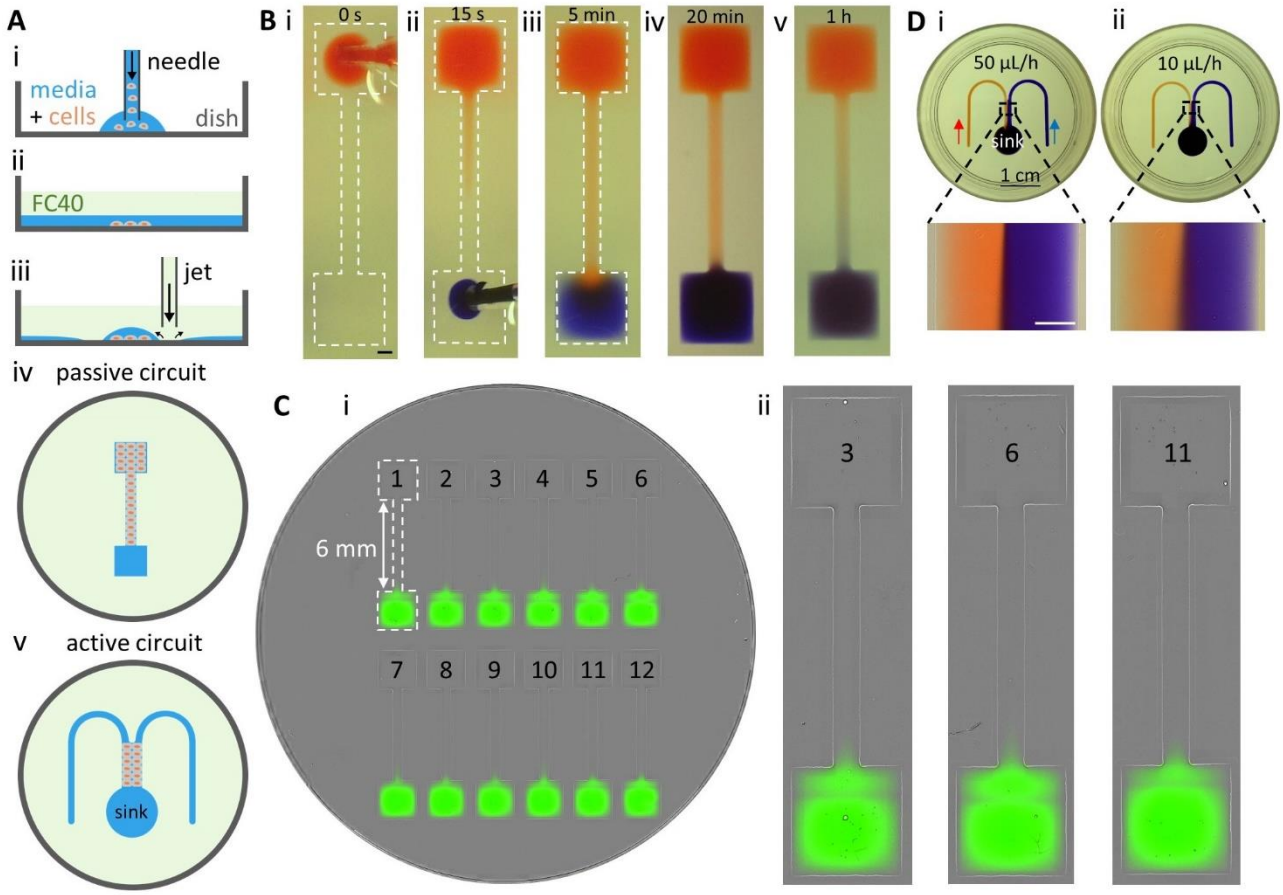


Fig. 1. Printing circuits and setting up gradients. (A) Printing passive and active circuits around patterned cells. **(i)** A needle infuses media containing cells in a dish; moving the needle laterally deposits cells in the desired pattern. **(ii)** Once cells attach, the bottom of the dish is covered with medium, most media removed to leave ~50 µL in a thin layer, and FC40 (2 mL) overlaid. **(iii)** A needle loaded with FC40 is lowered into FC40 until just above the medium, and jets FC40 on to the dish to replace medium with FC40 that remains locally stuck to the dish. Moving the jet around cells will now create a continuous isolating FC40 wall and the desired circuit. **(iv)** Flow-free (passive) dumbbell circuit. Cells are dispensed into a rectangular drop, before jetting the dumbbell-shaped wall around them. **(v)** Active 'm'-shaped circuit. Cells are plated in a rectangle and walls jetted to create the circuit. **(B)** Establishing gradients in a passive dumbbell circuit. Red and blue dyes represent medium and C5a. Dashed lines: wall footprint. Scale bar = 500 µm. **(i)** Red dye (1 µL) is manually pipetted into the top chamber. **(ii)** Resulting pressure differences induce convective flow down the conduit. A volume of blue dye (0.5 µL) too small to reverse this flow is pipetted into the bottom

chamber. **(iii)** After 5 min, red dye has entered the bottom chamber, the system equilibrates, and diffusion will now establish the gradient. **(iv)** Blue dye starts to diffuse up the conduit. **(v)** After 1 h, linear concentration gradients of each dye are established. **(C)** Gradients in dumbbells remain undistorted as dishes are moved from printer to microscope. **(i)** Image of a whole 35 mm dish containing 12 identical dumbbells formed by stitching together smaller images. Medium, or medium + fluorescein, are loaded into upper and lower chambers as in (B) by a printer, the dish transferred to a microscope, images collected after 20 min, and stitched together. The fluorescein front diffuses up the conduit to reach the same place in all 12 conduits. Incorrect stitching by the software yields dark lines in lower chambers. **(ii)** Close-ups of 3 circuits. **(D)** Establishing gradients in an active 'm'-shaped circuit. **(i)** Image of circuit as dyes are infused continuously (each at 25 μL/h) through flanking arms to flow as laminar streams down the central conduit. Diffusion creates a gradient across the conduit. Inset: gradient width increases down the conduit (scale bar = 500 μm). **(ii)** As (i), but now dyes are each infused at 5 μL/h. Inset: the gradient is shallower, as dyes have more time to diffuse (as flow is slower).

Passive circuits for BMDM chemotaxis

Exposing BMDMs to gradients of C5a

We demonstrate the approach by monitoring chemotaxis of BMDMs in response to a gradient of C5a that falls from 10 nM – the concentration eliciting the strongest chemotactic response in traditional transwell dose-response experiments (**Fig. S2**). Initially, all cells are in the top chamber of a dumbbell-shaped circuit (**Fig. 2Ai**), C5a (10 nM) is pipetted into the bottom chamber, and a time-lapse movie is made of the conduit over the next 48 h (**Movie 1**; 1 frame every 20 min). Almost no cells are seen in the first frame of the movie (**Fig. 2Aii**). As the gradient becomes established over time ($t_{SS} = 0.9$ h) , progressively more cells enter the conduit and by the last frame some have even reached the bottom chamber (**Fig. 2Aiii**). Tracks of individual cell trajectories are now derived by analysing successive images in the

movie; these tracks show a biased movement of cells towards C5a (**Fig. 2Aiv**; blue tracks indicate movement towards C5a, red ones away from it, and black dots show static cells). Tracked cell trajectories are also binned according to angle and displayed as rose plots (**Fig. 2Av**; blue segments indicate the proportion of tracks towards C5a, and red ones away from it, with segment length indicating the number of tracks per bin). We next examine the response of cells already in the conduit to the same gradient (**Fig. 2B**; **Movie 2**). Now, cells are visible in the first frame (**Fig. 2Bii**). Whilst many cell trajectories are biased towards C5a, some are not (**Fig. 2Biv**); in other words, only some cells chemotax, and rose plots confirm this (**Fig. 2Bv**).

Distinguishing between chemotaxis and chemokinesis

In the absence of concentration gradients, cells typically move randomly – a behaviour described as chemokinesis. Whilst rose plots clearly indicate that some macrophages exhibit directed movement in the presence of C5a gradients (and so chemotaxis), rose plots from controls performed in circuits without C5a in either chamber (**Movie 3**), or with the attractant initially in both chambers (**Movie 4**), show no bias (**Fig. 2Cii,iii**). We also quantify chemotactic cell velocities (v_{taxis}, average y-velocity) and net-to-gross displacement ratio (NGDR) for each condition. Chemotactic velocities are calculated by averaging the y-velocities of each trajectory (positive velocities towards the top chamber, negative velocities towards the bottom chamber). Thus, in the presence of a gradient, the resulting negative values obtained for v_{taxis} indicate biased movement towards the C5a chamber (**Fig. 2Av** & **Fig. 2Bv**). In controls, $v_{taxis} = 0$ μm/min, confirming the absence of chemotactic bias (**Fig. 2Cii,iii**). The NGDR is defined as the straight-line distance between start and end points of a trajectory divided by the total distance travelled along the path of the trajectory [20]; therefore, an

NGDR of 1 indicates the cell travelled in a straight line from start to finish irrespective of whether it was towards (or away from) attractant, with progressively lower values indicating increased randomness (**Fig. 2D**). Altogether, these results confirm previous results that BMDMs chemotax towards C5a [17].

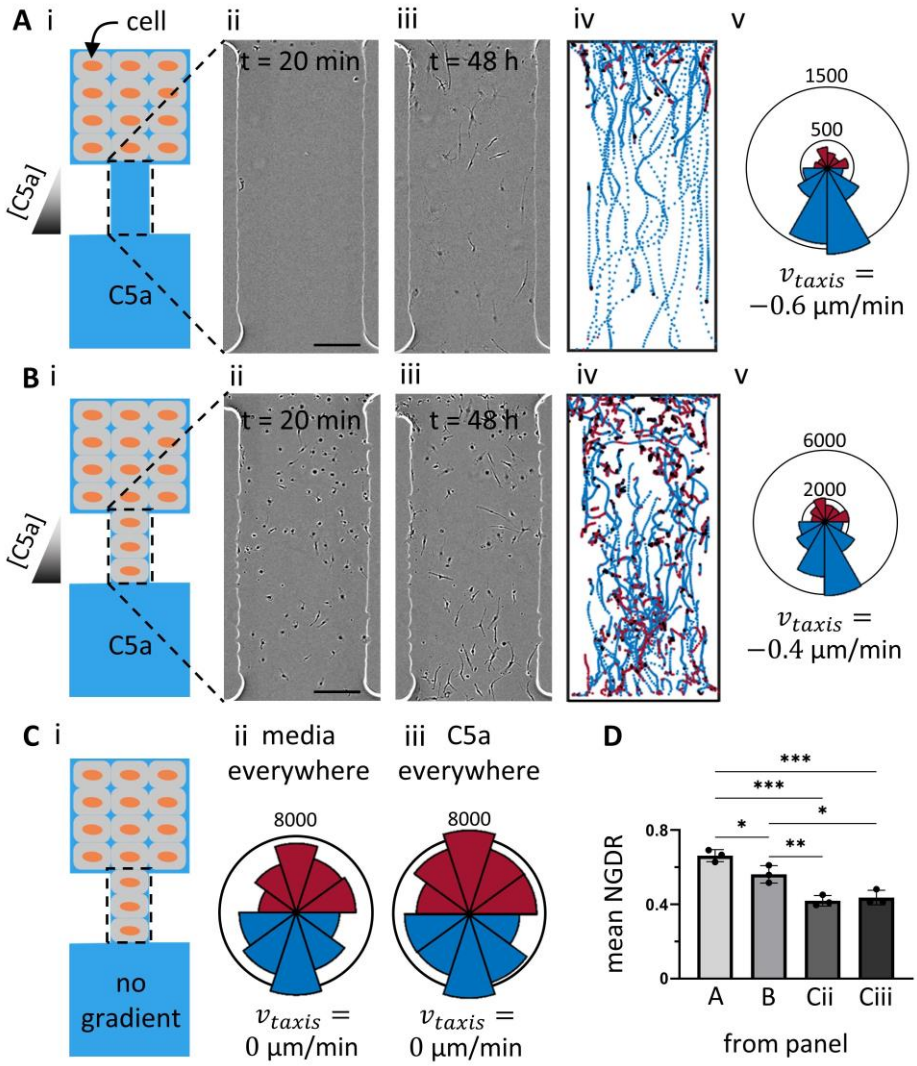


Fig. 2. Tracking chemotactic bias in dumbbells jetted around BMDMs. C5a (10 nM) is generally added to the bottom chamber, movies of the conduit made over 48 h, trajectories of individual cells extracted, and rose plots generated (n = 3 mice for each condition). **(A)** Migration of cells initially present only in the top chamber. **(i)** Cartoon showing starting positions of cells (grey with orange nuclei). **(ii,iii)** Images of conduit.

Cells migrate into an empty conduit; many are elongated with characteristic pseudopodia. Scale bar = 250 μm. **(iv)** Cell trajectories. Downward tracks towards C5a (blue) outnumber upward ones (red). Black tracks: stationary cells. **(v)** Rose plot with the circles indicating number of trajectory points falling into each bin and measurements of v_{taxis} confirming this bias. **(B)** Migration of cells initially present in both top chamber + conduit. **(i)** Cartoon showing starting positions of cells. **(ii,iii)** Images of conduit; many cells are elongated vertically. Scale bar = 250 μm. **(iv)** Trajectories are again biased towards C5a. **(v)** Rose plot with the circles indicating number of trajectory points falling into each bin and measurements of v_{taxis} confirming this bias. **(C)** Controls performed on **(i)** cells initially present in the top chamber + conduit, and rose plots with **(ii)** medium alone or **(iii)** C5a in both chambers showing lack of bias. **(D)** Mean NGDR (+SD, n = 3 mice) for C5a gradients from conditions in panels A, B, Cii, and Ciii; one-way ANOVA statistical significance $p<0.05$.

Cells at the front behave differently from those behind

Patterning cells in conduits reveals different population dynamics

Thus far, we have imaged short conduits (length 1.5 mm) initially containing no cells, or those where cells are uniformly distributed everywhere. We now compare responses of cells distributed in 4 different patterns in longer 6 mm conduits (chosen to improve resolution, but note that now $t_{SS} = 13.6$ h); initially, cells occupy either the whole conduit (**Fig. 3A**, purple), or just the top (**Fig. 3B**, green), middle (**Fig. 3C**, red), or bottom third (**Fig. 3D**, blue). Since all 4 conduits have the same dimensions and as bottom chambers are filled with the same C5a concentration, diffusion will establish identical gradients in all conduits that develop similarly over time. Remarkably, trajectories of cells at equivalent points in the y axis in the 4 conduits often differ. Thus, consider the conduit initially filled uniformly with cells: only cells in the bottom third yield long blue trajectories and a biased rose plot, whilst those above them do not (**Fig. 3A**). This might be expected: responders lie close to the

highest attractant concentration, and non-responders far from it. Now consider the other three panels (**Fig. 3B-D**). The front closest to C5a is always rich in responders, but this is found at different distances from the lower chamber. In other words, responses seem to depend more on whether cells are at the front, and not on the C5a concentration expected at that point in the conduit.

Determining chemotactic responses to concentration and gradient strength

We next determine the lowest C5a concentration eliciting chemotaxis (c_{min}) in each of the four circuits described in **Figure 3**. Macrophages move by extending pseudopodia that pull the cell over the substrate, and such pseudopodia extending towards an attractant are early visible markers of chemotaxis [21]. Therefore, we trace cells giving the long blue trajectories back in time in movies, identify when and where they first extend pseudopodia towards attractant (**Fig. S3**), and calculate the local C5a concentration present at that time in that place (using the solution to the 1D diffusion equation). Unfortunately, these movies are collected using a framerate of 20 min, and this limits the temporal resolution achieved (higher framerates can be acquired by reducing the imaged area or increasing scan rate, but then overheating can alter cell behaviour and even kill cells). Therefore, we recognize the concentration, $c_{min_{obs}}$, present in the earliest frame in which such pseudopodia are seen is an upper limit of c_{min}. Then, in movies used for **Figure 3A** and **D** (**Movie 5,8**), marker pseudopodia are seen at the bottom of the conduit in the first frame, and $c_{min_{obs}}$ is ~1 nM (**Table 1**). For movies used for **Figure 3B** and **C** (**Movie 6,7**) the markers are seen in the second frame, and values for $c_{min_{obs}}$ are much lower (**Table 1**). Values for the concentration gradients at the points where cells respond are also given in **Table 1**.

Table 1. Initial response concentration and gradient for circuits in Figure 3

	whole	top	middle	bottom
$c_{min_{obs}}$ (nM)	1.01 ± 0.29	1.2e-4 ± 1.8e-5	7.9e-2 ± 6.2e-3	1.8 ± 0.06
gradient (nM/mm)	3.1e-12 ± 7.4e-13	5.9e-16 ± 8.6e-17	2.52e-13 ± 1.8e-14	4.9e-12 ± 1.3e-13

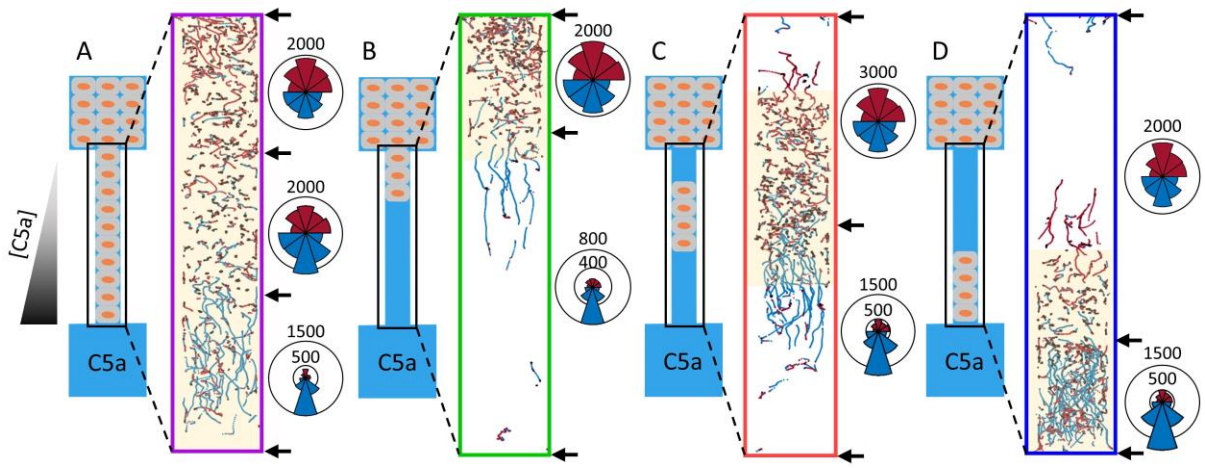


Fig. 3. First contacts respond to C5a. BMDMs are printed in different patterns, C5a gradients established (0-10 nM), and cells imaged for 48 h. Cartoons illustrating circuits (conduit length 6 mm) plus cell starting positions, trajectories from a single experiment (blue – towards C5a, red – away from C5a, black – stationary), and rose plots (n = 3 mice; blue – towards C5a, red – away from C5a with circles indicating number of trajectory points falling into each bin) are shown at the left, right, and middle of each panel, respectively. Yellow shading: initial position of cells. **(A)** Cells initially throughout the conduit (gradient shown). Only those at the bottom yield long trajectories towards C5a, and rose plots confirm this bias. **(B)** Cells initially in the top third of the conduit respond to C5a to give long blue trajectories, and biased rose plots – in contrast to those in (i) with the same starting positions. **(C, D)** Cells in islands initially in the middle and bottom of the conduit again show biased migration towards C5a – again in contrast to those in (A) with the same starting positions.

Comparing multiple cell types and high-throughput chemotaxis studies in well plates

Label-free comparison of different cell populations in single circuits

We next design and implement circuits with 3 chambers used to compare chemotactic responses of two cell populations without adding distinguishing cell labels (**Fig. 4A**). The middle chamber serves as a C5a reservoir, while chambers and conduits above and below contain different cells. To establish gradients, media is first added to the top chamber (1 µL, $P_{top} = 20$ Pa), a slightly smaller volume to the bottom one (0.9 µL, $P_{bottom} = 18.5$ Pa), and C5a to the middle one (0.6 µL, $P_{middle} = 13$ Pa). This creates pressure gradients that drive media into the C5a chamber (**Fig. 4Ai**, red dye represents media, blue represents C5a) until the system reaches equilibrium; then, diffusion creates a steady gradient of C5a along both conduits (**Fig. 4Aiii**). To demonstrate the approach, C5a-receptor knock-out (KO) BMDMs are initially at the top, wild-type (WT) BMDMs at the bottom, and 10 nM C5a in the middle. As expected, KO cells exhibit unbiased chemokinesis in the upper conduit (**Fig. 4Aiv**, rose plot in top inset), as WT cells chemotax towards C5a (**Fig. 4Aiv**, rose plot in bottom inset; **Movie 9,10**). This demonstrates how responses of two different cell types can be compared in a single microfluidic system without the need to add identifying labels.

Increasing throughput using well plates

The printer used thus far can accommodate nothing larger than one 6 cm dish. To increase throughput, we use a custom-built three-axis traverse with a working area large enough to hold several standard well plates and build 12 identical dumbbell circuits in each well of one 6-well plate (giving 72 circuits in total; **Fig. 4Bi**). Cell responses in such circuits are

essentially similar to those obtained in **Figure 2**, illustrated by the biased mean NGDR seen when C5a is present (**Fig. 4Bii**). This general approach gives users flexibility in choice of circuit design. For example, the 5-chambered circuits in **Figure 4Cii-v** – prepared in wells in standard 6-, 12-, 24-, and 48-well plates – could be used to compare responses of 4 different cell types to one chemoattractant in the central chamber. Circuits can even be shrunk to fit in each well of a 96-well plate, illustrated by printing pairs of chambers connected by 1-8 conduits (**Fig. 4Cvi**).

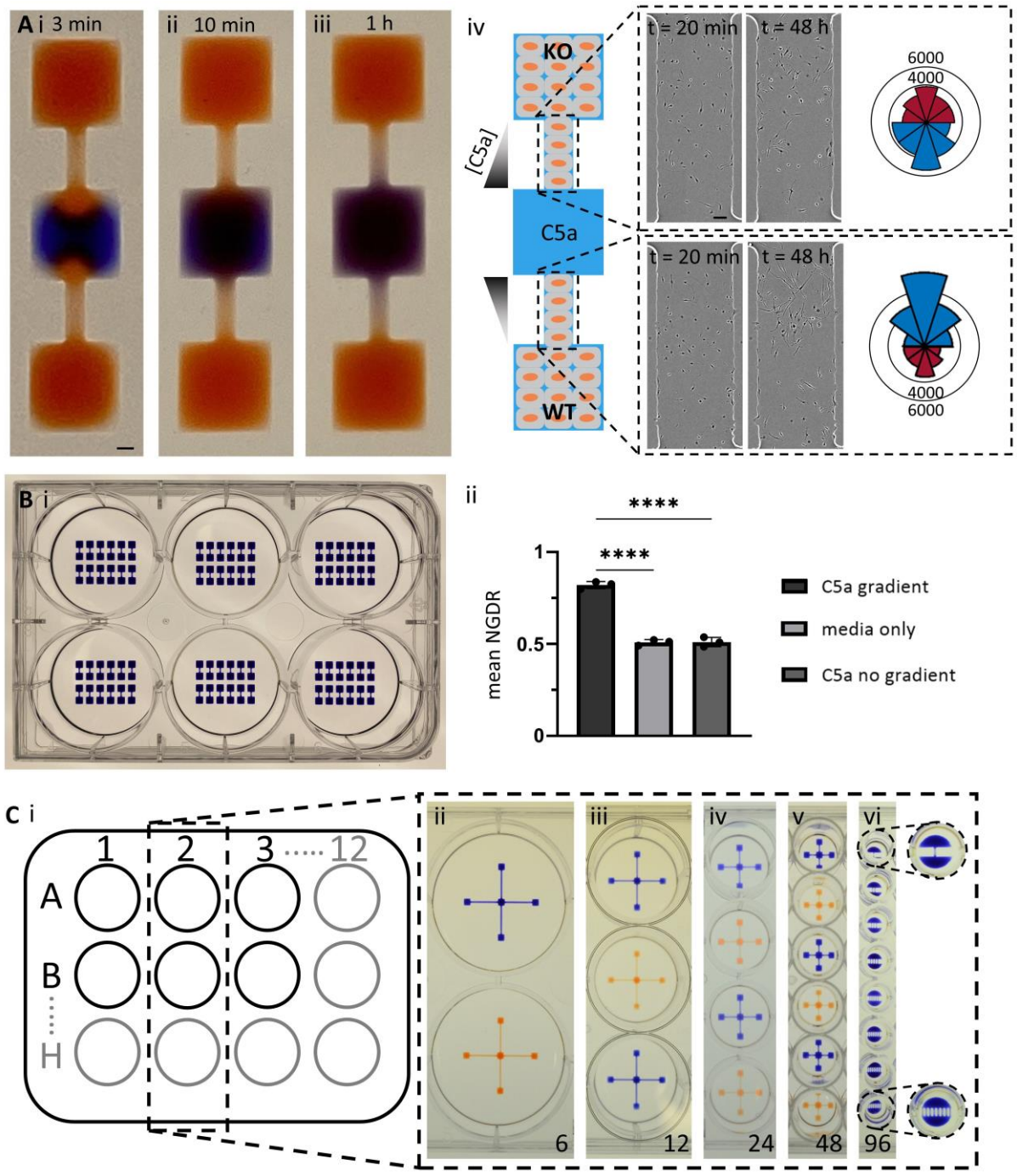


Fig. 4. Comparing chemotaxis of 2 different cell types in a single circuit, and increasing throughput. (A) Two different cell types in one 3-chamber circuit. Scale bar = 500 µm. **(i)** Images during generation of stable gradients. At t = 0, dyes are pipetted manually into chambers – first 1 µL red into the top chamber, 0.9 µL red into the bottom one, and finally 0.6 µL blue into the middle one. After 3 min, the induced pressure difference has driven red dye into the middle chamber, and pressures equilibrate. **(ii)** After 10 min, blue

dye has diffused throughout the middle chamber. **(iii)** After 1 h, blue dye has diffused equally into both conduits to create a steady gradient. (**iv**) Proof of concept. Circuits are built around wild-type BMDMs (WT) in the bottom chamber, and those in which the C5a receptor has been knocked out (KO) in the top one. Gradients are established by adding media ± C5a (equivalent to red and blue dyes as in (i)). Movies are collected for 48 h (frames at the start and end shown), trajectories determined; rose plots (n = 3 mice) show biased movement of WT (but not KO) cells towards C5a. **(B)** Increasing throughput with 2-chamber circuit. **(i)** Image of a 6-well plate containing 72 identical circuits (1.5 mm long conduits). Blue dye is added to aid visualisation. (**ii**) Example results. Circuits are built around WT BMDMs contained in the top chambers, and cells are exposed (as in Fig. 2A) to 10 nM C5a added to the bottom chamber ('C5a gradient'), both chambers ('C5a no gradient'), or neither ('media only'). After collecting movies and determining trajectories, NGDRs are calculated (+ SD, n = 3 mice with 3 technical repeats in each setup). Cells in C5a gradients yield the highest NGDRs; one-way ANOVA, statistical significance $p<0.05$. **(C)** Increasing throughput with chambers allowing comparison of up to 4 cell types. **(i)** Cartoon illustrates plates with 6 to 96 wells, and images show a column from each plate. **(ii-v)** In 6- to 48-well plates, circuits have 5 chambers and conduit length decreases as wells become smaller. Four different cell types could be plated in the 4 outer chambers, and attractant in the central one. **(vi)** In the 96-well plate, each circuit has 2 chambers with 1-8 connecting conduits. Insets show zoom of rows 1 and 8.

Active circuits for chemotaxis assays in steady and shifting gradients

Generating defined steady gradients in flowing circuits

The passive circuits described previously have the advantage of being simple to set up and do not require external pumps. However, their concentration gradients change as diffusion drives the system to equilibrium. In contrast, gradients generated by diffusion between two laminar streams (with and without chemoattractant) remain stable and unchanging for as long as flow continues. We now use an 'm'-shaped circuit (**Fig. 1D**) to create a steady concentration gradient of C5a across the central conduit (**Fig. 5A**), with

concentrations determined using the solution to the one-dimensional, time-dependent, diffusion equation in finite media – where $c(x,t) = \frac{c_0}{2} erfc\left(\frac{x}{2\sqrt{Dt}}\right)$ and $t =$ time a molecule spends in the conduit [18]. Flows through fluid-walled conduits can be predicted using a simplified power law [22]; velocities at any point can be determined if the geometry of the conduit footprint, flow rate, and fluid properties of the perfusing medium are known. We thus determine flow velocities to transform the time-dependent diffusion solution into a distance along the device substitution using $t = \frac{x}{u}$, where u is the mean flow velocity at a given x-location.

BMDMs respond to low concentrations of C5a in flow-generated gradients

Media ± 10 nM C5a are infused into left and right arms of the circuit, respectively (**Fig. 5Ai**); their convergence in the central arm and diffusion between laminar streams establishes a gradient of C5a from 0-10 nM across the conduit. Analysis of movie made over 48 h (**Movie 11**) shows that many BMDMs migrate from the left to the centre of the conduit, leaving behind a cell-depleted zone (**Fig. 5Aii**). Cell trajectories and a rose plot confirm such taxis towards C5a (**Fig. 5Aiii**). A theoretical prediction of the gradient is now mapped onto the image taken at 48 h (**Fig. 5Aiv**); the colour map illustrates the normalised local concentration of C5a (from 0 to 1, corresponding to 0-10 nM). Additional concentration curves are overlaid to show some gradient contours; the red one marks half the maximum (i.e., 5 nM), and the left-most one ($c_0 \times 10^{-5} = 0.1$ pM) the left-most edge of the depleted zone – which is the minimum concentration triggering chemotaxis. While a macrophage is typically ~20 µm in diameter [23], cell length increases to more than 100 µm when extending pseudopodia and

moving (**Fig. 5Aii**) so cells in this region can sense a difference in C5a concentration of 1-2 orders of magnitude across their bodies.

BMDM taxis in instantaneously-shifted and continuously-shifted gradients

We next establish a gradient as described above for 24 h, instantaneously shift it 200 µm to the right (by increasing the left-hand input and decreasing the right-hand one, so the overall flow rate does not change; **Fig. S4**), and then maintain a gradient in the new position for 24 h (**Movie 12**). Before the shift, BMDMs migrate into the central zone and form a central band (**Fig. 5Bii**) as described previously. After the shift, the band shifts further to the right, as confirmed by the cell trajectories and rose plot (**Fig. 5Biii,iv**; note the large proportion of blue tracks towards C5a, and enlarged blue segment). These results show that BMDMs can follow this rapid shift in gradient.

We now see if BMDMs follow a continuously-shifting gradient. As before, BMDMs are exposed to a static C5a gradient for 24 h, so that many migrate from the left to the centre (**Fig. 5Ci,ii**). Over the following 24 h, the gradient is shifted continuously rightwards up to 150 µm from the right-hand edge by gradually increasing flow into the left arm and decreasing it into the right one (performed with the 'ramp' function of the pump). Analysis of cell trajectories then reveals that BMDMs do not follow this shifting gradient, and the chemotactic bias observed previously disappears (rose plot in **Fig. 5Ciii**). However, when the gradient remains stationary for an additional 24 h, cells migrate to generate a new band on the right (**Fig. 5Civ**; **Movie 13**). This confirms that cells can still chemotax, but cannot follow a gradient that shifts at the pace used during the middle 24 h.

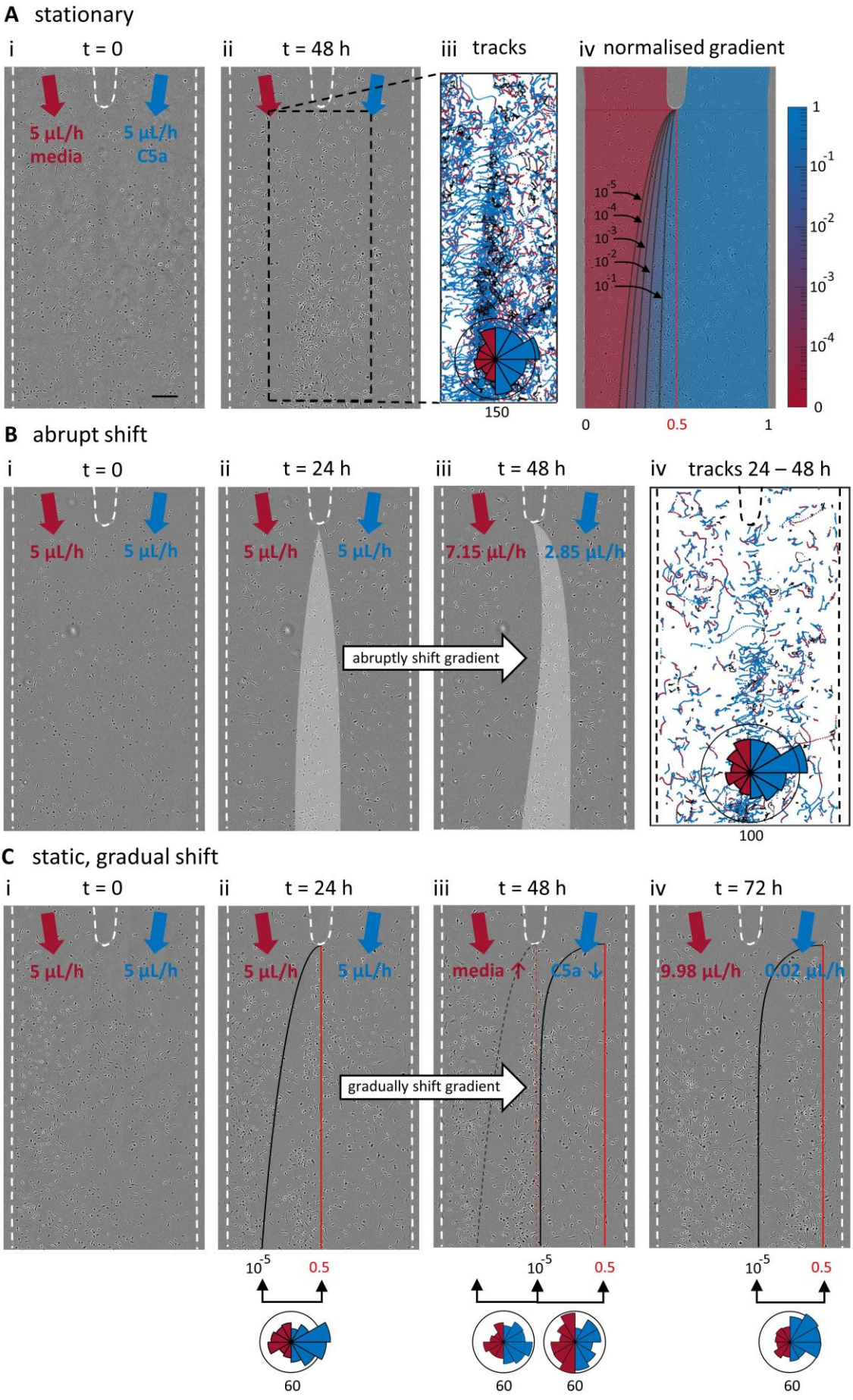

A stationary
i t = 0
ii t = 48 h
iii tracks
iv normalised gradient
5 µL/h media
5 µL/h C5a
150
0
0.5
1
B abrupt shift
i t = 0
ii t = 24 h
iii t = 48 h
iv tracks 24 – 48 h
5 µL/h
5 µL/h
5 µL/h
5 µL/h
7.15 µL/h
2.85 µL/h
abruptly shift gradient
100
C static, gradual shift
i t = 0
ii t = 24 h
iii t = 48 h
iv t = 72 h
5 µL/h
5 µL/h
5 µL/h
5 µL/h
media ↑
C5a ↓
9.98 µL/h
0.02 µL/h
gradually shift gradient
0.5
60

Fig. 5. Chemotaxis in steep C5a gradients held stationary, shifted abruptly to the right, or combinations of the two. BMDMs in the central conduit of 'm'-shaped circuits are exposed to laminar streams of media and media + 10 nM C5a, so diffusion creates a concentration gradient across the conduit. Movies (phase-contrast) are collected of migrating cells as the position of this gradient is changed (either abruptly or steadily) at times indicated by varying input flows into side arms, and cell trajectories plus rose plots (segment length indicates the number of trajectory points per bin) determined (blue towards C5a, red away, black stationary). Scale bar in Ai = 250 µm applies to all panels. Dotted white lines: fluid walls. **(A)** Chemotaxis in a stationary gradient (both input streams constant at 5 µL/h; n = 3 mice). **(i,ii)** Two movie frames illustrating views of central conduit. At t = 0, cells are randomly distributed; after 48 h, some cells have accumulated in a central vertical band (leaving a depleted region behind). **(iii)** Cell trajectories in the region indicated and the overlaid rose plot with the circle indicating the number of trajectories that fall into each bin highlight this chemotaxis. **(iv)** Normalised concentration gradient overlaid on frame at t = 48 h. Contours indicate different C5a concentrations (blue and red: maximum and minimum concentrations corresponding to 10 and 0 nM C5a); the leftmost one labelled 10^{-5} = 0.1 pM marks the left of the depleted region and so the minimum concentration inducing migration. **(B)** Cells continue to chemotax when a gradient established as in (A) after 24 h is abruptly shifted by ~200 µm to the right. **(i-iii)** Movie frames. At t = 24 h, migrating cells are beginning to form a central band (light-grey overlay). Then, changing inputs immediately shifts the gradient to the right (not shown), and by 48 h the cell band is further to the right than in (Aii) (light-grey overlay). **(iv)** Cell trajectories (24-48 h) and overlaid rose plot with the circle indicating number of trajectories falling into each bin confirm cells follow the shifted gradient. **(C)** Partial control of movement by moving gradient position over 72 h. The gradient is static for the first 24 h (equal input flows), then shifts steadily by 750 µm to the right over the next 24 h (by progressively increasing/decreasing flows into left/right inputs), and finally remains static for the last 24 h. **(i-iv)** Movie frames and rose plots with the circle indicating number of trajectories falling into each bin. Cells distributed randomly (t = 0), accumulate at t = 24 h along the centre-line (red) leaving a depleted region behind (just to the right of the black line marking a concentration of 0.1 pM C5a). At t = 48 h, dotted and solid red/black

lines indicate initial and final concentrations of 0.5 nM and 0.1 pM C5a during the intermediate phase when the gradient was shifted continuously; many cells initially in the central band remain roughly in the same position during this phase. At t = 72 h (and so 24 h in a steady gradient after the shift), a new band of cells accumulates close to the right-hand edge of the gradient (red line). Rose plots confirm biased cell movement towards C5a in regions indicated.

Discussion

We describe a general method for studying chemotaxis of cells growing in microfluidic circuits built on standard Petri dishes, and use it to demonstrate mouse macrophages migrating up gradients of C5a, a small peptide released at inflammation sites. Cells are grown in culture medium under a biocompatible and immiscible fluorocarbon (FC40) to limit evaporation, and circuits built in seconds around the living cells by reshaping the two liquids; the aqueous phase and associated cells are confined by fluid walls and ceilings to user-specified regions of the dish (**Fig. 1**) [16]. Concentration gradients of C5a are established by diffusion in both flow-free and flowing environments, and we develop a theoretical model enabling prediction of the C5a concentration at any point. As fluid walls are optically transparent [25], time-lapse movies are made (using a standard imaging system) of cells migrating towards the attractant over days; after determining individual cell trajectories, cell responses are analysed (**Figs 2-5**). The method allows rapid prototyping so users can tune circuit geometry to their specific requirements, and – in principle – migrating cells can be retrieved through the fluid walls for downstream analysis [19], [24].

We first establish the method by imaging cells chemotaxing in the conduit connecting the two chambers in a dumbbell-shaped flow-free circuit. After adding medium into one chamber and C5a into the other, diffusion creates an attractant gradient over cells, and some migrate towards C5a (**Fig. 2**). We then compare responses of cells in different patterns in 4 identical circuits, where cells occupy the whole conduit, or just the top, middle, or bottom third; results are remarkable. Responding cells are the ones closest to the highest C5a concentration, or – to put it in another way – cells distant from the source only respond if there are no others in front of them (**Fig. 3**). Since C5a gradients are identical in all circuits,

this suggests that cells do not respond to a particular range of attractant concentration, as the position of this range will be identical in all 4 gradients – if we assume cells do not distort the gradient. However, as recently demonstrated by Kienle *et al.* [26], neutrophils self-limit their swarming when chemotaxing towards bacteria to improve bacterial elimination efficiency. Perhaps, similarly, macrophages chemotaxing in response to C5a gradients release signals to neighbouring cells to limit and control the overall population response and increase immune efficiency. It would thus be interesting to perform more detailed analyses of the population dynamics involved in the chemotaxis response, for instance by extracting the subpopulation of migrating cells to perform RNA sequencing and compare their genotype with the subpopulation of unbiased cells. Additionally, to investigate the onset of chemotaxis in response to the C5a concentration, it would be interesting to increase the imaging framerate to determine the minimum concentration c_{min} at which cells begin to chemotax.

We next use a 3-chambered circuit to compare responses of C5a-receptor KO and WT BMDMs to C5a gradients emanating from one central C5a chamber; WT cells chemotax normally, as KO ones do not (**Fig. 4A**). We also increase throughput by building various circuits, including 12 dumbbells in each well of a 6-well plate (**Fig. 4Bi**), 5-chambered circuits in each well of a 6-, 12-, 24- and 48-well plate, and 2-chambered circuits connected by 1-8 conduits in each well of a 96-well plate (**Fig. 4C**).

Dynamic systems are then implemented in ‘m’-shaped circuits, and used to study the response of BMDMs to steep gradients of C5a. Using our theoretical model, we alter the flow rate ratio of the input streams to instantly shift the gradient by a fixed distance and show that cells move to the new location. To assess whether cells follow a gradient shifting

uninterruptedly, we continuously move the gradient from the centre of the conduit to the right-hand wall (750 µm) over 24 h; interestingly, cells do not follow the gradient during this transient phase. Instead, once the gradient reaches steady-state near the wall, a new band of cells migrates and accumulates in this region. Why then do cells not respond during the transient phase of the gradient shifting? The gradient is shifted by 750 µm in 24 h, corresponding to a shift speed of ~0.5 µm/min, or half the average velocity of a macrophage [27]. BMDMs should therefore be able to follow the gradient as it moves along the width of the conduit. However, as the gradient moves, the concentration at the front of a cell decreases (while a concentration gradient across the entire cell body remains); perhaps then do cells in the gradient observe this time-varying concentration at their leading edge (decreasing in the direction of the shift), and as a result do not chemotax. In contrast, once the gradient reaches its final position near the wall after the initial 48 h period, cells migrate again as the concentration distribution reaches steady-state. It is commonly accepted that eukaryotic cells regulate their response to concentration gradients by spatial sensing [28]. However, it was recently shown that migrating myeloid cells (dendritic cells and neutrophils) sense temporal dynamics of chemoattractant concentrations and respond to rising concentrations of CCL19 and CXCL12 by migrating further than in stable gradients of these chemokines (while transiently rising and stable gradients of C5a lead to the same response) [29]. Additionally, neutrophils were shown to migrate towards moving gradients of interleukin-8 that follow step changes (instantaneous rather than continuous shifts) [30]. While these results indicate the ability of myeloid cells to spatiotemporally sense changing concentrations of chemoattractants and follow instantly-shifted gradients, they fail to capture the unique combination of continuously-moving gradients that temporally decrease the chemoattractant concentration at the side of the cell facing the higher concentration,

whilst maintaining a concentration gradient over the cell. Our findings suggest that macrophages spatiotemporally sense varying concentrations of C5a, and appear to limit chemotaxis when gradients are moved continuously away, leading to decreasing concentrations of C5a at the leading end of the cell. However, when gradients are moved instantly, this temporal effect is eliminated and cells continue to migrate up the concentration gradient.

Altogether, this method seeks to address limitations of current chemotaxis assays, allowing users to generate stable gradients, track individual cells, distinguish between chemotaxis and chemokinesis, perform higher-throughput assays in both Petri dishes and well plates, observe and isolate cells of interest in real-time for downstream analysis, pattern cells in unique configurations, and study the response of diverse cell populations in unique circuits without requiring additional cell labels. **Table 2** summarises the advantages offered by fluid-walled circuits and compares them to more traditional chemotaxis platforms such as transwell assays, cell tracking chambers, under-agarose assays and conventional microfluidic systems. We thus hope that this study will serve as a blueprint for future chemotaxis studies, offering new methods to evaluate population dynamics and cell-cell signalling of chemotaxing macrophages, and to elaborate on the temporal sensing mechanisms involved in chemotaxis of myeloid cells. We additionally anticipate that the technique will increase uptake of microfluidics in biomedical labs and contribute to further expand and improve the field of chemotaxis.

Table 2. Comparing traditional and fluid-walled chemotaxis assays

Assay	Transwell assays	Direct observation and cell tracking chambers	Under agarose assays	Traditional microfluidic assays	Fluid-walled microfluidics
Stable gradients	+ [31]	+/- [5], [31]	-	+ [32], [33]	+ [19]
Single cell tracking	-	+ [26], [34]	+ [26]	+ [32], [33]	+ [25], [35]
Fugetaxis detection	+ [36], [37]	-	+ [38]	+ [39]	+
Distinction between chemotaxis and chemokinesis	+ [40]	+ [34], [41]	+/- [42]	+ [32], [33]	+
High throughput	+/- [43], [44]	-	-	+ [11], [45]	+
Specialised equipment	+/- [4], [44]	-	-	+ [32], [33]	+/-
Real-time observation	+/- [4]	+ [34], [41]	+ [26], [42]	+ [32], [33]	+ [19]
Multiple cell types	-	-	+/- [42]	+/- [45]	+
Patterning cells	-	-	-	+/- [32]	+
Multiple chemoattractants	-	-	+ [42]	+ [32], [45]	+
Cell isolation / circuit reconfiguration	-	-	-	-	+ [19], [24]
Targeted live cell recovery	-	-	-	-	+ [19]

Materials and Methods

Strains, media, culture conditions and reagents

To obtain BMDMs, bone marrow is extracted from femurs and tibia of mice (C57BL/6, Balb/c or 5ar1tm1Cge/J on Balb/c background – a C5a KO; C57BL/6 were bred in Pathology Support Building University of Oxford, and Balb/c WT plus the C5aR KO were bought from the Jackson Laboratory) and frozen for up to 6 months in -80^{o}C. Upon defrosting the bone marrow is cultured for 7 days (37°C, 5% CO_2) in high-glucose Dulbecco's Modified Eagle's Medium (DMEM, Sigma) enriched with 10% L929-conditioned media (containing macrophage colony-stimulating factor), 10% Fetal Bovine Serum (FBS, Sigma) and 1% penicillin plus streptomycin (P/S, Gibco); as this combination is used throughout the study, we refer to the mixture simply as 'media'. 8 mL media is used for the first 4 d; then, 3 mL is removed and replaced with 5 mL fresh media. Cells are plated on dishes on day 6, circuits built around them on the same day for passive circuits and on the next day for active circuits, and chemoattractants added on day 7.

Experiments with cells are performed in 35 mm Petri dishes (Corning, 430165) and 6-well plates (Corning, 3516). We additionally use a various other plates (12 to 96-wellplates, Corning) for higher-throughput applications. In all chemotaxis assays, we use recombinant mouse complement component 5a (C5a, 10 nM; R&D Systems).

Imaging

BMDMs are imaged at a rate of 3 frames/h (for experiments in dishes) or 2 frames/h (for experiments in plates) using an IncuCyte ZOOM, a live-cell imaging system (Sartorius, Gottingen, Germany). The IncuCyte is itself contained in an incubator (37°C, 5% CO_2).

Printing circuits

In all experiments, cells are first plated on either Petri dishes or well plates, and – after attaching to the substrate – the circuit is jetted around the cells. Cell plating and circuit printing are performed on custom-made three-axis traverses (iotaSciences Ltd, Oxford, UK); we refer to these as a 'printer' for circuits made on Petri dishes, and a larger 'pro-printer' for circuits made on well plates.

Loading and patterning cells

Cells are first plated on the dish using the printer as described previously [16]. Briefly, the three-axis arm of the printer holds a dispensing needle (25G, Adhesive Dispensing Ltd) connected by PTFE tubing (Cole-Parmer) to a 250 µL glass syringe (Hamilton) controlled by a syringe pump (iotaSciences Ltd). The needle is brought 300 µm above the dish surface and begins to infuse a solution of BMDMs suspended in media + 2% Fibronectin (Sigma, F1141; 1 million cells/mL). The needle is then moved over the surface of the dish to deposit the cell mixture in the desired pattern. After printing, the dish is placed in an incubator for 5 minutes to allow cells to settle and attach to the surface.

Jetting circuits

The dish is now removed from the incubator and 1 mL of media is gently pipetted over the cells to wet the entire dish. Most of the media is removed, and 1 mL of FC40 is pipetted to cover the remaining thin film of media. The dish is placed back onto the printer and a second needle loaded with FC40 begins to jet a stream of FC40 500 µm above the surface of the dish. When this jet contacts the surface, it displaces the underlying media, and – as FC40 wets polystyrene better than water – it replaces media to form a fluid wall (a medium:FC40

interface). The needle is then moved over the dish and around cells to create fluid walls that form the footprint of the circuit [16]. For passive circuits, 1 µL of media is added to each chamber after jetting the circuit.

Circuit design

We design two types of circuit, static (passive) circuits without flow, and dynamic (active) ones with flow. The first passive circuits used are dumbbell shaped and consist of two square chambers (footprints 2.5 x 2.5 mm) connected by a thin conduit (600 µm wide, 1.5 mm long). Circuits are built around cells so that those cells end up just within the top chamber, within the top chamber + conduit, or in bands at different positions in the conduit. The chemoattractant (C5a) is then added to the bottom chamber. For these experiments, 12 circuits are printed in each dish (**Fig. 1C**). Cells in different locations of the circuit grow under different heights of media due to the curved profile of the overlying fluid interface, and this might affect cell behaviour; therefore, we tracked cells growing at different positions throughout static circuits in media or a uniform distribution of C5a (i.e., without a gradient), and find that average cell velocities are unaffected by position in the circuit (**Fig. S6**).

For cell-comparison studies (**Fig. 4A**), we use a slightly modified version of the passive circuit by connecting three chambers (also 2.5 mm wide) to two conduits (600 µm wide, 1.5 µm long). Due to larger circuit sizes, 6 circuits are printed in each individual dish.

For flow-generated gradients, we use ‘m’-shaped circuits similar to previous studies [19]. These circuits consist of two arms that join into a conduit that ends in a large circular

sink (7 mm wide). Cells grow in the central conduit (6 mm long, 1.8 mm wide), and side arms are used to perfuse media or media + C5a.

Generating stable concentration gradients

Passive circuit

As described previously, reagents are loaded using the printer, and dishes are subsequently moved onto the IncuCyte for imaging. Loading is performed by matching reagent volumes to ensure that C5a remains in the bottom chamber and does not flow into the conduit. To achieve this, pressure in the C5a chamber is kept lower than the media chamber during loading, so media flows into the C5a chamber until the system reaches equilibrium and then diffusion can create a steady gradient down the conduit. This is done by first infusing 1 µL of media into the top chamber, and then 0.5 µL of C5a in the bottom chamber. After loading all 12 circuits, the dish is gently moved from printer to incubator (to not cause sudden flows of C5a) and placed inside the IncuCyte for imaging.

Active circuit

Gradients in active circuits are generated as in previous studies [19]. Briefly, two 500 µL glass syringes (Hamilton) are loaded with either media or media + 10 nM C5a, placed on a syringe pump (Harvard Apparatus), and connected to needles via PTFE tubing. Using a 3D-printed adaptor that fits around the edge of the dish and holds the needles, needles are inserted into each arm of the circuit (left – media, right – C5a). A third needle – also connected to a 1 mL glass syringe (Hamilton) on a separate syringe pump and held in the adaptor – is inserted into the sink. The first two needles are then set to infuse (at the rates indicated in **Fig. 5**; total flow rate in the conduit is always 10 µL/h), while the third needle withdraws at

an equivalent flow rate (10 µL/h). The circuit is overlaid with an additional 4 mL of FC40, and placed inside the IncuCyte to begin imaging.

Determining the diffusion coefficient of C5a

In both types of circuits, we use theoretical models to predict local concentrations and gradient steepness across conduits. The models use well-known solutions to the one-dimensional diffusion equation (**Supplementary Information**) that require the diffusion coefficient of C5a to be known. We thus determine D_{c5a} using the Stokes-Einstein equation for the diffusion of a spherical particle in water of radius r as $D = \frac{k_B T}{6\pi\eta r}$ ($k_B =$ Boltzmann's constant, $T =$ absolute temperature, $\eta =$ dynamic viscosity). The Stokes radius of a C5a molecule is first determined using its molecular weight, $MW_{c5a} = 9$ kDa, as $r = 1.82$ nm. Then, using $\eta_{water} = 0.7$ cP and $T = 310.15$ K (37°C), we find $D_{c5a} = 1.8 \times 10^{-10}$ m^2/s.

Image analysis

To analyse and quantify migration of individual macrophages, we track thousands of cells using a custom-made particle-tracking algorithm in Fiji. Briefly, bright-field images are extracted, stabilised, the median background intensity subtracted, and particle locations recorded. Analyses of trajectories to quantify cell velocities, NGDR, and chemotactic bias are then performed in Matlab as previously described [19].

xCELLigence chemotaxis assay

Real-time xCELLigence chemotaxis assays are performed as previously described [4]. Briefly, CIM-16 plates are used in RTCA-DP instrument (Agilent, Santa Clara, USA).

Experimental concentrations (0.03 nM – 300 nM) of C5a are re-suspended in chemotaxis buffer (RPMI-1640 + 25 mM HEPES solution + 0.5% bovine serum albumin) and 160 µL of pure chemotaxis media or the C5a solution are placed in the bottom chamber of the CIM-16 plates. The top insert is then attached and 50 µL of pure chemotaxis buffer are added to the top chamber; the plates are left in the incubator for 30 min to allow gradient formation. BMDMs are re-suspended at $2x10^6$ cells per mL in the chemotaxis buffer. After 30 min a blank recording is taken and 50 µL of the BMDM suspension is added to the top chamber. Cells are left at room temperature for 10 min to attach after which the recording starts, and measurements are taken every 40 seconds. RPMI-1640 was bought from Gibco, HEPES solution and bovine serum albumin were bought from Sigma.

References

[1] X. Yang, D. Dormann, A. E. Münsterberg, and C. J. Weijer, "Cell Movement Patterns during Gastrulation in the Chick Are Controlled by Positive and Negative Chemotaxis Mediated by FGF4 and FGF8," *Dev. Cell*, vol. 3, no. 3, pp. 425–437, 2002, doi: https://doi.org/10.1016/S1534-5807(02)00256-3.

[2] Y. V Bobryshev, E. A. Ivanova, D. A. Chistiakov, N. G. Nikiforov, and A. N. Orekhov, "Macrophages and Their Role in Atherosclerosis: Pathophysiology and Transcriptome Analysis," *Biomed Res. Int.*, vol. 2016, p. 9582430, 2016, doi: 10.1155/2016/9582430.

[3] S. Boyden, "The chemotactic effect of mixtures of antibody and antigen on polymorphonuclear leucocytes," *J. Exp. Med.*, vol. 115, no. 3, pp. 453–466, Mar. 1962, doi: 10.1084/jem.115.3.453.

[4] A. J. Iqbal *et al.*, "A Real Time Chemotaxis Assay Unveils Unique Migratory Profiles amongst Different Primary Murine Macrophages," *PLoS One*, vol. 8, no. 3, p. e58744, Mar. 2013, [Online]. Available: https://doi.org/10.1371/journal.pone.0058744.

[5] D. Zicha, G. A. Dunn, and A. F. Brown, "A new direct-viewing chemotaxis chamber.," *J. Cell Sci.*, vol. 99 (Pt 4), pp. 769–775, Aug. 1991.

[6] F. Vianello, E. Righi, and M. C. Poznansky, "Methods for Quantitation of Leukocyte Chemotaxis and Fugetaxis," in *T-Cell Trafficking: Methods and Protocols*, F. M. Marelli-Berg and S. Nourshargh, Eds. Totowa, NJ: Humana Press, 2010, pp. 115–124.

[7] H. Harris, "Role of Chemotaxis in Inflammation," *Physiol. Rev.*, vol. 34, no. 3, pp. 529–562, Jul. 1954, doi: 10.1152/physrev.1954.34.3.529.

[8] W. Zhao, H. Zhao, M. Li, and C. Huang, "Microfluidic devices for neutrophil chemotaxis studies," *J. Transl. Med.*, vol. 18, no. 1, p. 168, 2020, doi: 10.1186/s12967-020-02335-7.

[9] D. Irimia, "Microfluidic Technologies for Temporal Perturbations of Chemotaxis," *Annu. Rev. Biomed. Eng.*, vol. 12, no. 1, pp. 259–284, Jul. 2010, doi: 10.1146/annurev-bioeng-070909-105241.

[10] C. Frick *et al.*, “Nano-scale microfluidics to study 3D chemotaxis at the single cell level,” *PLoS One*, vol. 13, no. 6, p. e0198330, Jun. 2018, [Online]. Available: https://doi.org/10.1371/journal.pone.0198330.

[11] Z. Xu *et al.*, “High-throughput three-dimensional chemotactic assays reveal steepness-dependent complexity in neuronal sensation to molecular gradients,” *Nat. Commun.*, vol. 9, no. 1, p. 4745, 2018, doi: 10.1038/s41467-018-07186-x.

[12] M. Samandari, L. Rafiee, F. Alipanah, A. Sanati-Nezhad, and S. H. Javanmard, “A simple, low cost and reusable microfluidic gradient strategy and its application in modeling cancer invasion,” *Sci. Rep.*, vol. 11, no. 1, p. 10310, 2021, doi: 10.1038/s41598-021-89635-0.

[13] E. Berthier, E. W. Young, and D. Beebe, “Engineers are from PDMS-land, Biologists are from Polystyrenia,” *Lab Chip*, vol. 12, no. 7, pp. 1224–1237, 2012, doi: 10.1039/c2lc20982a.

[14] S. Halldorsson, E. Lucumi, R. Gómez-Sjöberg, and R. M. T. Fleming, “Advantages and challenges of microfluidic cell culture in polydimethylsiloxane devices,” *Biosens. Bioelectron.*, vol. 63, pp. 218–231, 2015, doi: https://doi.org/10.1016/j.bios.2014.07.029.

[15] E. J. Walsh *et al.*, “Microfluidics with fluid walls,” *Nat. Commun.*, vol. 8, no. 1, p. 816, 2017, doi: 10.1038/s41467-017-00846-4.

[16] C. Soitu, N. Stovall-Kurtz, C. Deroy, A. A. Castrejón-Pita, P. R. Cook, and E. J. Walsh, “Jet-Printing Microfluidic Devices on Demand,” *Adv. Sci.*, 2020, doi: 10.1002/advs.202001854.

[17] R. R. Kew, “The Complement System,” in *Pathobiology of Human Disease*, L. M. McManus and R. N. B. T.-P. of H. D. Mitchell, Eds. San Diego: Academic Press, 2014, pp. 231–243.

[18] J. Crank, *The Mathematics of Diffusion*. (Clarendon Press, Oxford), 1975.

[19] C. Deroy *et al.*, “Reconfiguring microfluidic circuits to isolate and retrieve cells of interest,” (Manuscript in Preparation), 2021.

[20] N. M. Oliveira, K. R. Foster, and W. M. Durham, “Single-cell twitching chemotaxis in developing biofilms,” *Proc. Natl. Acad. Sci.*, vol. 113, no. 23, pp. 6532 LP – 6537, Jun. 2016, doi: 10.1073/pnas.1600760113.

[21] R. R. Kay, P. Langridge, D. Traynor, and O. Hoeller, “Changing directions in the study of chemotaxis,” *Nat. Rev. Mol. Cell Biol.*, vol. 9, no. 6, pp. 455–463, 2008, doi: 10.1038/nrm2419.

[22] C. Deroy, N. Stovall-Kurtz, F. Nebuloni, C. Soitu, P. R. Cook, and E. J. Walsh, “Predicting flows through microfluidic circuits with fluid walls,” *(Manuscript Submitt.*, 2021.

[23] D. A. Guertin and D. M. Sabatini, “Cell Size Control,” *eLS*. Jan. 27, 2006, doi: https://doi.org/10.1038/npg.els.0003359.

[24] C. Soitu, A. Feuerborn, C. Deroy, A. A. Castrejón-Pita, P. R. Cook, and E. J. Walsh, “Raising fluid walls around living cells,” *Sci. Adv.*, vol. 5, no. 6, 2019, doi: 10.1126/sciadv.aav8002.

[25] C. Soitu, C. Deroy, A. A. Castrejón-Pita, P. R. Cook, and E. J. Walsh, “Using Fluid Walls for Single-Cell Cloning Provides Assurance in Monoclonality,” *SLAS Technol.*, 2019, doi: 10.1177/2472630319891135.

[26] K. Kienle *et al.*, “Neutrophils self-limit swarming to contain bacterial growth in vivo,” *Science (80-.).*, vol. 372, no. 6548, p. eabe7729, Jun. 2021, doi: 10.1126/science.abe7729.

[27] F. J. Pixley, “Macrophage Migration and Its Regulation by CSF-1,” *Int. J. Cell Biol.*, vol. 2012, p. 501962, 2012, doi: 10.1155/2012/501962.

[28] C. A. Parent and P. N. Devreotes, “A Cell’s Sense of Direction,” *Science (80-.).*, vol. 284, no. 5415, pp. 765 LP – 770, Apr. 1999, doi: 10.1126/science.284.5415.765.

[29] C. E. Petrie Aronin *et al.*, “Migrating Myeloid Cells Sense Temporal Dynamics of Chemoattractant Concentrations,” *Immunity*, vol. 47, no. 5, pp. 862-874.e3, Nov. 2017, doi: 10.1016/j.immuni.2017.10.020.

[30] M. A. Qasaimeh, M. Pyzik, M. Astolfi, S. M. Vidal, and D. Juncker, “Neutrophil Chemotaxis in Moving Gradients,” *Adv. Biosyst.*, vol. 2, no. 7, p. 1700243, Jul. 2018, doi: https://doi.org/10.1002/adbi.201700243.

[31] D. A. Lauffenburger and S. H. Zigmond, “Chemotactic factor concentration gradients in chemotaxis assay systems.,” *J. Immunol. Methods*, vol. 40, no. 1, pp. 45–60, 1981, doi:

10.1016/0022-1759(81)90079-x.

[32] J. Schwarz *et al.*, “A microfluidic device for measuring cell migration towards substrate-bound and soluble chemokine gradients,” *Sci. Rep.*, vol. 6, no. 1, p. 36440, 2016, doi: 10.1038/srep36440.

[33] E. van den Bos, S. Walbaum, M. Horsthemke, A. C. Bachg, and P. J. Hanley, “Time-lapse Imaging of Mouse Macrophage Chemotaxis,” *JoVE*, no. 158, p. e60750, 2020, doi: doi:10.3791/60750.

[34] A. P. Wheeler *et al.*, “Rac1 and Rac2 regulate macrophage morphology but are not essential for migration.,” *J. Cell Sci.*, vol. 119, no. Pt 13, pp. 2749–2757, Jul. 2006, doi: 10.1242/jcs.03024.

[35] C. Soitu *et al.*, “Microfluidic chambers using fluid walls for cell biology,” *Proc. Natl. Acad. Sci.*, 2018, doi: 10.1073/pnas.1805449115.

[36] P. Ogilvie, S. Paoletti, I. Clark-Lewis, and M. Uguccioni, “Eotaxin-3 is a natural antagonist for CCR2 and exerts a repulsive effect on human monocytes,” *Blood*, vol. 102, no. 3, pp. 789–794, Aug. 2003, doi: 10.1182/blood-2002-09-2773.

[37] P. M. Cano, A. Vargas, and J.-P. Lavoie, “A real-time assay for neutrophil chemotaxis.,” *Biotechniques*, vol. 60, no. 5, pp. 245–251, 2016, doi: 10.2144/000114416.

[38] J. E. Phillips and R. H. Gomer, “A secreted protein is an endogenous chemorepellant in Dictyostelium discoideum,” *Proc. Natl. Acad. Sci.*, vol. 109, no. 27, pp. 10990 LP – 10995, Jul. 2012, doi: 10.1073/pnas.1206350109.

[39] W. G. Tharp *et al.*, “Neutrophil chemorepulsion in defined interleukin-8 gradients in vitro and in vivo.,” *J. Leukoc. Biol.*, vol. 79, no. 3, pp. 539–554, Mar. 2006, doi: 10.1189/jlb.0905516.

[40] H. M. Buettner, D. A. Lauffenburger, and S. H. Zigmond, “Measurement of leukocyte motility and chemotaxis parameters with the Millipore filter assay.,” *J. Immunol. Methods*, vol. 123, no. 1, pp. 25–37, Sep. 1989, doi: 10.1016/0022-1759(89)90026-4.

[41] W. E. Allen, D. Zicha, A. J. Ridley, and G. E. Jones, “A role for Cdc42 in macrophage

chemotaxis," *J. Cell Biol.*, vol. 141, no. 5, pp. 1147–1157, Jun. 1998, doi: 10.1083/jcb.141.5.1147.

[42] Y. Mousseau *et al.*, "Improved agarose gel assay for quantification of growth factor-induced cell motility," *Biotechniques*, vol. 43, no. 4, pp. 509–516, Oct. 2007, doi: 10.2144/000112557.

[43] W. Falk, R. H. J. Goodwin, and E. J. Leonard, "A 48-well micro chemotaxis assembly for rapid and accurate measurement of leukocyte migration.," *J. Immunol. Methods*, vol. 33, no. 3, pp. 239–247, 1980, doi: 10.1016/0022-1759(80)90211-2.

[44] L. Taylor, M. H. Brodermann, D. McCaffary, A. J. Iqbal, and D. R. Greaves, "Netrin-1 Reduces Monocyte and Macrophage Chemotaxis towards the Complement Component C5a," *PLoS One*, vol. 11, no. 8, p. e0160685, Aug. 2016, [Online]. Available: https://doi.org/10.1371/journal.pone.0160685.

[45] J. Wu, A. Kumar-Kanojia, S. Hombach-Klonisch, T. Klonisch, and F. Lin, "A radial microfluidic platform for higher throughput chemotaxis studies with individual gradient control.," *Lab Chip*, vol. 18, no. 24, pp. 3855–3864, Dec. 2018, doi: 10.1039/c8lc00981c.

Supplementary Information

Determining concentration gradients in passive circuits

The dumbbell-shaped passive circuits consist of two square chambers connected by a thin conduit (**Materials and Methods**). Shortly after adding C5a in the bottom chamber the system reaches equilibrium (no pressure gradient) and diffusion creates a concentration gradient of C5a across the conduit. Diffusion is described by Fick's second law as $\frac{\partial c}{\partial t} = D\frac{\partial^2 c}{\partial x^2}$ ($c =$ concentration, $t =$ time, $x =$ distance, $D =$ diffusion coefficient). The concentration gradient in the conduit is expressed by the solution to the one-dimensional diffusion equation for a semi-infinite medium with constant concentration c_0 at the boundary [18]:

$$c(x,t) = c_0 erfc\left(\frac{x}{2\sqrt{Dt}}\right) \qquad (S1)$$

From Eq. S1, we determine the time for the system to reach steady state, which we define as 15% of the initial concentration c_0 reaching the end of the conduit, $t_{SS} = \frac{x^2}{4D \times erfc^{-1}(0.15)}$, with $x =$ conduit length. After this time, the gradient is linear and set to vary from 0 to 10 nM. We then assess how long concentration gradients remain stable to determine maximum experimental runtimes, t_{end}. We define t_{end} as the time taken for the concentration in the media chamber to reach 5% of the initial concentration c_0 in the C5a-free chamber where it becomes evenly distributed ($c_{end} = 0.05 \times c_0 \; @ \; t_{end}$). To evaluate t_{end}, we determine the rate of mass transfer through a conduit using Fick's first law of diffusion which gives:

$$\dot{m} = -DA\frac{dc}{dx} \qquad (S2)$$

Hence once we know the mass of C5a to be transferred, we determine t_{end} as:

$$t_{end} = 1.05\frac{x_{conduit}\, m_{c5a_{transferred}}}{DA_{conduit}c_0} \qquad (S3)$$

The cross-sectional area of the conduit, $A_{conduit}$, is now determined to find t_{end}. As the system is static, Laplace pressure (ΔP) in the circuit is equal everywhere such that $\Delta P_{chamber} = \Delta P_{conduit}$, with $\Delta P_{chamber} = \frac{2\gamma}{R_{chamber}}$ and $\Delta P_{conduit} = \frac{\gamma}{R_{conduit}}$ (R = radius of curvature); thus, $R_{chamber} = 2R_{conduit}$ (**Fig. S1**).

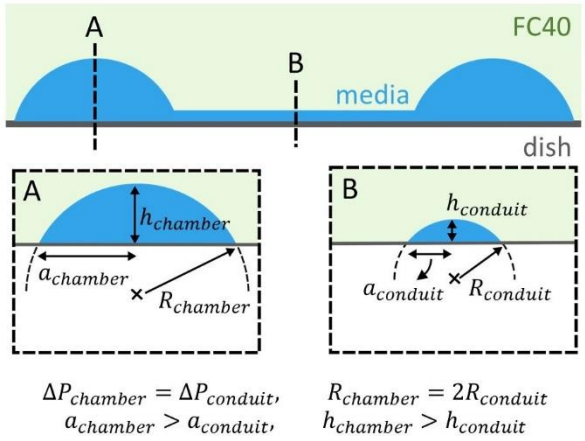


Fig. S1. Geometrical properties of passive circuits. The top panel illustrates a side view of a dumbbell circuit consisting of two large chambers with spherical caps connected by a thin conduit. The bottom-left panel shows the cross-sectional profile of the chamber at A, while the bottom-right panel illustrates the conduit cross-section at B.

Heights of sessile drops are determined by their volume using $V = \frac{\pi h}{6}(3a^2 + h^2)$ [15]. To determine heights in chambers with square footprints (as in our circuits), we assume their pressure is equivalent to circular chambers with the same radius a. Thus, rearranging the terms of the previous equation:

$$h_{chamber} = \frac{\left(\sqrt{\pi^2 a_{chamber}^6 + 9V_{chamber}^2} + 3V_{chamber}\right)^{\frac{2}{3}} - \pi^{\frac{2}{3}} a_{chamber}^2}{\sqrt[3]{\pi}\sqrt[3]{\sqrt{\pi^2 a_{chamber}^6 + 9V_{chamber}^2} + 3V_{chamber}}}$$

Since $R_{chamber} = 2R_{conduit}$ and $R = \frac{a^2+h^2}{2h}$, $h_{conduit}$ is expressed in terms of $h_{chamber}$ as:

$$h_{conduit} = \frac{{a_{chamber}}^2 + {h_{chamber}}^2 - \sqrt{{a_{chamber}}^4 + {h_{chamber}}^4 - 16{a_{conduit}}^2{h_{chamber}}^2 + 2{a_{chamber}}^2{h_{chamber}}^2}}{4h_{chamber}}$$

To validate our assumption, we measure $h_{conduit}$ in passive circuits with square and circular chambers of equivalent radii, $a_{chamber}$, using fluorescent beads as described in a previous study [22]. Using $V_{chamber} = 1.75$ µL (the volume used in this study), we find good agreement between theoretical and measured heights (i.e., $h_{conduit,\ theoretical} = 65$ µm, $h_{conduit,\ square} = 65.7 \pm 6$ µm, $h_{conduit,\ circular} = 68.6 \pm 2$ µm). We then calculate steady-state and maximum experimental runtimes for circuits of varying lengths, summarised in **Table S1**:

Table S1. Steady-state times and maximum runtimes in passive circuits

Conduit length (mm)	1.5	2	3	4	5	6	7
t_{SS} (h)	0.9	1.5	3.4	6	9.5	13.6	18.6
t_{end} (d)	11.5	15	23	30	38	45	53

Dose-response of BMDMs to C5a

To determine the concentration of C5a eliciting the strongest migration response, we perform xCELLigence chemotaxis assays to establish a dose-response curve. Concentrations ranging 0.03 – 300 nM C5a are tested and results plotted in **Figure S2**. From these measurements, we find that 10 nM C5a elicits the strongest response, and thus this concentration is used throughout our microfluidic experiments.

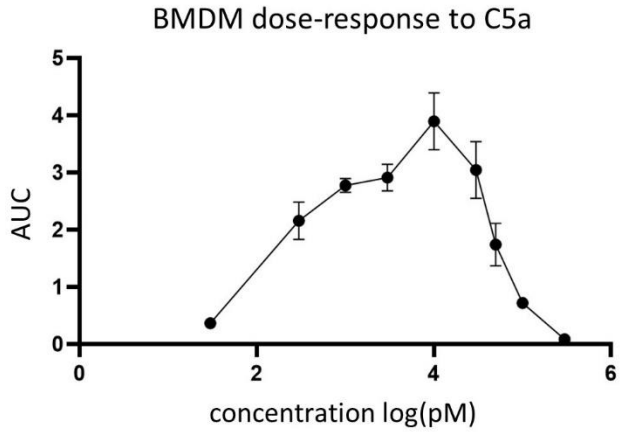


Fig. S2. BMDM dose-response to C5a. A real-time xCELLigence assay (modified Boyden chamber) is used to perform dose-response measurements of BMDMs to concentrations of C5a ranging from 0.03 – 300 nM. The area under the curve (AUC) is quantified for the cell impedance measurements collected every 40 seconds over 4 hours (n = 3-6 biological repeats per each concentration).

Determining chemotaxis onset in passive circuits

To determine the onset of chemotaxis, we analyse morphological changes in BMDMs that are characteristic of cell migration. As BMDMs extend pseudopodia to move across surfaces and sense chemical stimuli, we determine the time required for these pseudopodia to become apparent around cells (**Fig. S3**). This time then provides a window during which cells are activated, and corresponding concentrations and gradient strengths are determined using the distance of cells to the C5a chamber.

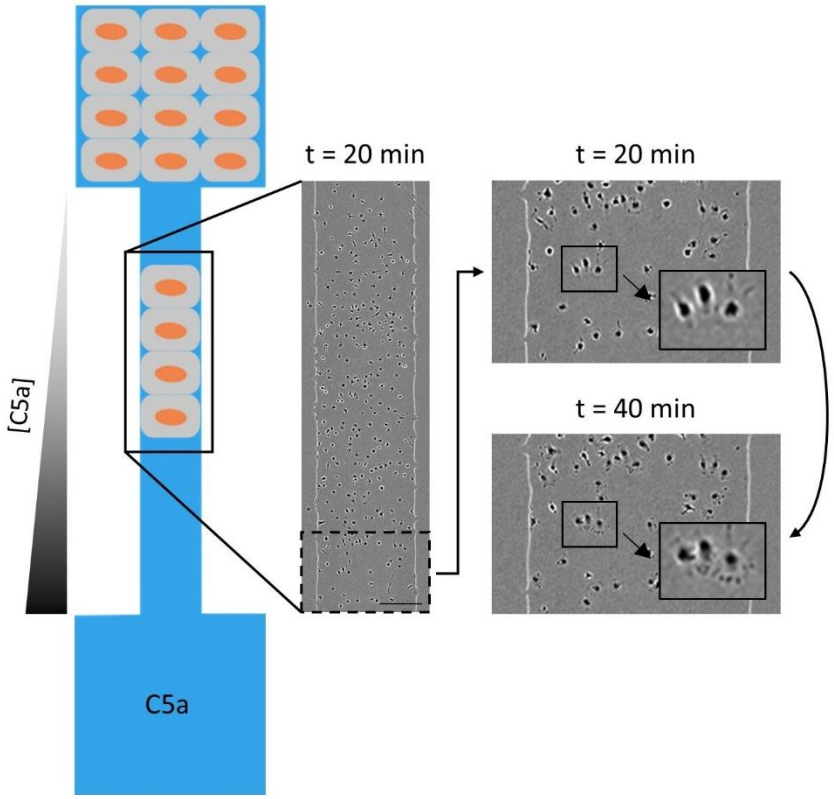


Fig. S3. Chemotaxis onset in passive circuits. The cartoon (left) shows the experimental setup in Fig. 4iii. The central image is from the first frame in the movie (t = 20 min after addition of C5a) and shows the part of the conduit containing cells. Inset at top right illustrates a close-up of cells that will chemotax over the

next 2 days; they are mostly round. Inset at bottom right shows the same region in the next frame (t = 40 min); pseudopodia are now visible extending from rounded cell bodies. Scale bar: 250 μm.

Determining concentration gradients in active circuits

To predict concentration gradients in active circuits, we use the solution to the one-dimensional diffusion equation in which the initial distribution of diffusing substance occupies a finite region and the initial state is defined by $c = c_0, x < 0, c = 0, x > 0, t = 0$, given by [18]:

$$c(x,t) = \frac{c_0}{2} erfc\left(\frac{x}{2\sqrt{Dt}}\right) \qquad (S4)$$

In this case, time is transformed into distance along the conduit using the mean flow velocity. Unlike traditional microfluidic devices with fixed geometries, fluid-walled conduits have flexible interfaces that morph with changes in pressure; as a result, conduit height decreases in the flow direction due to decreasing pressure. Furthermore, conduits have circular cross-sections (**Fig. S4A**). Thus, the average velocity in a conduit will vary as a function of conduit length, x, and conduit width, z [22]. In order then to predict the shape of the concentration gradient in conduits where streams meet along the conduit centreline (i.e., $Q_1 = Q_2$, **Fig. S4Bi**), we determine the average velocity, u_{mean}, along the centreline (red line in **Fig. S4Bi**) over the entire conduit length (in increments $\Delta x = 6$ μm). From these values, we infer the time t a particle spends in the conduit at a given x-location as $t = \frac{x}{u_{mean}}$ and substitute this in Eq. S4 to obtain the local concentration.

As discussed in **Figure 5**, gradients can be shifted by varying the ratio of flow rate between input streams Q_1 and Q_2 (**Fig. S4B**). Using the previously established semi-analytical solution to predict conduit heights in flowing systems [22], we now apply the solution to determine flow rate ratios required to shift gradients by a fixed distance (red line in **Fig. S4Bii**). First, using the total flow rate in the conduit (i.e., $Q_{total} = Q_1 + Q_2$; in this study we set $Q_{total} = 10$ µL/h), we determine the maximum conduit height, h_{max}, and velocity, u_{max}, for a conduit of length L using $h_{max} = \left(\frac{26.08 Q_{total} \mu a L}{\gamma}\right)^{0.25}$ and $u_{max} = \frac{Q_{total}}{0.61 h_{max} a}$ (μ = viscosity, a = conduit half-width, γ = interfacial tension). Since Q_{total} can be expressed in terms of h_{max} and u_{max} as $Q_{total} = \frac{2}{3}\frac{u_{max}}{h_{max}^2}\int_0^{2a} h_z^3 dz$, where h_z corresponds to height across the conduit width, we next determine Q_1 and Q_2 to position the gradient at location s across the width of the conduit using:

$$Q_1 = \frac{2}{3}\frac{u_{max}}{h_{max}^2}\int_0^{s} h_z^3 dz \qquad (S5)$$

$$Q_2 = \frac{2}{3}\frac{u_{max}}{h_{max}^2}\int_s^{2a} h_z^3 dz \qquad (S6)$$

Thus, the position of the gradient can be shifted to any location across the conduit using these sets of equations to determine the necessary flow rate ratios. Note that the same principle can also be applied for increasing numbers of input streams. Since shifting gradients brings the centreline closer to the conduit edge where flow velocities are lower due to conduit curvature, we adapt our model to account for these changing velocities. We first begin by predicting t using the mean velocity at the new shifted location, $u_{mean\ shift}$. Then, moving

down the conduit in steps Δx as before, we incrementally shift the mean velocity used to calculate t in steps Δz ($u_{mean\ shift-\Delta z}$), in the direction of the conduit centreline (i.e., $\Delta z = L/(s-a)$).

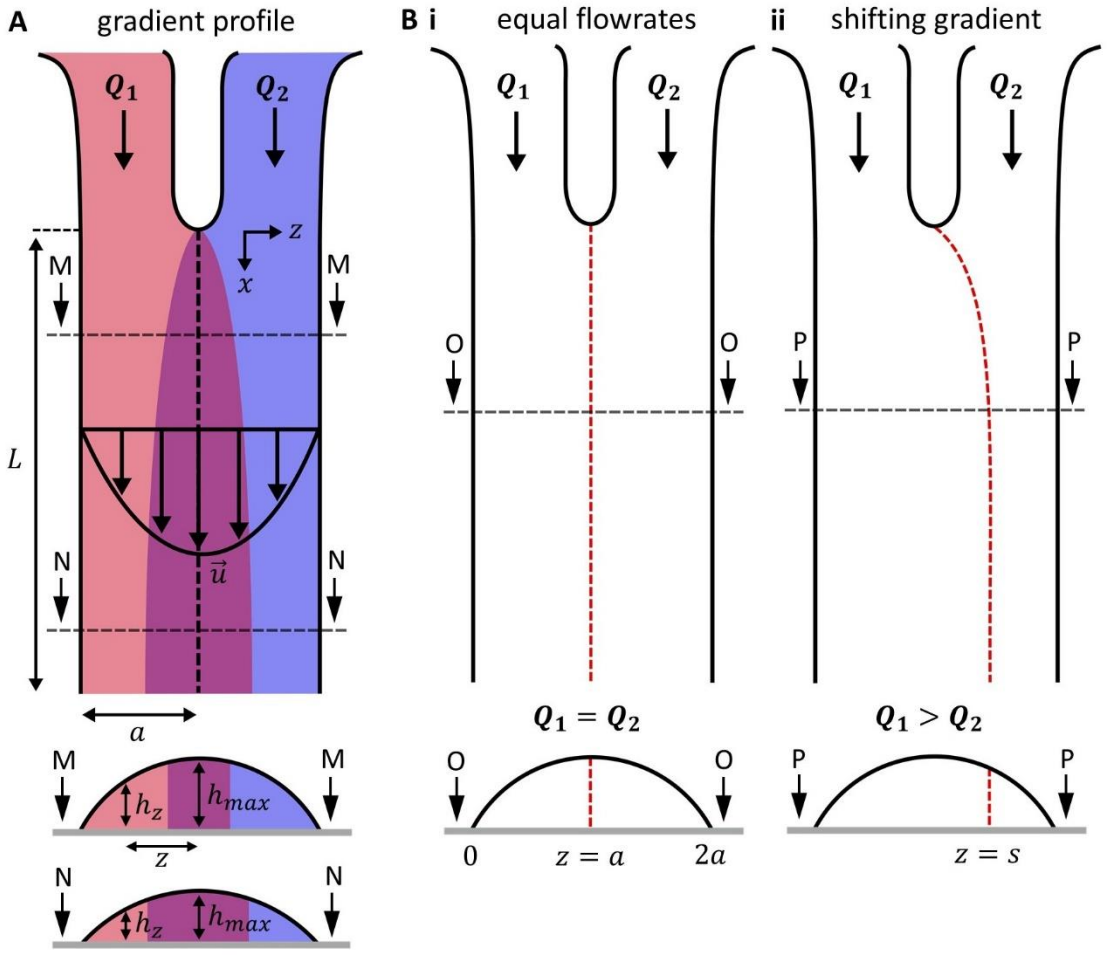


Fig. S4. Characterising stable and shifting gradients in active circuits. (A) General gradient and conduit characteristics. Illustration of a conduit with input streams Q_1 (red) and Q_2 (blue). Streams meet in the middle of the conduit below the junction, and diffusion creates a steady gradient across the width (purple area). Gradient width increases in the x-direction (as shown in cross-sections M-M and N-N). L = conduit length, a = conduit half width, $\vec{u}$ = velocity field, h_{max} = max conduit height, h_z = conduit height at z. **(B)** Location of gradient centreline for various input stream flow rate ratios. Plans are shown above, and cross-section profiles at O-O and P-P below. **(i)** For equal flow rates (i.e., $Q_1 = Q_2$), streams meet in the

middle of the conduit at location $z = a$ (denoted by the red dashed line). **(ii)** When the flow rate is increased in one arm relative to the other (i.e., $Q_1 > Q_2$), this centreline shifts in the direction of the weaker stream to location $z = s$.

To validate our assumptions for predicting gradients in the case where input flow rates are equal (**Fig. S4Bi**), we compare predictions using the average velocity along the conduit centreline (**Fig. S5i**) to predictions made using a numerical approach. This approach mirrors the case for the shifted gradient described for **Fig. 4Bii**, except that we first begin by predicting t using the mean velocity at the conduit centreline, and progressively shift the mean velocity used to calculate t to a distance $a/2$ from the centreline (**Fig. S5ii**).

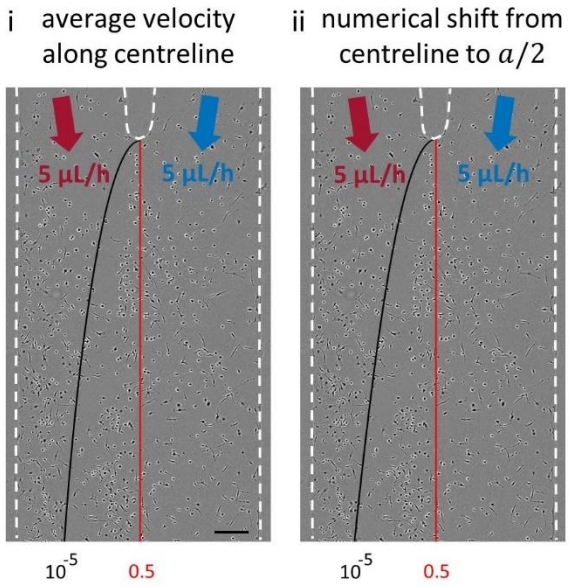


Fig. S5. Comparing gradient prediction methods in active circuits. Images of circuits shown at t = 24 h, with input flow rate $Q = 10$ µL/h. Scale bar = 250 µm. **(i)** Gradient predicted using the average velocity along the conduit centreline. **(ii)** Prediction using a numerical approach in which the average velocity is first taken along the centreline and then progressively shifted by a distance $a/2$.

Assessing the effect of circuit geometry on cell velocity

Fluid-walled conduits have circular cross-sections resulting in decreasing conduit heights from the centre to the wall (**Fig. S4**). Consequently, cells growing in such conduits have varying volumes of medium above them depending on their location in the conduit. We thus investigate the effect of cell position on cell behaviour using passive dumbbell-shaped circuits filled with cells, to assess whether these changing heights affect or bias cell behaviour. We expose cells in the circuits to either plain cell culture medium or uniform distributions of 10 nM C5a (no gradient) and image them over 48 h. We then segment circuits into 19 distinct regions, and compare cell velocities in each (**Fig. S6**). In this way, we show that average cell velocities throughout circuits are nearly identical and thus that changing heights do not impact cell behaviour.

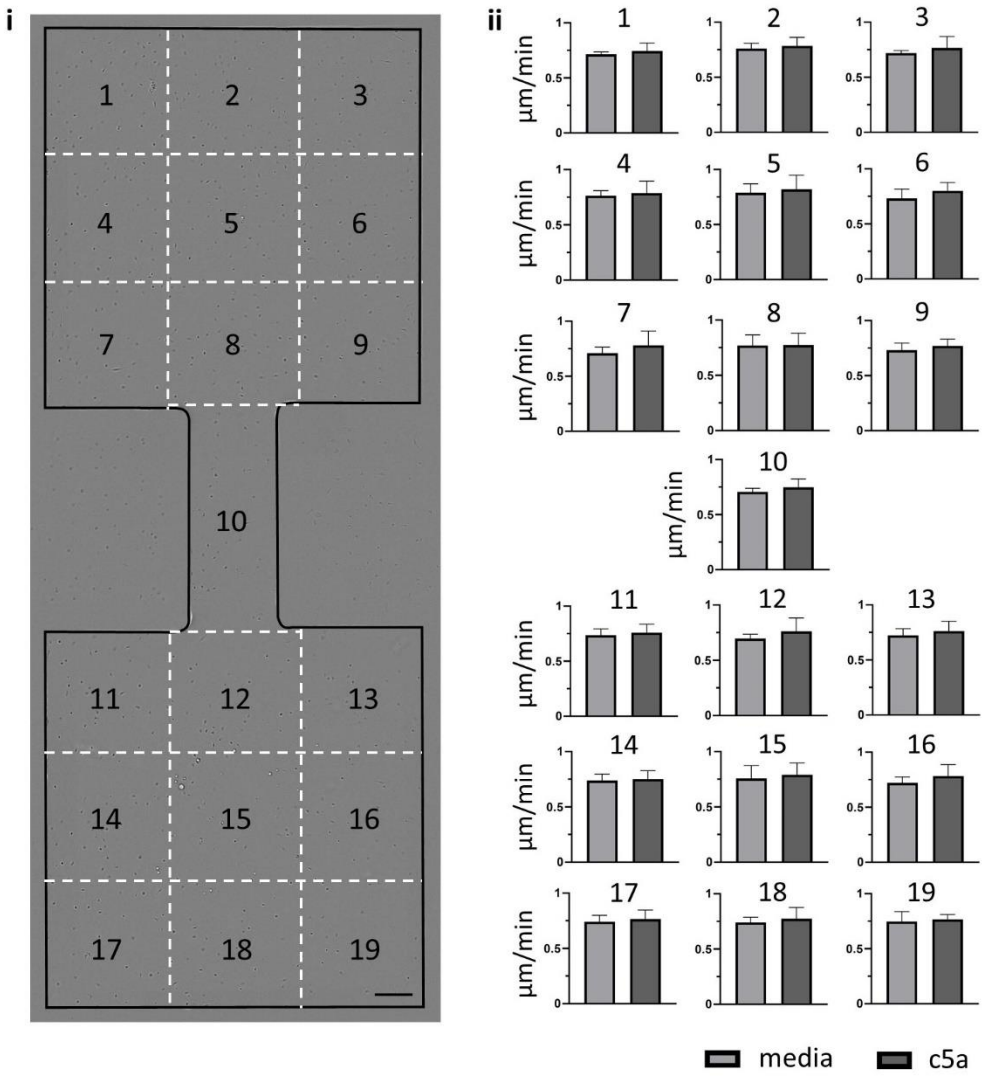


Fig. S6. Location within the circuit has no effect on velocity of BMDM movement. Control experiments in which cells are plated in the entire circuit are performed to identify potential biases in cell behaviour at various circuit locations. Average cell velocities are analysed in circuits containing only media or uniform distributions of 10 nM C5a (without gradient; 3 biological replicates for each condition). The circuits are imaged over 48 h and cell trajectories analysed. Circuits are segmented into 19 regions and cell velocities averaged for each location across all replicates. **(i)** Image of a full circuit containing cells, with superimposed plan showing the 19 regions. Scale bar: 250 µm. **(ii)** Cell velocities for both conditions and all regions. Average cell velocities are unaffected by circuit location or the presence of C5a.

Movies

Movie 1. Macrophages in the top chamber of a dumbbell circuit chemotaxing in a 10 nM gradient of C5a. Cells are initially contained within the top chamber (not visible), and few can be seen at the top of the conduit (1.5 mm). Cells chemotax through the conduit over 48 h towards the C5a chamber, which many are seen entering (bottom). Video link

Movie 2. Macrophages in the conduit of a dumbbell circuit chemotaxing in a 10 nM gradient of C5a. Cells are uniformly distributed in the conduit (1.5 mm). Most cells in the bottom half of the conduit chemotax over 48 h towards the C5a chamber, which many are seen entering (bottom). However, most cells in the top half do not chemotax and are chemokinetic. Video link

Movie 3. Macrophages in the conduit of a dumbbell circuit with media everywhere. Cells are uniformly distributed in the conduit (1.5 mm). In the absence of a C5a gradient (only media present), the cells are chemokinetic and move randomly over 48 h. Video link

Movie 4. Macrophages in the conduit of a dumbbell circuit with uniform distribution of 10 nM C5a. Cells are uniformly distributed in the conduit (1.5 mm). In the absence of a C5a gradient (uniform distribution of C5a), the cells are chemokinetic and move randomly over 48 h. Video link

Movie 5. Macrophages in 6 mm conduit chemotaxing in a 10 nM gradient of C5a. Cells are uniformly distributed in the conduit (6 mm). Only cells at the leading front chemotax over 48 h towards the C5a chamber. Cells located behind this band of responding cells do not chemotax and are chemokinetic. Video link

Movie 6. Macrophages in top third of a 6 mm conduit chemotaxing in a 10 nM gradient of C5a. Cells are distributed in the top third of the conduit (6 mm). Only very few cells (~7) at the leading front chemotax

over 48 h towards the C5a chamber. Cells located behind this band of responding cells do not chemotax and are chemokinetic. Video link

Movie 7. Macrophages in middle third of a 6 mm conduit chemotaxing in a 10 nM gradient of C5a. Cells are distributed in the middle third of the conduit (6 mm). Only cells at the leading front chemotax over 48 h towards the C5a chamber. Cells located behind this band of responding cells do not chemotax and are chemokinetic. Video link

Movie 8. Macrophages in bottom third of a 6 mm conduit chemotaxing in a 10 nM gradient of C5a. Cells are distributed in the bottom third of the conduit (6 mm). Only cells at the leading front chemotax over 48 h towards the C5a chamber. Cells located behind this band of responding cells do not chemotax and are chemokinetic. Video link

Movie 9. C5a-receptor KO macrophages in the top conduit of a 3-well dumbbell circuit in a 10 nM gradient of C5a. C5a-receptor KO cells are uniformly distributed in the top conduit (1.5 mm) of a 3-well dumbbell circuit. In the presence of a C5a gradient, cells are chemokinetic and move randomly over 48 h. Video link

Movie 10. WT macrophages in the bottom conduit of a 3-well dumbbell circuit in a 10 nM gradient of C5a. WT cells are uniformly distributed in the bottom conduit (1.5 mm) of a 3-well dumbbell circuit. In the presence of a C5a gradient, most cells in the top half of the conduit chemotax over 48 h towards the C5a chamber, which some are seen entering (top). However, most cells in the bottom half do not chemotax and are chemokinetic. Video link

Movie 11. Macrophages in 'm'-shaped circuit under a steady gradient of 10 nM C5a. Cells growing inside the conduit of an 'm'-shaped circuit are exposed to a steady gradient of C5a over 48 h. Media is perfused through the left arm (5 µL/h) and C5a through the right (5 µL/h). A gradient is established along the centre

of the conduit, and cells chemotax from into this region from the left, leaving behind a cell-deplete zone. Video link

Movie 12. Macrophages in 'm'-shaped circuit under a gradient of 10 nM C5a shifted abruptly to the right. Cells growing inside the conduit of an 'm'-shaped circuit are exposed to a steady gradient of C5a over 24 h. Media is perfused through the left arm (5 µL/h) and C5a through the right (5 µL/h). Cells on the left chemotax into the centre of the conduit to leave behind a cell-deplete zone. After 24 h, the gradient is shifted instantly 200 µm to the right by increasing media flow (7.15 µL/h) and decreasing C5a flow (2.85 µL/h), and kept steady for an additional 24 h in this new location. Cells in the centre of the conduit respond by chemotaxing further to the right. Video link

Movie 13. Macrophages in 'm'-shaped circuit under a gradient of 10 nM C5a shifting continuously to the right. Cells growing inside the conduit of an 'm'-shaped circuit are exposed to a steady gradient of C5a over 24 h. Media is perfused through the left arm (5 µL/h) and C5a through the right (5 µL/h). Cells on the left chemotax into the centre of the conduit to leave behind a cell-deplete zone. After 24 h, the gradient is shifted continuously over the next 24 h by 750 µm to the right, by gradually increasing media flow (from 5 to 9.98 µL/h) and decreasing C5a flow (from 5 to 0.02 µL/h). During this time, cells do not chemotax but appear chemokinetic. At the end of the continuous shift, the gradient is kept steady in the new location (150 µm from the right wall) for an additional 24 h. A new band of cells then responds by chemotaxing into this region, creating a cell-deplete zone in the right half of the conduit. Video link

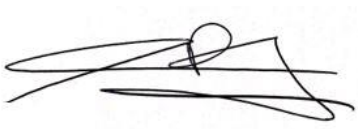
Statement of Authorship for joint/multi-authored papers for PGR thesis

To appear at the end of each thesis chapter submitted as an article/paper

The statement shall describe the candidate's and co-authors' independent research contributions in the thesis publications. For each publication there should exist a complete statement that is to be filled out and signed by the candidate and supervisor **(only required where there isn't already a statement of contribution within the paper itself).**

Title of Paper	Fluid-walled microfluidic assay for macrophage chemotaxis
Publication Status	Unpublished and unsubmitted work written in a manuscript style
Publication Details	C. Deroy, A. Rumianek, J. H. Wheeler, D. R. Greaves, P. R. Cook, and E. J. Walsh.

Student Confirmation

Student Name:	Cyril Deroy		
Contribution to the Paper	Lead author, designed and performed majority of experiments, led data collection and analysis, prepared all figures, coordinated and contributed to manuscript writing and editing.		
Signature		Date	27/09/2021

Supervisor Confirmation

By signing the Statement of Authorship, you are certifying that the candidate made a substantial contribution to the publication, and that the description described above is accurate.

Supervisor name and title: Prof. Edmond Walsh		
Supervisor comments		
Signature 	Date	27/09/21

This completed form should be included in the thesis, at the end of the relevant chapter.

Chapter 6: Discussion

Conclusion

This thesis presents for the first time a comprehensive study of fluid-walled microfluidic systems for cell migration assays and serves as a blueprint for the implementation of circuits that fit the specific requirements of biologists. The semi-analytical model introduced in **Chapter 3** is used to predict flow velocities and shear stresses in fluid-walled conduits of varying geometries when applying pump-controlled flows, and can be applied to more complex structures such as vascular trees. This model simplifies to a simple power law and is validated experimentally, making it accessible to less technical users and empowering them to design circuits suitable to their particular needs. Crucially, circuits are fabricated using the materials common to biologists, namely cell culture medium and Petri dishes, in a matter of seconds to minutes and directly on the benchtop. This approach thus makes microfluidic circuit design and fabrication accessible to the modern cell biologist.

Chapter 4 introduces a method to reconfigure microfluidic environments to isolate cells of interest in real-time on a microscope. Using simple 3D-printed adaptors, conventional inverted microscopes are converted into reconfiguring tools that manipulate fluid-walled circuits, all without interrupting flows. This method enables users to selectively isolate and extract phenotypically unique cells from diverse populations and analyse their genotype. Uniquely, circuit manipulations are performed with the precision of a microscope, typically in the micrometre range. This method thus provides users with familiar tools to interrogate and connect phenotype to genotype.

Finally, **Chapter 5** presents two distinct approaches to study chemotaxis in which cells are freely patterned on dishes and circuits printed around them. In the first, passive

dumbbell-shaped circuits are designed that can accommodate concentration gradients that remain stable for days. This approach does not require additional equipment like external pumps to establish and maintain concentration gradients, making it an attractive solution for chemotaxis studies. Additionally, these circuits are easily modified to incorporate multiple cell types for label-free comparison studies, and printed on well plates for higher-throughput assays. In the second approach, active circuits are implemented in which stable concentration gradients can be maintained continuously as flow continues driven by external pumps. In both methods, theoretical models allow concentration gradients to be defined and manipulated according to specific requirements. Algorithms are also developed to track cells in fluid-walled circuits and quantify chemotactic responses.

The outlined methods are then applied to investigate the behaviour of various cell types in response to concentration gradients and yield important results. Firstly, the semi-analytical model described in **Chapter 3** is used to control velocity fields and shear stress in fluid-walled conduits, informs the design of circuits with uniform shear stress distributions, and enables the quantification of concentration gradients in dynamic systems. This model thus guides the theoretical approaches used in the investigation of chemotaxis throughout this thesis. The method detailed in **Chapter 4** is then applied to study the behaviour of bacteria chemotaxing towards lethally-high antibiotic concentrations, and demonstrates that these cells exhibit suicidal behaviours as a counterattack mechanism to protect their colony. Lastly, passive and active circuits presented in **Chapter 5** are used to study population dynamics in primary murine macrophages, and demonstrate the likely cell-cell interactions involved in regulating and self-limiting chemotactic responses. Additionally, concentration gradients are controlled and moved to reveal possible spatiotemporal sensing of these cells.

Although this technology provides significant advantages and addresses many of the current limitations associated with traditional microfluidic systems, it does have disadvantages. First, the fluid-walls in these circuits have the particularity of morphing in response to changes in pressure, and thus do not have fixed geometries. As a result, these systems will fail (i.e., conduits will expand or break) when contact angles exceed 90 degrees, and so are limited in the flow rates they can accommodate, which will be far lower than the maximum flow rates used in solid-walled systems. This makes them less appropriate for applications in which high shear rates are required to influence cell behaviour. Second, conduits are limited in the range of widths they can achieve as smaller widths (e.g., < 100 μm) will result in very small heights (i.e., a few microns) making them prone to evaporation and thus impractical. As a result, conduits investigated throughout this thesis have widths > 500 μm. Third, although prototyping and fabrication times are greatly reduced and costs minimised, designing and implementing fluid-walled circuits requires technical expertise less suited for biologists, which this thesis searches to address by making the design and operation steps accessible to non-technical users. Finally, current workflows are not optimised for 3D cell culture models (e.g., spheroids and organoids), which are increasingly used in biomedical research.

In conclusion, this thesis presents the theoretical tools and experimental methods to implement fluid-walled microfluidics for various biological applications. By setting the framework for users to design and implement systems that fit their specific requirements, together with the multiple advantages offered by the technology, this thesis hopes to contribute in increasing the adoption of microfluidic systems in biomedical research and help address the unmet needs of biologists.

Future work

Dynamic systems controlled by gradients in Laplace pressure

The theoretical model developed throughout this thesis is used to define dynamic systems, which are relevant when mimicking biological environments as most cells experience flow *in vivo*. However, they require additional equipment such as syringe pumps to maintain steady flows throughout conduits. Alternatively, dynamic environments may be generated passively, using Laplace pressure to drive flow throughout the system. Such a system could consist of a large source drop connected to a thin conduit. At equilibrium, both source and conduit are nearly flat with Laplace pressures approximately zero. Adding cell culture medium to the source then increases its Laplace pressure and creates a pressure gradient across the system. Medium then flows through the conduit until the system reaches equilibrium again (**Fig. 1**). In this way, flow is controlled by differences in Laplace pressure across fluid-walled circuits and does not rely on external controllers. This makes it an attractive solution for continuous perfusion of cell cultures with the aim of increasing throughput of, for instance, spheroid and organoid formation. The challenge in this system would be to model the continuously-changing Laplace pressures and thus flow rates across conduits, to determine the maximum time cells could be perfused before re-initialising the system by adding more medium. Additionally, these systems are limited in their ability to maintain constant flow rates for long periods.

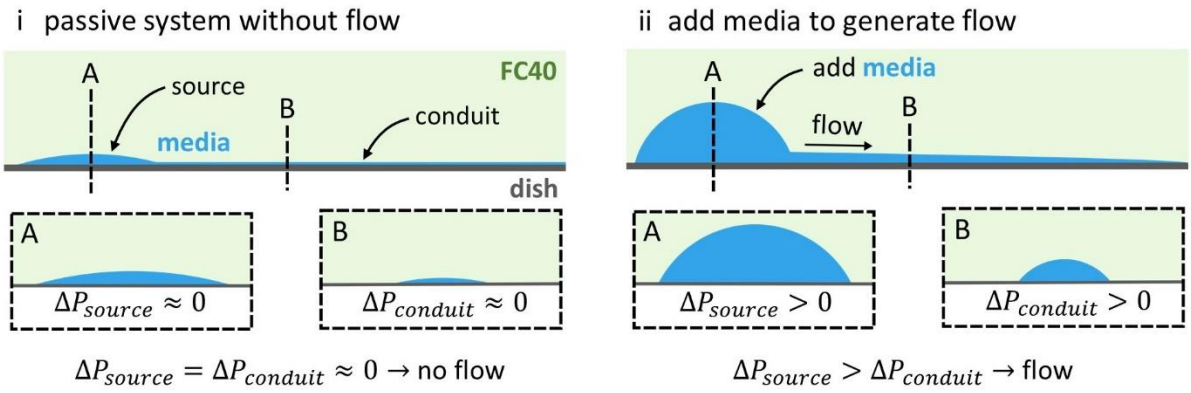


Fig. 1. Generating flow in passive circuits. Insets A and B show cross-sections of the source drop and conduit. **(i)** Passive circuit without flow. The system consists of a large source connected to a thin open-ended conduit. At equilibrium, Laplace pressure in both the source and the conduit are approximately zero resulting in nearly flat cross-sections. **(ii)** Adding media to the source drop increases its Laplace pressure and creates a pressure gradient across the system driving flow through the conduit.

Measuring diffusion coefficients in flowing conduits

The diffusion model presented in **Chapter 5** is used to predict diffusion gradients of C5a in active circuits and uses the theoretical diffusion coefficient of C5a determined from the Stokes-Einstein equation. However, these same circuits can now be used to measure the diffusion coefficient of fluorescent species by mapping fluorescence intensity to local concentration in the conduit. This could be used for instance to determine the actual diffusion coefficient of C5a using a fluorescent tag, and to assess the effect of conduit curvature on the diffusion gradient, especially when the gradient is shifted near the wall. To demonstrate this, measurements of the diffusion coefficient of fluorescein dextran (FD-10S, Sigma) of equivalent molecular weight to C5a used in **Chapter 5** ($MW_{fluo} = MW_{C5a} = 9$ kDa) are performed. To calibrate the system, conduits are first perfused with a solution of 300 µM fluorescein in PBS through both inlet arms (at the same flow rate) and a fluorescent image of the conduit is taken (**Fig. 2A**). Then, green pixel values across the entire conduit width are

extracted along a line drawn at three locations from the junction (1.5, 2, and 2.5 mm). These values are normalised (dividing by the maximum pixel intensity for each line) and plotted against the predicted normalised height profile of the conduit at that location to confirm the proportional relationship between pixel intensity and conduit height. One stream is then replaced with a solution of PBS to generate a concentration gradient of fluorescein across the conduit width (**Fig. 2B**). Pixel values are recorded along the same lines and converted to concentration by dividing with the calibration curve. This process is repeated for flow rates from 2.5 – 20 µL/h (solid lines in **Fig. 2C**). We then compare these results to theoretical predictions obtained with our model (dashed lines in **Fig. 2C**). By tuning the value of the diffusion coefficient of fluorescein to find the best fit, we find $D_{fluo} = 1 \times 10^{-10}$ m^2/s.

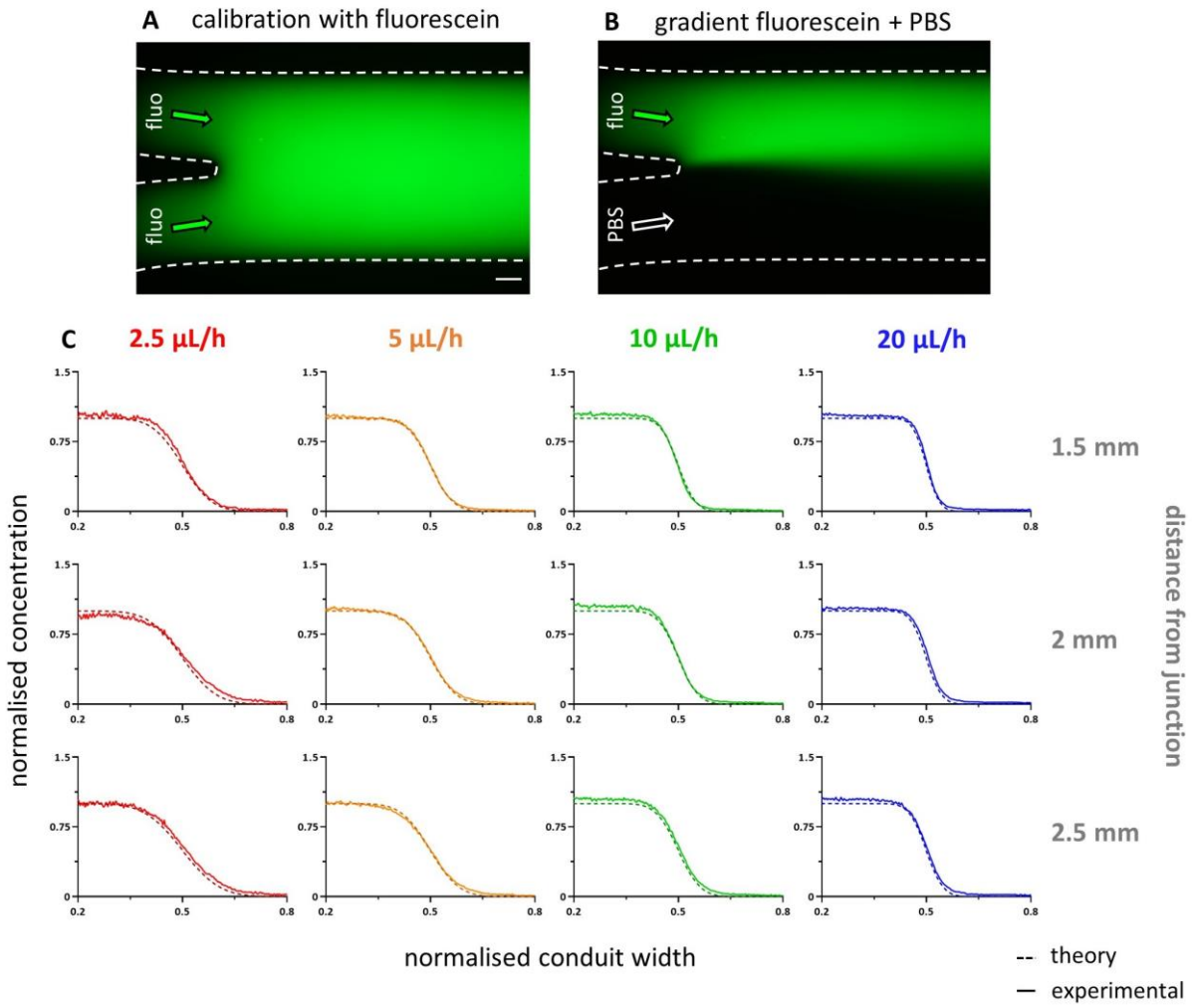


Fig. 2. Estimating the diffusion coefficient of fluorescein in active circuits. (A) Image of conduit perfused with two streams of 300 µM fluorescein in PBS at the same flow rate. Scale bar = 250 µm. **(B)** Image of the conduit with the bottom stream now replaced with pure PBS to create a gradient of fluorescein across the conduit width. **(C)** Plots of concentration gradients of fluorescein in active circuits for various flow rates. Line colours indicate the total flow rate in the conduit and measurements are taken at three distances from the junction (1.5, 2, and 2.5 mm). Solid lines represent experimental measurements, dashed lines show theoretical predictions.

Understanding the suicidal response of bacteria to antibiotics

In **Chapter 4**, bacteria are shown to migrate towards highly concentrated antibiotic and commit suicide. A possible explanation for this behaviour is that bacteria evolved to

counter-attack against competing bacterial strains by committing suicide to release toxins lethal to their competitors, thereby protecting their colony. As this chapter investigated the response of *P. Aeruginosa* to ciprofloxacin, it would now be interesting to investigate whether this behaviour is also found in other bacterial strains against different antibiotics. Furthermore, the underlying genotypic mechanisms involved in regulating the suicidal response have not been investigated, thus it would be interesting to perform RNA sequencing on the proportion of migrating cells extracted from circuits to determine the signalling pathways that control this response. These insights could then be harnessed to develop new approaches or therapies that trigger this suicidal response, potentially finding alternative treatments to antibiotics and reducing the risk of antibiotic resistance.

Population dynamics in macrophages

Chapter 5 explores the behaviour of murine macrophages to concentration gradients of C5a and reveals the likely cell-cell interactions that self-limit population response. Although this behaviour has recently been reported in neutrophils, the underlying mechanisms regulating these processes have not been identified in macrophages. It would therefore be interesting to further investigate this observed behaviour to understand and identify the self-regulating mechanisms at play and contrast them to those reported in neutrophils. Firstly, in passive circuits, the subpopulation of migrating cells could be isolated and extracted from the conduit using the same technique outlined in **Chapter 4** to reconfigure circuits. These cells could then be sequenced and compared to their non-responsive counterparts to assess genotypic differences in both populations and determine the signalling pathways involved. Additionally, the cell supernatant in the conduits could be extracted and analysed using mass

spectrometry to identify cell signalling molecules likely secreted by the subpopulation of chemotaxing cells (**Fig. 3**).

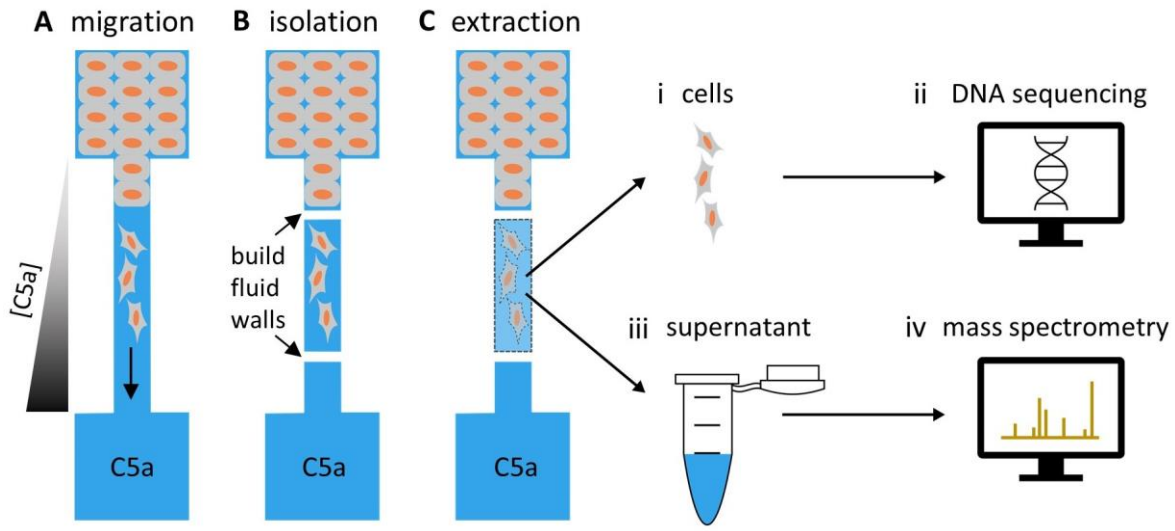


Fig. 3. Extracting subpopulations of chemotaxing macrophages and supernatant for downstream analysis. (A) Cells migrate in response to concentration gradients of C5a. **(B)** The migrating population of cells is isolated using the reconfiguration method outlined in **Chapter 4**, in which a PTFE stylus builds new fluid walls above and below this subpopulation to create an isolated chamber. **(C)** The contents of the chamber are then extracted, including **(i)** the cells for **(ii)** DNA sequencing, and **(iii)** the chamber supernatant for **(iv)** analysis by mass spectrometry.